Lund University GEM thesis series nr 07

Switching to the "Golden Age of Natural Gas" with a Focus on Shale Gas Exploitation: A Possible Bridge to Mitigate Climate Change?

Hossein Maazallahi

2015

Department of Physical Geography and Ecosystem Science

Lund University

Sölvegatan 12

S-223 62 Lund

LUND UNIVERSITY

UNIVERSITY OF TWENTE.

FACULTY OF GEO-INFORMATION SCIENCE AND EARTH OBSERVATION

Switching to the "Golden Age of Natural Gas" with a Focus on Shale Gas Exploitation: A Possible Bridge to Mitigate Climate Change?

by

Hossein Maazallahi

Thesis submitted to the department of Physical Geography and Ecosystem Science, Lund University, in partial fulfilment of the requirements for the degree of Master of Science in Geo-information Science and Earth Observation for Environmental Modelling and Management

Thesis assessment Board

First Supervisor: Prof. Petter Pilesjö (Lund University)
Co-supervisor: Dr. Robert Hack (ITC/University of Twente)

Exam committee:
Dr. Jonathan Seaquist
Dr. Sadegh Jamali

Disclaimer:
This document describes work undertaken as part of a program of study at the University of Lund. All views and opinions expressed therein remain the sole responsibility of the author, and do not necessarily represent those of the institute.

Course title:
Geo-information Science and Earth Observation for Environmental Modelling and Management (GEM)

Level:
Master of Science (MSc)

Course duration:
September 2013 until June 2015

Consortium partners:
The GEM master program is a cooperation of departments at 5 different universities:
University of Twente, ITC (The Netherlands)
University of Lund (Sweden)
University of Southampton (UK)
University of Warsaw (Poland)
University of Iceland (Iceland)

Maazallahi, H. (2015), Switching to the “Golden Age of Natural Gas” with a Focus on Shale Gas Exploitation: A Possible Bridge to Mitigate Climate Change?, Master degree thesis, 30 credits in Geo-Information and Earth Observation for Environmental Modelling and Management (GEM), Department of Physical Geography and Ecosystems Sciences, Lund University

Acknowledgement

It is essential to the author of this thesis to warmly appreciate support of warm-hearted people who have been shoulder by shoulder with the author. The author extends his unlimited gratitude to the family he has grown up in since twenty four years ago. It is great pleasure of the author to spread his thankfulness to friendly people who have taught him even a single word, especially to staffs during Petroleum Engineering program at BSc level at Chemical and Petroleum Engineering Department, Sharif University of Technology, Tehran, Iran, Geo-Information and Earth Observation for Environmental Modelling and Management (GEM) at MSc level at ITC/University of Twente, Enschede, The Netherlands, and Physical Geography and Ecosystem Science Department, Lund University, Lund, Sweden.

The author would like to deliver his highest sincere to the GEM program coordinator, Prof. Andrew Skidmore[1], the program directors specially to Prof. Michael Weir[1], Drs. Raymond Nijmeijer[1], and Prof. Petter Pilesjö[2], Ms. Laura Windig[1], the program secretary, and Mr. Ulrik Mårtensson[2], director of studies,.

The author expresses his utmost gratefulness to the supervisors of the research work, Dr. Robert Hack[1], and Prof. Petter Pilesjö[2], who have brighten the road of the thesis work to the author by opening enough meeting time in their schedule, and giving fruitfully clear comments.

The author has high respect to researchers and organizations who have established platforms for researchers, especially to developers of **Ed**ucational **G**lobal **C**limate **M**odelling (EdGCM), Columbia University/ **N**ational **A**eronautics and **S**pace **A**dministration (NASA) under direction of Dr. Mark A. Chandler, **En**vironment for **V**isualizing **I**mages (ENVI) software, Exelis Visual Information Solutions, **mat**rix **lab**oratory (MATLAB) software, MathWorks, Inc., and **hi**gh-resolution **tran**smission (HITRAN), Harvard-Smithsonian Centre for Astrophysics under direction of Prof. Laurence S. Rothman.

The author, hereby, expresses his extreme appreciations to research institutes, libraries, laboratories and organizations for providing accessible free data and reports, especially Jet Propulsion Laboratory (JPL), **G**oddard **I**nstitute for **S**pace **S**tudies (GISS), **A**tmospheric **C**orrection **P**arameter **C**alculator (ACPC), and **A**dvanced **S**paceborne **T**hermal **E**mission and **R**eflection **R**adiometer (ASTER) Library of NASA, **E**arth **S**ystem **R**esearch **L**ibrary (ESRL) of **N**ational **O**ceanic and **A**tmospheric **A**dministration (NOAA), U.S. **E**nergy **I**nformation **A**dministration (U.S. EIA), **I**ntergovernmental **P**anel on **C**limate **C**hange (IPCC), **E**uropean **E**nvironment **A**gency (EEA), **P**hoto**v**oltaic (PV) lighthouse, and World Bank.

The author is extremely thankful to Drs. Henk Kloosterman[1] who played as a friend in the very beginning steps of this work, Dr. Paul Miller[2] and Dr. Jörgen Olofsson[2] who played important roles in the climate simulation part of the thesis, Prof. Lars Eklundh[2] who opened his office generously to answer author's questions related to the remote sensing part of the study, and all fellows[1, 2] who put openhandedly time for improving message delivery of this research work.

The author is thankful to associations who highly take care of students, especially **E**uropean **A**ssociation of **G**eoscientists and **E**ngineers (EAGE), and **A**merican **A**ssociation of **P**etroleum **G**eologists (AAPG) who gave opportunities to the author for having direct meetings with active people from energy sector.

"Knowledge is in the end based on acknowledgement."

Ludwig Wittgenstein (1889-1951)

[1]ITC/University of Twente, Enschede, The Netherlands
[2]Physical Geography and Ecosystem Science Department, Lund University, Lund, Sweden

“Look deep into nature, and then you will understand everything better.”

Albert Einstein (1879-1955)

Abstract

Currently, policy makers put high attention in supplying global energy demand by focusing on 2°C policy; global temperature anomaly based on the global mean temperature of pre-industrial era (13.7°C). How to keep the 2°C policy at global scope is the main question in climate framework. It is widely believed that primary energy resources (mainly coal, oil and natural gas) with focus on shale gas resources (one of natural gas resources) will be the main resources to global energy demand. Based on the shale gas boom in USA, there is an open question related to amount of fugitive methane emission from shale gas exploitation at local scale. In this study, which is separated into two parts, it was intended to narrow down current questions on climate change at global scope, and shale gas exploitation at local scale. The first part of the study is about climate simulations based on different natural gas scenarios using **Ed**ucational **G**lobal **C**limate **M**odel (EdGCM) software. In the second part, **A**irborne **V**isible/**I**nfra**r**ed **I**maging **S**pectrum (AVIRIS) imagery over Marcellus shale basin in Pennsylvania, USA, was retrieved from **J**et **P**ropulsion **L**aboratory (JPL) of **N**ational **A**eronautics and **S**pace **A**dministration (NASA). By using **hi**gh-resolution **tran**smission (HITRAN) molecular absorption compilation and database the atmospheric transmittance spectrum was modelled. In order to map and evaluate fugitive methane emissions from shale gas well-heads, **Mat**rix**Lab**oratory (MATLAB) and **En**vironment for **V**isualizing **I**mages (ENVI) software were used. The results of the climate simulations show that if human activities switch from the current style of primary resources combustion (25.62% coal, 39.05% oil and 21.85% natural gas) to 8.5% coal, 19.24% oil, and 58.8% natural gas in average until 2100, there would be USD 19.82 billion (2005 USD) saved annually until 2078, for the countries who are paying for adaptation to climate change; meanwhile we can keep the 2°C policy until the end of 21st century. In the second part, in addition to inducing a new mapping technique of methane emission plumes, the results show that shale gas production has almost the same fugitive gas emissions as conventional gas wells, but some areas were detected where possible methane emissions were not direct fugitive emissions from the shale gas well-head but from surrounding areas of the well-pads. For these areas, site sampling and isotope analysis should be done to determine whether the probable methane emissions are results of shale gas activities. All in all, switching to supply global energy demand mostly from natural gas resources can play as a possible golden transition bridge to slow down global warming with consideration of local environmental impacts of shale gas exploitation.

Keywords: Age of natural gas; Fossil fuel combustion; Carbon Dioxide; Climate change; Fugitive Methane; Shale gas exploitation;

Popular Summary

We have the planet Earth where we and so many species are living. But so many alarms from Arctic all the way down to Antarctic are alerting us to very terrifying happenings at global scale which are known under climate change framework. The global warming is happening, which put living conditions on the blue planet Earth in dangerous red zones. According to a report from World Bank in 2010, annual adaptation costs to climate change at global scale is about USD 81.1 billion (2005 USD).

In the framework of climate change, it is extremely likely that burning fossil fuel resources are the main driving forces of global warming, so if we want to slow down the global mean temperature rise, we have to think about switching from the current style of fossil fuel combustion to a style which slow down the temperature rise, but how?

Our life styles have been dependant on fossil fuel combustions for a very long time, and it is impossible to change the style in the blink of an eye, so we need long term plans with support of short term plans. It is extremely likely that: I) our planet Earth is very vulnerable to temperature rise of more than 2°C, II) fossil fuel combustion is the main driving force of climate change, along with the facts that: I) we need resources to supply our energy demand, and II) natural gas combustion increase global mean temperature less than oil and coal combustion to produce the unit of energy. So, should we increase natural gas combustion share and decrease coal and oil share to keep the 2°C policy?

There are different resources from which we can extract natural gas. One of the natural gas resources is called shale gas formations. Fracking is a practice to extract natural gas from shale gas formations. Currently, we have heard about environmental impacts of fracking at local scale, mainly fugitive methane emissions, so here is the question: is it environmental friendly to increase the natural gas combustion from shale gas resources?

In this study, it was assumed that we are going to switch from current style of fossil fuel combustion to an age when we replace coal and oil with natural gas to slow down global warming, so let's call this age "Golden Age of Natural Gas". It was also assumed that the natural gas is extracted from shale gas resources. The results of this study show that if we switch from current style of fossil fuel combustions (25.62% coal, 39.05% oil and 21.85% natural gas) to 8.5% coal, 19.24% oil, and 58.8% natural gas in average until 2100, there would be USD 19.82 billion (2005 USD) saved annually. This switching should be implemented step by step in coherent plans at global scale as sudden change is far from reality. Fracking may be environmental friendly if companies from oil/gas sector follow standards. The "Golden Age of Natural Gas" may be considered as a bridge to mitigate climate change. This age will give us time to develop promising clean technologies to supply global energy demands.

Table of Contents

Abbreviation and Acronyms

USA	**U**nited **S**tates of **A**merica
U.S. EIA	**E**nergy **I**nformation **A**gency, USA
EPA	**E**nvironmental **P**rotection **A**gency, USA
IEA	**I**nternational **E**nergy **A**gency
IPCC	**I**ntergovernmental **P**anel on **C**limate **C**hange
UNFCCC	**U**nited **N**ations **F**ramework **C**onvention on **C**limate **C**hange
WMO	**W**orld **M**eteorological **O**rganization
UNEP	**U**nited **N**ations **E**nvironment **P**rogram
NOAA	**N**ational **O**ceanic and **A**tmospheric **A**dministration, USA
NASA	**N**ational **A**eronautics and **S**pace **A**dministration, USA
JPL	**J**et **P**ropulsion **L**aboratory, NASA, USA
ASTER	**A**dvanced **S**paceborne **T**hermal **E**mission and **R**eflection **R**adiometer, JPL, NASA, USA
EEA	**E**uropean **E**nvironment **A**gency
PA	**P**ennsylvani**a**, USA
CA	**Ca**lifornia, USA
LA	**L**os **A**ngeles, USA
AVIRIS	**A**irborne **V**isible/**I**nfra**r**ed **I**maging **S**pectrum
DN	**D**igital **N**umber
ROI	**R**egion **o**f **I**nterest
COP	**C**oal and **O**il **P**oint, CA, USA
ROI_CA	**R**egion **o**f **I**nterest in **Ca**lifornia as the Reference Point
ROI_PA_A	**R**egion **o**f **I**nterest in **P**ennsylvani**a** as one of Shale Gas Exploitation Areas
ROI_PA_B	**R**egion **o**f **I**nterest in **P**ennsylvani**a** as one of Shale Gas Exploitation Areas
HITRAN	**Hi**gh resolution **Tran**smission, compilation and database
EdGCM	**Ed**ucational **G**lobal **C**limate **M**odelling

ENVI	**En**vironment for **V**isualizing **I**mages
MATLAB	**mat**rix **lab**oratory
ANG	**A**ge of **N**atural **G**as
GHG	**G**reen**h**ouse **G**as
GWP	**G**lobal **W**arming **P**otential
RF	**R**adiative **F**orcing
ppb	**P**art **p**er **B**illion
ppm	**P**art **p**er **M**illion
NNC	**N**eural **N**etwork **C**lassification
H	**H**eight
T	**T**emperature
P	**P**ressure
RH	**R**elative **H**umidity
DOS	**D**ark **O**bject **S**ubtraction
ρ	Reflectance
ν	Frequency
λ	Wavelength
h	Planck's Constant
τ	Transmittance
L	Radiation
E_{irr}	Irradiance
E	Element Energy
C	Speed of Light
BB	**B**lack **B**ody

List of Figures

List of Tables

List of Diagrams

1 Introduction

In this chapter of the thesis, information on background of the thesis study, research objectives, research questions, scientific importance of the research work are written.

1.1 Background

In this part, facts which are provided in figures and literature studies related to the "**A**ge of **N**atural **G**as" (ANG) are given. Also, the relationship of ANG with climate change at global scope with focus on impacts of shale gas exploitation at local scale is described.

1.1.1 Age of Natural Gas and Climate Change at Global Scale

Increasing populations and subsequently increasing energy demands have resulted in huge demands for finding new unexploited fossil fuel resources. **I**nternational **E**nergy **A**gency (IEA) and U.S. **E**nergy **I**nformation **A**dministration (U.S. EIA) reported that although global energy demand will increase by 37% to 56% up until 2040 (equally supplied by four different sections: coal, oil, gas and low-carbon sources), there will be decrease in shares of coal and oil to supply global energy demand (IEA, 2014;U.S. EIA, 2013). It is also claimed that renewable energy sources are not sufficient for world's future energy demand and over-estimation of global potential of renewable energy will result in very dangerous policies (De Castro et al., 2013). It is also widely concluded that the global conventional oil peak has passed both from academic studies (Murray and King, 2012) and reports from international organizations (Sorrell et al., 2009). From the perspective of supplying future energy demand, with respect to decrease in oil and coal combustions and undetermined global potential of renewable energy, natural gas resources can get more attractions by policy makers.

The **I**ntergovernmental **P**anel on **C**limate **C**hange (IPCC) in 1988 was established by **W**orld **M**eteorological **O**rganization (WMO) and **U**nited **N**ations **E**nvironment **P**rogram (UNEP) (IPCC, 2015). IPCC is able to access to socio-economic documents on climate change issues, and on the alternative actions to decrease impacts of climate change, and the way to improve policies related to climate change. On request, IPCC feed reports and instructions to the Conference of Parties to the United Nations Framework Convention on Climate Change (UNFCCC). IPCC (1990) published reports on impacts of **g**reen**h**ouse **g**ases (GHGs) based on **r**adiative **f**orcing (RF) capacity of them. The detailed concept of RF is explained by IPCC (1990b). Generally, the RF is the amount of energy per unit area, per unit time, absorbed by GHGs that would otherwise be lost to space. As it can be understood from the Fig. 1, anthropogenic Carbon Dioxide (CO_2) has the highest contribution to increase global mean temperature.

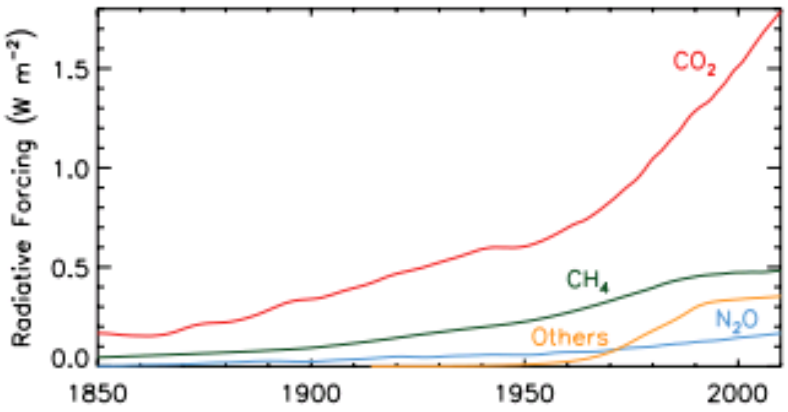

Figure 1- Anthropogenic GHGs contributions in increasing global radiative forcing, adopted from Myhre et al. (2013, P. 677)

In Fig. 2, based on real data from U.S. EIA (2015e), it is clear that the natural gas combustion has the least amount of CO_2 emission in order to produce the unit of energy compared to coal and oil combustion. So, in order to reduce anthropogenic CO_2 emission whilst supplying global energy demand, replacing shares of coal and oil with natural can be an option; however it is not clear how increasing share of natural gas for supplying global energy demand impacts on future climate.

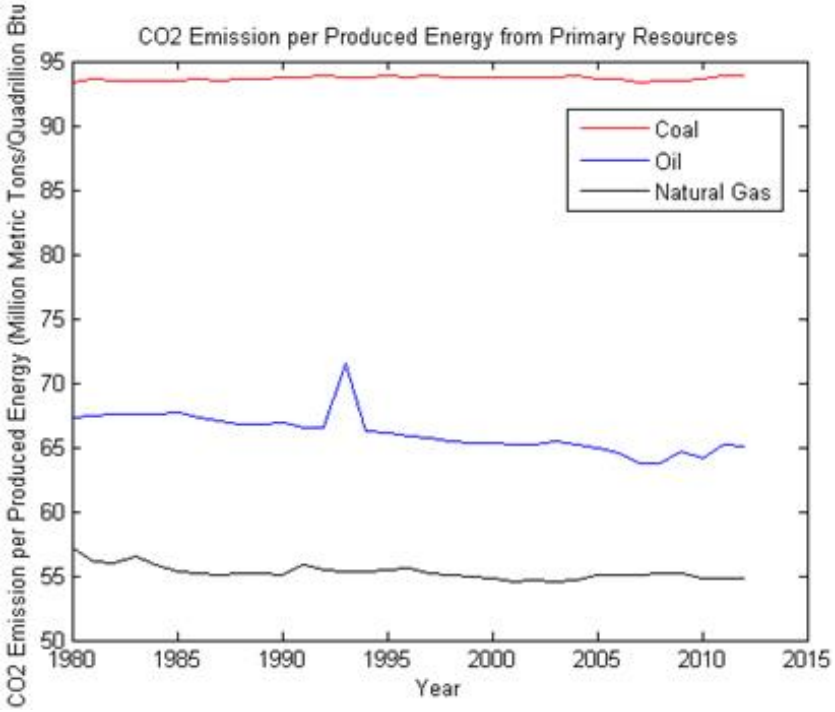

Figure 2- CO_2 emission from different primary sources per unit of energy (U.S. EIA, 2015e)

Supplying world's future energy demand with focus on keeping maximum 2°C rise in global temperature based on global mean temperature of pre-industrial era has been a concern for policy makers for making both short and long term plans (e.g. World Bank, 2010). It is reported that we have to take the 2°C policy seriously, else there will be dangerous consequences (Directorate-General for Climate Action, 2010). It seems there are still possible

mitigations to keep the 2°C policy by the end of 21st century (IPCC, 2014a, p. 20). Acting on the fifth IPCC assessment, it is "extremely likely" that over 50% of the global average surface temperature rise from 1951 to 2010 was the result of increasing anthropogenic concentration of GHGs (IPCC, 2014a, p. 5). The main anthropogenic GHGs are considered CO_2, Methane (CH_4) and Nitrous Oxide (N_2O) which have the main contributions to global warming (Qin et al., 2007); meanwhile 75% of anthropogenic CO_2 emissions into atmosphere are results of fossil fuel combustions, and cement productions (Forster et al., 2007, p. 131). Based on data from U.S. EIA, coal, oil and natural gas in average had supplied 86.52% (25.62% coal, 39.05% oil and 21.85% natural gas) of total global energy demand since 1980 to 2012 (Fig. 3). Keeping the same style of fossil fuel combustions will result in exceeding 2°C policy (Shaftel, 2015; Critchlow, 2015; IEA, 2015). It is essential to find a scenario by which anthropogenic emissions decrease enough, thus we can keep the 2°C policy.

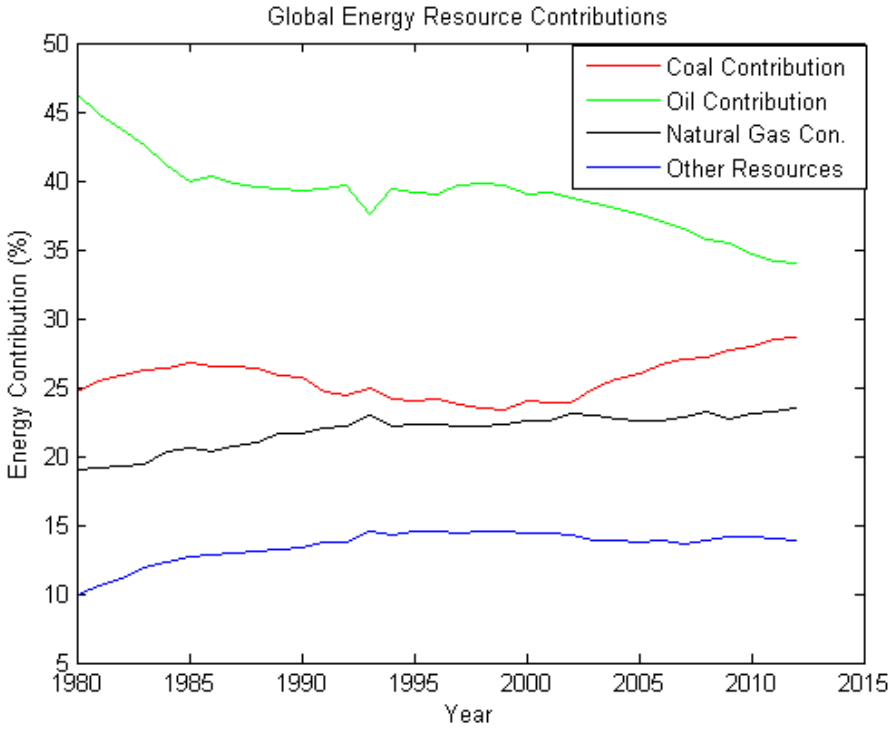

Figure 3- Contributions of resources to supply global energy demand (U.S. EIA, 2015f)

In 2000, IPCC defined different future anthropogenic emission scenarios, the scenarios are explained by Nakicenovic et al. (2000). In general, defining different scenarios shows available uncertainties on how the future will be. Acting on data from U.S. EIA, among available fossil fuel resources, natural gas is the cleanest one (Fig. 2), which produces the least CO_2 emissions comparing to coal and oil combustions to produce a unit of energy. It is also progressively mentioned that the future is the "golden age of gas" (IEA, 2012) with focus on shale gas resources (BP, 2014). On the other hand switching to high share of natural gas combustion is considered as a "bridge to nowhere", so we should not replace fossil fuel (coal, oil) with fossil fuel (natural gas) (Howarth, 2014). However, acting on the climate framework at global scale with focus on 2°C policy, it is uncertain that how golden the age of natural gas might be.

1.1.2 Impacts of Shale Gas Exploitation at Local Scale

Fossil fuels are separated into two main categories; conventional and unconventional resources (Halliburton, 2011). Conventional resources have been exploited for decades all around the world; those are considered conventional because, naturally, oil/gas can easily flow into wellbore. Unconventional resources are any reservoirs that require particular recovery operations within the unconventional formation, outside the conventional operating practices. Unconventional reservoirs include reservoirs such as tight-gas sands, gas and oil shale, coalbed methane, heavy oil and tar sands, and gas-hydrate deposits. Based on data from U.S. EIA (2015b), it is shown in Fig.4 that how the production of natural gas had been increased since 1990 until 2012 at global scale.

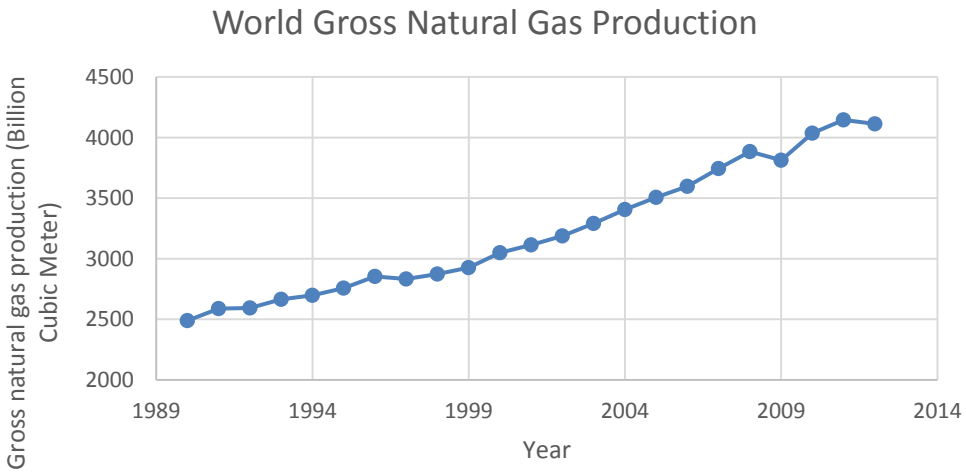

Figure 4- World natural gas production from 1991 to 2012 (U.S. EIA, 2015b)

Shale gas is considered as one of the main natural gas resources to supply global energy demand in future (BP, 2014). Currently the United States of America (USA) is the leading country in shale gas production. In Fig. 5, it is shown that how shale gas production from U.S. shale basins has been increased from 2007 to 2013.

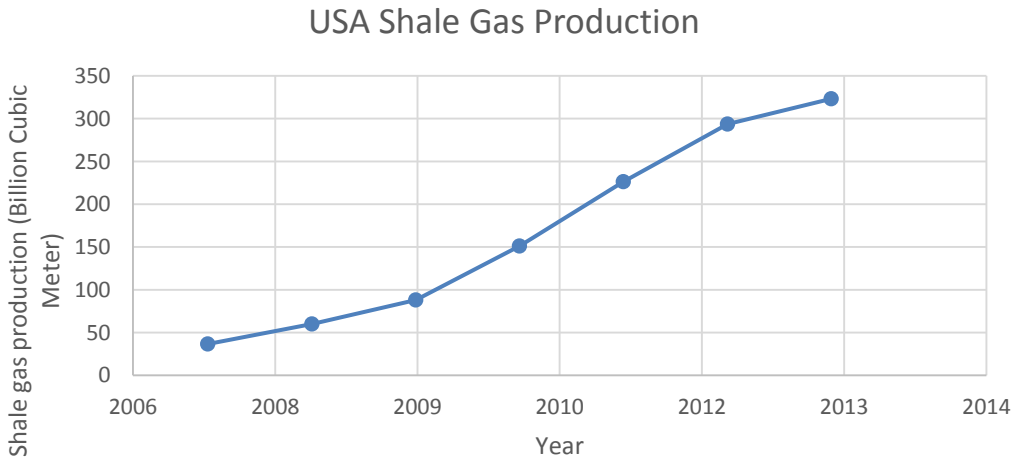

Figure 5- USA natural gas production from shale basins from 2007 until 2013 (U.S. EIA, 2015g)

Environmental Protection Agency (EPA) (2013b) announces that "natural gas and petroleum systems are the largest sources of CH_4 emissions from industry in the United States." There is fugitive methane emission from gas energy activities for both conventional and unconventional wells (Bradbury and Obeiter, 2013); from wellhead during production, work over, transportation, storage etc. It was also reported for the first time that fugitive methane emissions from shale gas exploitation are much higher than exploiting other fossil fuel resources (Howarth, Santoro and Ingraffea, 2011). Since 2011, there have been studies related to fugitive methane emissions from shale gas exploitation (Alvarez et al. 2012; Wilcox et al. 2014; Jackson et al. 2014). Howarth in 2014 mentioned that the results of the first article in 2011 were robust (Howarth, 2014). So, finding the effective technique to map and evaluate fugitive methane emission from shale gas activities makes this situation clear whether the fugitive methane emissions from shale gas exploitation are higher than normal. There are different techniques in remote sensing realm to detect methane emission plums (e.g. Roberts et al., 2010; Bradley et al., 2011; Thorpe, Frankenberg and Roberts, 2014). It was also reported that CH_4 emissions from drilling in Marcellus shale basin in Pennsylvania, USA are 1000 times EPA reports (Kelly, 2015). However there was not study with focus on shale gas exploitation sites in Marcellus shale basin in Pennsylvania, USA using remote sensing. So, remote sensing imagery over the shale gas exploitation sites in Marcellus shale basin, PA, USA might give an answer to the current question related to the amount of fugitive methane emissions over Marcellus shale basin. Answering to the question related to the fugitive methane emission can decrease uncertainties related to CH_4 emissions for policy makers for further consideration on the age of natural gas with focus on shale gas exploitation. Based on the data from U.S. EIA (2001), there are different shale basins across the USA, which are shown in the Fig. 6. In the thesis study, the focus was on Marcellus shale extent in PA, USA which is the largest basin for shale gas production in USA (Lieskovsky, Yan and Gorgen, 2014), in addition other required data (remote sensing imagery, wells data, etc.) were available for this basin.

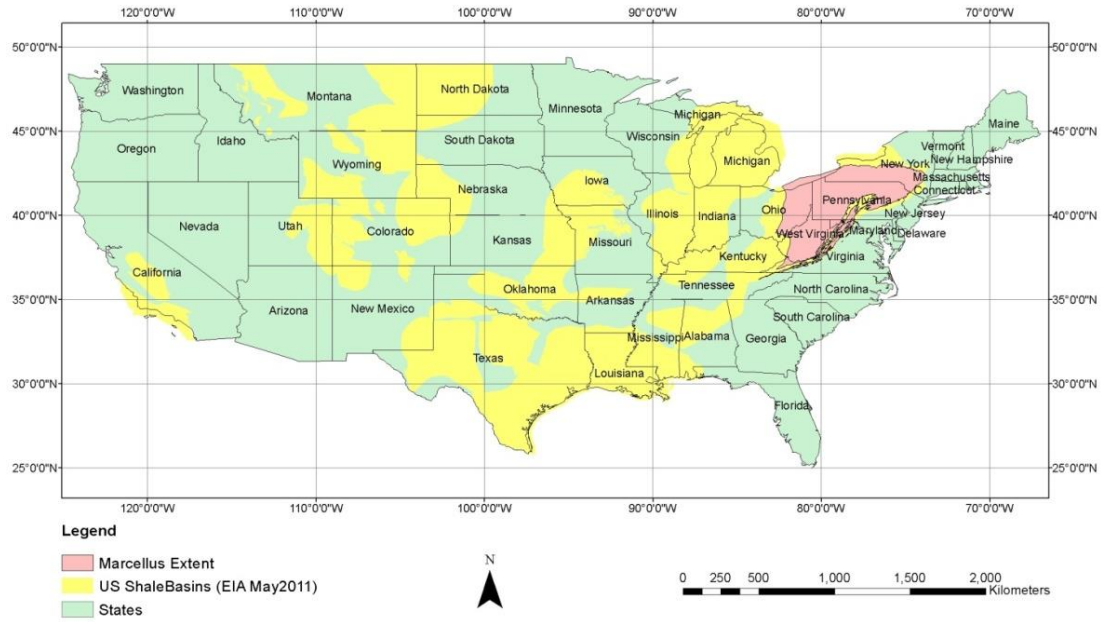

Figure 6- USA shale basins (U.S. EIA, 2015c) and boundaries of states (ArcGIS, 2012a)

In Fig. 5, the locations of gas wells over Marcellus shale basin in PA, USA are shown. Based on data from U.S. EIA, by Feb. 2015, 8891 wells were drilled. Among all the drilled wells, just 51 wells were drilled before 2007, which is the reason that recent shale gas activity in USA is called the boom period of natural gas production from shale formations.

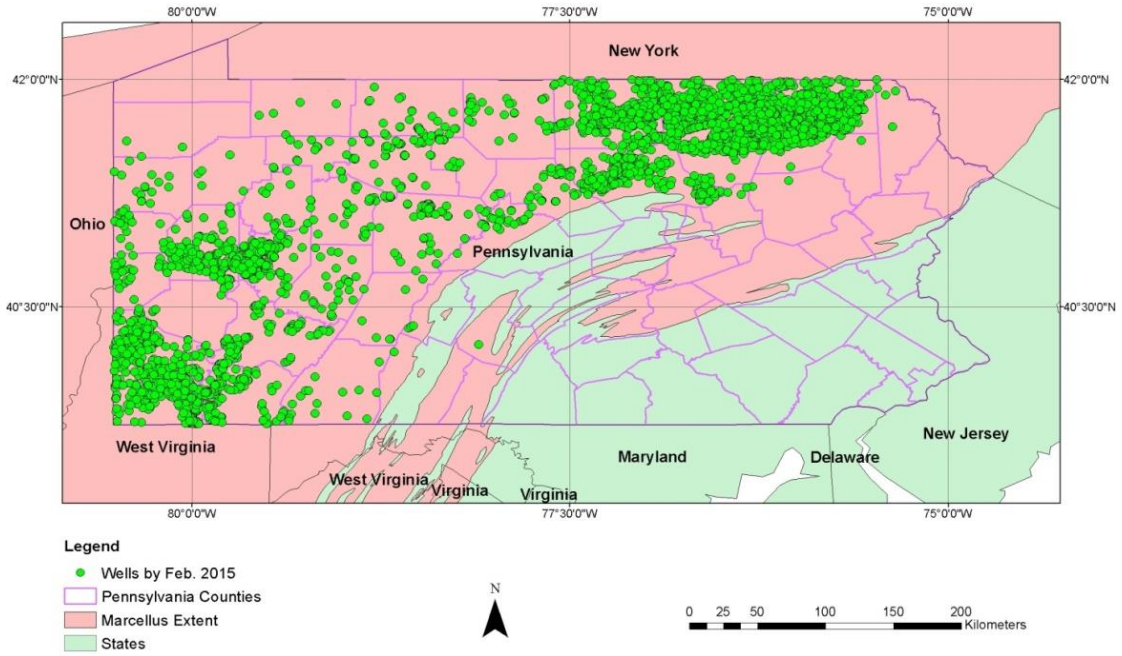

Figure 7- Well locations (U.S. EIA, 2015d) over Marcellus shale basin (U.S. EIA, 2015c) across counties of Pennsylvania (ArcGIS, 2012b), USA (ArcGIS, 2012a)

Natural gas reservoirs are classified into two main categories from the perspective of fluid types; dry and wet reservoirs (Fekete, 2014). The reservoirs which generally contain less than 85% of methane, more ethane, and other complex hydrocarbons are classified as wet gas. Dry

gas reservoirs are those with very high amount of methane with some intermediates. There was no information on type of wells in Marcellus shale basin in the wells' metadata. However, in northeast of Marcellus shale basin which was the study area of this thesis, dry gas is dominant (Marcellus center for outreach and research/Penn State University, 2009). So, in this thesis study, shale gas wells were considered as dry gas.

Throughout this thesis, it is assumed that in future, there will be much higher natural gas combustion for supplying global energy demand compared to current situation, so the term "**A**ge of **N**atural **G**as" (ANG) in any part of this study, refers to future with higher share of natural gas combustion among combustion of other world's total primary energy resources. It was also assumed that in future, energy sector will exploit unconventional gas resources; especially shale gas resources, for meeting the energy needs. Nowadays, about 21% of global energy demand is supplied by natural gas combustion (Fig. 3).

1.2 Problem Statement

In the last years, there have been large efforts to make international policies on slowing down global mean temperature rise (Ruamsuke, Dhakal and Marpaung, 2015). Majority of countries are now involved in climate change discussion to make long-term plans for supplying future world's energy demand from the view of socio-economic growth as it is reported by IPCC (2014a). Different perspectives on age of natural gas, whether this age helps to slow down global warming, occur. Based on a report from World Bank (2010, p. 96), uncertainties make decision making difficult to assess adaptation costs to global warming. The World Bank (2010, p. 19) estimated that by 2050, in order to keep the global mean temperature less than 2°C rise (based on global mean temperature in pre-industrial era), about USD 70 billion to USD 100 billion (2005 USD) needed to adopt to the climate change. The main question is: which scenario will lead us to keep the 2°C policy?

Based on the facts and documents provided in the background study of this thesis, it is probable, with high confidence, that in future primary energy resources (mainly coal, oil, and natural gas) remain the most in hand supply for global energy demand. It is also reported that natural gas production will increase; both from conventional and unconventional resources. However, in Fig. 8, it is shown that there are high uncertainties in both energy market and climate issues for policy makers. As it is shown in Fig. 8, issues related to energy market and climate framework have high impacts on lives of humans whilst these two issues have high uncertainties, so there is high need for acting to address uncertainties of these issues. In this thesis work, it is intended to address parts of these uncertainties and open questions by studying impacts of ANG scenarios on global mean temperature, and impacts of shale gas exploitation at local scale.

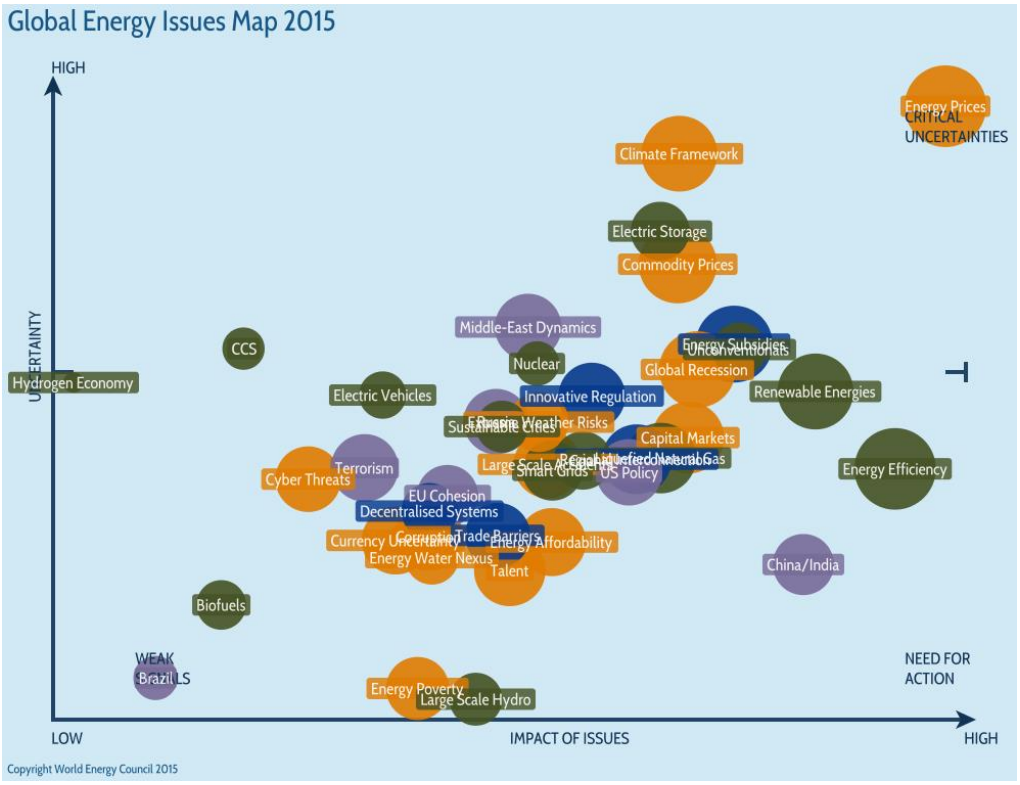

Figure 8- Map of global energy issues (World Energy Council, 2015)

1.3 Research Questions

- Can policy makers trust on increasing natural gas production as a golden bridge for supplying global future energy demand with consideration of global warming?
- Is it possible to map fugitive methane emission from well pads of shale gas production or surrounded area using remote sensing data; if any?
- Is it possible to calculate flux of fugitive methane emission from well pads of shale gas production or surrounded area using remote sensing data; if any?

1.4 Research Objectives

Generally, the objectives of this thesis are to evaluate the "age of natural gas" (ANG) with focus on shale gas exploitation. Specific objectives are to simulate global mean temperature under different ANG scenarios, meanwhile map and evaluate possible fugitive methane emission from shale gas exploitation sites in Pennsylvania, USA. In Diagram 1, the relationship between general and specific objectives of this study is shown.

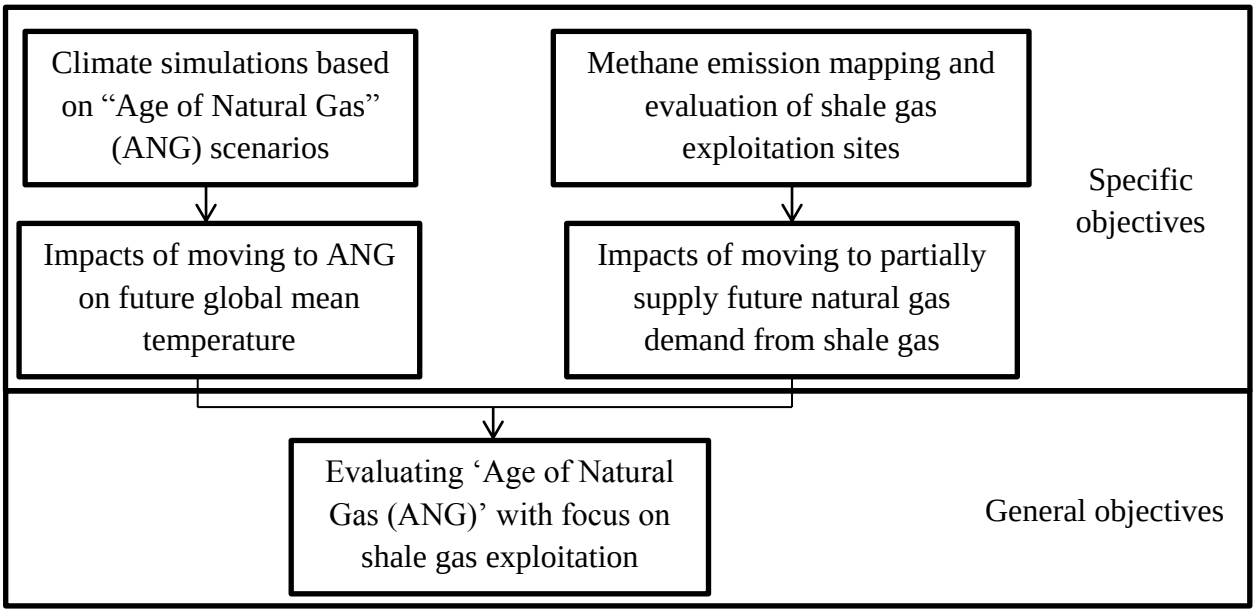

Diagram 1- General and specific objectives of this study

1.4.1 General Objective

The general aim of this thesis is to study the impacts of switching from current ~21% global natural gas production to ANG scenarios.

1.4.2 Specific Objectives

- To simulate future global mean temperature under different global natural gas production scenarios defined by the author and compare them with extending current portions of primary energy resources for future global energy demand as a control run
- To find a scenario by which we can keep the 2°C policy until the end of 21st century
- To detect fugitive methane emission points over shale gas well pads and surrounded area using remote sensing data
- To estimate flux of methane emission at probable detected points

1.5 Motivation of the Thesis Study

How climate change should be considered as an important issue to policy makers is explained by Darbee and Field (2010). Climate change increases annual costs at global scale (IPCC, 2007, p. 22). Adaptation costs of climate change at global scale is reported by World Bank (2010). Anthropogenic CO_2 and CH_4 are known as two major GHGs which are known as the main driving forces of current global warming (Myhre et al., 2013). About 75% of global anthropogenic CO_2 emissions into atmosphere are the results of fossil fuel combustions, and cement productions (Forster et al., 2007, p. 131). Since 2007, there has been shale gas (one of unconventional natural gas resources) exploitation boom in the USA, and it is predicted that at global scale natural gas extraction from unconventional resources will speed up in future (BP 2014). It is mentioned by IPCC (2014a, p. 13) that CO_2 has the main contribution in global warming. Environmental Protection Agency (EPA) (2013b) announces that "natural gas and petroleum systems are the largest sources of CH_4 emissions from industry in the United States." Howarth et al. (2011) claimed that fugitive methane emission from shale gas exploitation is much higher compared to exploiting conventional gas reservoirs. Increasing natural gas production in future is called "golden age of natural gas" (IEA, 2012) or "a bridge to nowhere" (Howarth, 2014). So, more research on the age of natural gas should be studied

both at global scale with focus on anthropogenic CO_2 emissions, and at local scale (shale gas extraction sites in the USA) with focus on fugitive CH_4 emissions.

1.6 Contribution to Future of the Planet Earth and Academia

The results of this thesis are important for energy sector policy makers who also consider climate change in long term plans at international scale. Detecting natural or anthropogenic gas plumes over any regions of interest gives a clue about natural or human activities across the regions, so the results may be useful to understand the happenings at regions of interest. The results of this study could be used for energy or climate policy makers. A new straight forward technique for methane plum detection is introduced using remote sensing imagery. This technique might be extended for detecting other kinds of gas plumes.

1.7 Research Outline

This outline shows how this document is separated into different parts. The first chapter provides the background of the study along with the current problems for which specific and general objectives were defined (Diagram 1). The materials and methods are written in the second chapter, and in the third chapter results are presented and discussed. In the fourth chapter, conclusions of this study, and future works are described. At the end of this document, references and appendices are provided.

I. Introduction
   a. Background
   b. Problem Statement
   c. Research Objectives
   d. Research Questions
   e. Motivation of the Thesis Study
   f. Contribution to Future of the Planet Earth and Academia
II. Material and Methods
   a. Data Extrapolation Methods
   b. Climate Simulations
   c. Methane Emission Mapping and Evaluation
III. Results and Discussion
   a. Climate Simulations
   b. Methane Emission Mapping and Evaluation
IV. Conclusions and Future Works
   a. Conclusions
   b. Future Works
V. References
VI. Appendices
   a. Appendix A (Climate Simulations)
   b. Appendix B (Methane Emission Mapping and Evaluation)
   c. Appendix C (Access Links to Datasets)
   d. Appendix D (MATLAB Codes)

2 Materials and Methods

In order to achieve the research objectives of this study, future climate simulations and fugitive methane emission mapping and evaluation were computationally operated. In this chapter, sources of data, data preparation methods, software, equations along with explanatory diagrams of how the steps were taken are described.

This study is separated into two main sub-studies. The first part is about climate simulations to find out impacts of switching to "**A**ge of **N**atural **G**as" (ANG) on global mean temperature under different ANG scenarios. The second part is about fugitive methane emission mapping, and an evaluation to figure out the probable flux of fugitive methane emission from shale gas exploitation sites in Marcellus shale basin, PA, USA. All in all, first part deals with simulations, and the second part is modelling.

2.1 Data Extrapolation Methods

In this study, in order to find extrapolated variation trends of different dataset spatially or temporally in both simulations and modelling parts, fitting models over available historical data played an important role. Firstly, a fitting model with the highest fitting goodness value was calculated using MATLAB (The MathWorks Inc., 2012) over a variation trend. Secondly, the variation trend was extrapolated (spatially or temporally) based on the fitting model.

2.1.1 Fitting Models

Linear (Eq. 1), exponential (Eq. 2) and Gaussian (Eq. 3) fitting models were the most suitable fitting models in this study based on the identity of different datasets. The selection of the fitting model was based on the fitting goodness which is also known as R-Square.

$$\boldsymbol{f(x) = a * x + b} \qquad \textbf{Equation 1}$$

where a is slope, b is intercept of linear model, x is explanatory variable and f (x) is dependent of x.

$$\mathbf{f(x) = a_1 * e^{b_1 * x} + a_2 * e^{b_2 * x}} \qquad \textbf{Equation 2}$$

where a_1, b_1, a_2, and b_2 are the coefficients of the exponential model, x is the explanatory variable and f (x) is function of x.

$$\mathbf{f(x) = a_1 * e^{(\frac{-(x-b_1)}{c_1})^2} + a_2 * e^{(\frac{-(x-b_2)}{c_2})^2}} \qquad \textbf{Equation 3}$$

where a_1, b_1, c_1, a_2, b_2, and c_2 are the coefficients of the Gaussian model, x is the explanatory variable and f (x) is function of x.

2.1.1.1 Fitting Goodness (R-Square)

Fitting goodness or R-Square shows how well a model fits over a dataset. R-Square is in the range from 0 to 1 and calculated by Eq. 4. The higher value of R-Square shows better fitting over the data. So, one of the introduced fitting models (Eq. 1, Eq. 2, and Eq. 3) which gives the highest R-Square was used.

$$\mathbf{R-Square} = 1 - \frac{\sum_{i=1}^{n} w_i(y_i - f(x))^2}{\sum_{i=1}^{n} w_i(y_i - y_{avg})^2} \qquad \textbf{Equation 4}$$

where, y_i is observed value, f(x) is predicted value by the fitting model, y_{avg} is average value of observed data, and w_i is weight which is 1 in all fitting models in this study.

2.2 Climate Simulations

Educational **G**lobal **C**limate **M**odelling (EdGCM) (Columbia University and NASA, 2013) is a powerful software by which future climate can be simulated and visualized in user friendly interface by EVA (Columbia Univeristy and NASA, 2012) for students at university level and educational institutions (Chandler, 2015). The use of the software is mentioned in other research works in climate simulation framework (e.g. Evangelinos et al., 2006; Crouch, Shen, Austin and Dinniman, 2008; Lanckriet et al., 2012; Huning and Margulis, 2015) . EdGCM and EVA were developed by Columbia University and **N**ational **A**eronautics and **S**pace **A**dministration (NASA) scientists in a joint project at the **G**oddard **I**nstitute for **S**pace **S**tudies (GISS) (Chandler, Richards and Shopsin, 2005). EdGCM was developed based on database structure so students and researchers can study future or past climate by changing driving forces, e.g. changing concentrations of atmospheric GHGs or altering solar luminosity. More information about how the software is functioning is available on the EdGCM website (http://edgcm.columbia.edu/). In the climate simulations of this thesis work, it was focused on the impacts of changing atmospheric concentrations of GHGs on future global mean temperature. The required data files for simulating future climate were downloaded from databases of NASA, IPCC, **E**uropean **E**nvironment **A**gency (EEA), and U.S. EIA. Diagram 2 demonstrates general steps of the climate simulations part. Firstly, in order to start simulations, it was required to estimate future atmospheric concentrations of GHGs under each ANG scenario. Secondly, the simulation of future global mean temperature under each ANG scenario was done by the EdGCM. Thirdly, based on the simulations outputs, a scenario was proposed by which we can keep 2°C policy until 2100. Finally, based the report of World Bank (2010) on adaptation costs to climate change, financial saved by the introduced scenario was estimated.

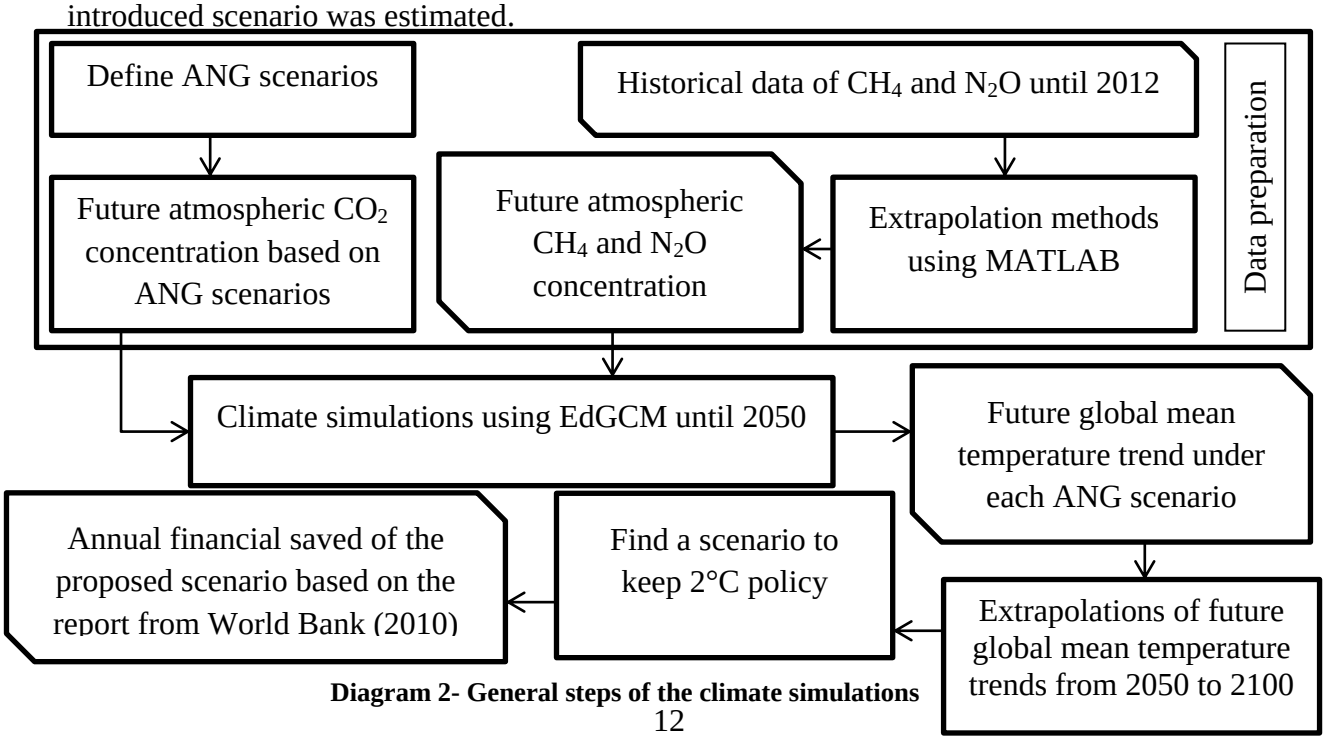

Diagram 2- General steps of the climate simulations

2.2.1 Global mean Temperature Estimation in Pre-Industrial Era

Pre-industrial era is defined the time before the beginning of industrial revolution in 1750 (IPCC, 2007b, p. 2). It is estimated that the global mean temperature in the pre-industrial era was equal to the global mean temperature from 1850 until 1900 (Buckle and Mactavish, 2013). Based on global mean temperature anomalies from 1850 until 1900 in the IPCC report (2014a, p. 3), and the global mean temperature values from GISS/NASA (2015), it was estimated that the global mean temperature in pre-industrial era was 13.7°C.

2.2.2 Extent of Climate Simulations

When it comes to study climate change, it is undeniable to study the globe as a system. Regional and local human activities result in global changes, so in the study of climate change it is important to analyse impacts of human activities such as changes in concentration of GHGs at global scope (NOAA, 2007). In the climate simulations of this thesis, the driving forces of climate change are increases of atmospheric concentrations of three main GHGs; CO_2, CH_4 and N_2O. Future annual atmospheric concentrations of CH_4 and N_2O under the ANG scenarios were estimated based on the extrapolations over historical data. Future annual atmospheric concentration of CO_2 under each ANG scenario was estimated based on CO_2 emissions from coal, oil, and natural gas combustions. The simulations under all scenarios were done until 2050, as the outlook reports of future energy are around 2050 (e.g. BP 2014; U.S. EIA 2014; World Energy Council 2014). Global climate simulations were time consuming which is another reason of simulating until 2050. Finally, based on the simulations until 2050, the variation trend of global mean temperature under each ANG scenario was extrapolated until 2100.

2.2.3 Age of Natural Gas (ANG) Scenarios

Six different ANG scenarios, based on different shares of primary resources to supply future global energy demand with focus on an increasing share of natural gas combustion. Throughout this thesis, these six scenarios are called ANG scenarios. Acting on Fig. 3, in average current human life style is 86.52% dependent on primary resources (mainly coal, oil, and natural gas) combustion. In the control run scenario, it was assumed that until 2050, human activities will remain dependent on the same contribution of each primary resources as it had been in average from 1990 until 2012; 25% for coal, 39.05% for oil, and 21.85% for natural gas (Fig. 3). In the other five ANG scenarios as it is shown in Table 1, the contributions of either coal or oil or both were decreased by 5% or 10%. The total contribution of coal, oil, and natural gas to supply global energy demand was considered 86.52% in all scenarios. So, the same percentage of decrease in contributions was considered as increase in contribution of natural gas combustion to supply global energy demand.

Table 1- Contribution of coal, oil and natural gas to supply global energy demand in the ANG scenarios

Resources	Contributions of resources in each scenario (%)					
	Control Run	Scenario 1	Scenario 2	Scenario 3	Scenario 4	Scenario 5
Coal	25.62	15.62	10.62	10.62	5.62	0
Oil	39.05	29.05	29.05	19.05	19.05	0
Natural Gas	21.85	41.85	46.85	56.85	61.85	86.52

2.2.4 Climate Simulations Diagram

The climate simulations were done by the use of EdGCM software. The data for the ANG scenarios were transferred from different databases; NASA, EEA, IPCC and U.S. EIA. In practice, the measurement methods of atmospheric concentrations of GHGs from different agencies are different, so in order to verify the data, actual atmospheric GHGs (Fig. 28 in Appendix A) from EEA and the IPCC data distribution centre were retrieved and mean values of the data from these two dataset were used. As it is demonstrated in Diagram 3, which is about the detailed steps of climate simulations of this study, finding extrapolation trends for CH_4 and N_2O were straight forward but not for CO_2.

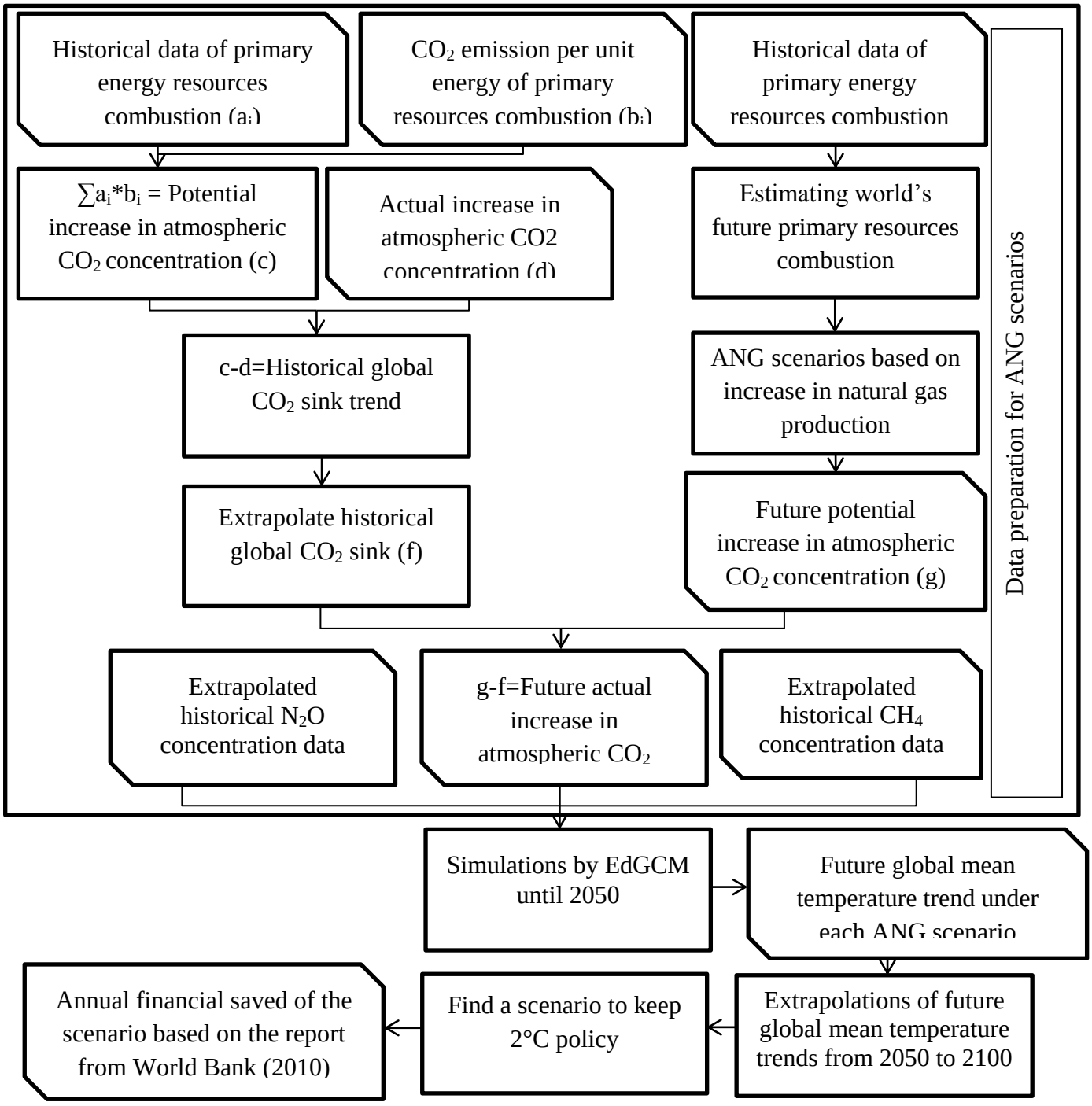

Diagram 3- Detailed steps of data preparation for climate simulation

2.2.5 Data Retrieval and preparation for Climate Simulations

Atmospheric concentrations of CO_2, CH_4 and N_2O as input driving forces for climate simulations for the ANG scenarios were done by fitting models over historical data and extrapolations of the fitting models. The extrapolations for CH_4 (Fig. 29b in Appendix A) and N_2O (Fig. 29c in Appendix A) were based on fitting models over real data, but to find atmospheric CO_2 concentration more steps were taken.

2.2.5.1 Atmospheric CO_2 Concentrations for ANG scenarios

To estimate future atmospheric concentration of CO_2, first it was required to know how much primary resources will be combusted under different ANG scenarios. In order to estimate future energy consumptions from coal, oil, and natural gas resources, real data from U.S. EIA (2015f) were retrieved. Linear and exponentially fitting models were modelled using historical data. Mean values of the two fitting models were used as the future global consumptions of primary resources. In Fig. 9, real data from 1980 till 2012 along with the extrapolation models are shown.

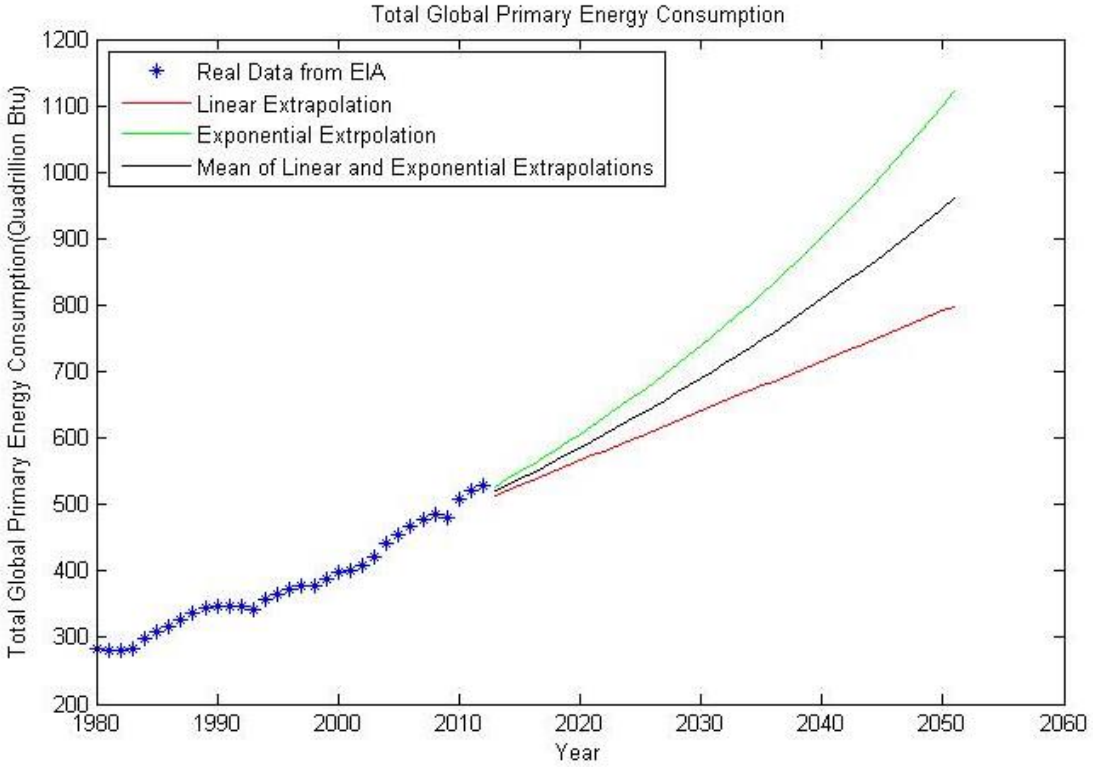

Figure 9- Historical data of coal, oil, and natural gas combustion (U.S. EIA, 2015f) along with extrapolations of the historical data

The fitting properties over historical data of global coal, oil, and natural gas combustions are shown in Table 2. The first column shows the models used, the second column shows equation of each models. The third and fourth columns show the coefficients of the fitting models. Finally, the mean value of linear and exponential models were calculated which is shown in the fourth row of Table 2. The fifth column of Table 2 shows R-Square for linear and exponential fitting models.

Table 2- Fitting properties of models over global coal, oil, and natural gas combustions (Quadrillion Btu)

Fitting model	Equation	a		b		R-square
Linear	a*year + b	7.498		-1.458e+004		0.9646
Exponential	a * exp(b*year)	2.199e-015		0.01988		0.9821
Mean	$\frac{a_1 * year + b_1 + a_2 * exp(b_2 * year)}{2}$	a_1	a_2	b_1	b_2	-
		7.498	2.199e-015	-1.458e+004	0.01988	-

As it is shown in Fig. 10, CO_2 emissions from fossil fuel combustions account for about 74% of global total emission of CO_2 (IPCC (2007) in U.S. EPA (2013a)). However, there are different natural CO_2 sinks by which 55% of anthropogenic CO_2 emissions sink every year (Ciais et al., 2013, p. 467).

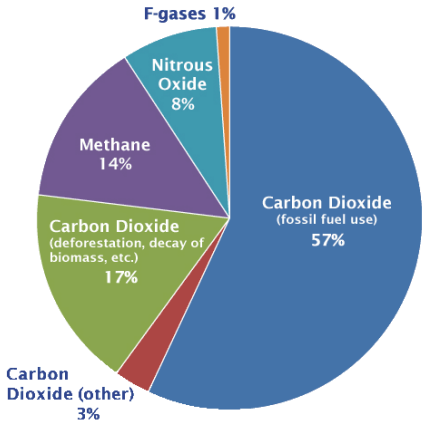

Figure 10- Global GHG emissions by gas from IPCC (2007) in U.S. EPA (2013a)

Based on historical contributions data of coal, oil and natural gas in supplying global energy demand (Fig. 3), and CO_2 emission from combustion of each primary resource (Fig. 2) potential increase of CO_2 concentration in the atmosphere was estimated (blue stars in Fig. 11). Based on potential along with actual atmospheric CO_2 increase (Fig. 11), the global sink of CO_2 was estimated from 1980 to 2012, and extrapolated linearly till 2050 (Fig. 12). The linear fitting model was used because of high fluctuation of data. Assumption of linear increase of global natural CO_2 sink is also mentioned by Raupach et al. (2014, p. 3454). It is reported that anthropogenic CO_2 emissions sink about 50% (NOAA, 2012) to 55% (Ciais et al., 2013) by natural processes at global scale every year. In average, the estimation on global CO_2 sink in Fig. 12 was estimated 51.22% from 1980 to 2012 in annual basis.

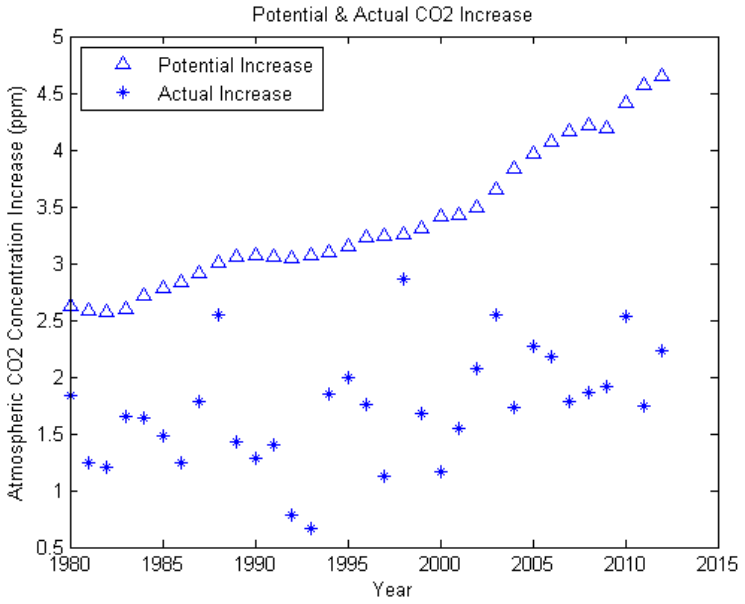

Figure 11- Estimated potential atmospheric CO_2 increase (Diagram.3), and mean value of actual atmospheric CO_2 increase from two datasets: EEA (2013) and IPCC (2014b)

Subtracting the actual CO_2 increase from potential CO_2 increase (Fig.11) gives the global CO_2 sink (Fig.12).

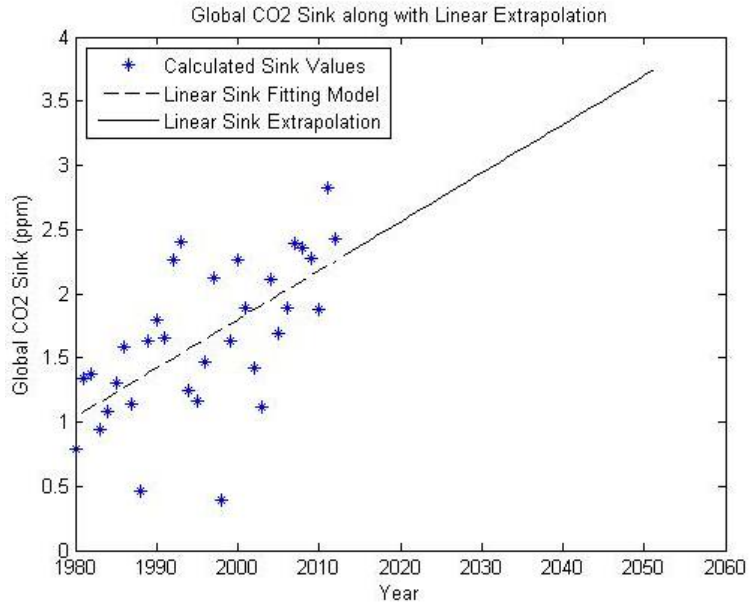

Figure 12- Global CO_2 sink from 1980 till 2012 along with linear extrapolation until 2050

In Table 3 the fitting properties over historical CO_2 sink are presented.

Table 3- Fitting properties over global CO_2 sink (ppm)

Fitting model	Equation	a	b	R-square
Linear	a*year + b	0.03796	-74.12	0.3828

Based on future global energy demand from coal, oil and natural gas (Fig. 9), contributions of coal, oil, and natural gas in each ANG scenarios (Table 1), CO_2 emission per unit of energy from combustion of each primary resource (Fig. 2), and global CO_2 sink (Fig. 12), the future atmospheric concentrations of CO_2 were estimated for each ANG scenario as one of the driving forces input to the EdGCM for climate simulations (Fig. 29 in Appendix A).

2.2.5.2 Atmospheric N_2O and CH_4 Concentration for ANG scenarios

Estimation of the future atmospheric concentrations of N_2O and CH_4 were based on extrapolation on fitting models over mean real data from EEA and IPCC (Fig. 28 in Appendix A). The driving forces input for climate simulations by EdGCM from N_2O and CH_4 along with CO_2 trends are presented in Fig. 28 and Fig. 29 in Appendix A.

2.3 Fugitive Methane Emission Mapping and Evaluation

The second part of this study deals with the mapping and evaluating fugitive methane emissions over shale gas drilling sites in the Marcellus shale basin, Pennsylvania, USA. Firstly, it was necessary to map the pixels of methane emissions. In order to verify mapping and evaluating techniques, there was a need for a known methane emissions point. In this study, natural seep of methane in coal and oil point (COP) in California, USA, was selected as it is one of the largest natural methane seep (Leifer, Kamerling, Luyendyk and Wilson, 2010, p. 331). In addition, there were studies of the COP (e.g. Roberts et al., 2010; Bradley et al., 2011; Thorpe, Frankenberg and Roberts, 2014), and the flux of methane emission from COP was reported by Quigtey et al. (1999, p. 1050). In this part, ArcMap (ESRI, 2013) was used for visualizing geographically coordinated extent of the study areas, ENVI (EXELIS, 2013) for remote sensing analysis, and MATLAB for programming.

2.3.1 Airborne Visible/Infrared Imaging Spectrum (AVIRIS)

In order to map and estimate flux of gas plumes, remote sensing is a powerful tool, and high spectral spectrometer allows mapping pixels of a gas plume using a specific spectral fingerprint for each gas (American Geophysical Union, 2012). In this study, imagery from **A**irborne **V**isible/**I**nfra**r**ed **I**maging **S**pectrum (AVIRIS) flights was used. AVIRIS is a unique spectral sensor in remote sensing which gives upwelling radiance in 224 bands from 250 to 2500 nm. The flights are generally in height of 20 km above sea level with 34 degree field of view at a speed of 730 km per hour (JPL, 2015). Information about the AVIRIS imagery including bands' wavelength and gain values for converting digital number (DN) values into radiation are presented in Table 24 (Appendix B). In order to visualize true colour of AVIRIS imagery band 29 as red, band 20 as green, and band 12 as blue were used.

In Diagram 4, the relationships between the reference point, mapping techniques and flux evaluation of fugitive methane emissions are shown. In Diagram 2, it is also shown how the regions of interest (ROIs) were selected.

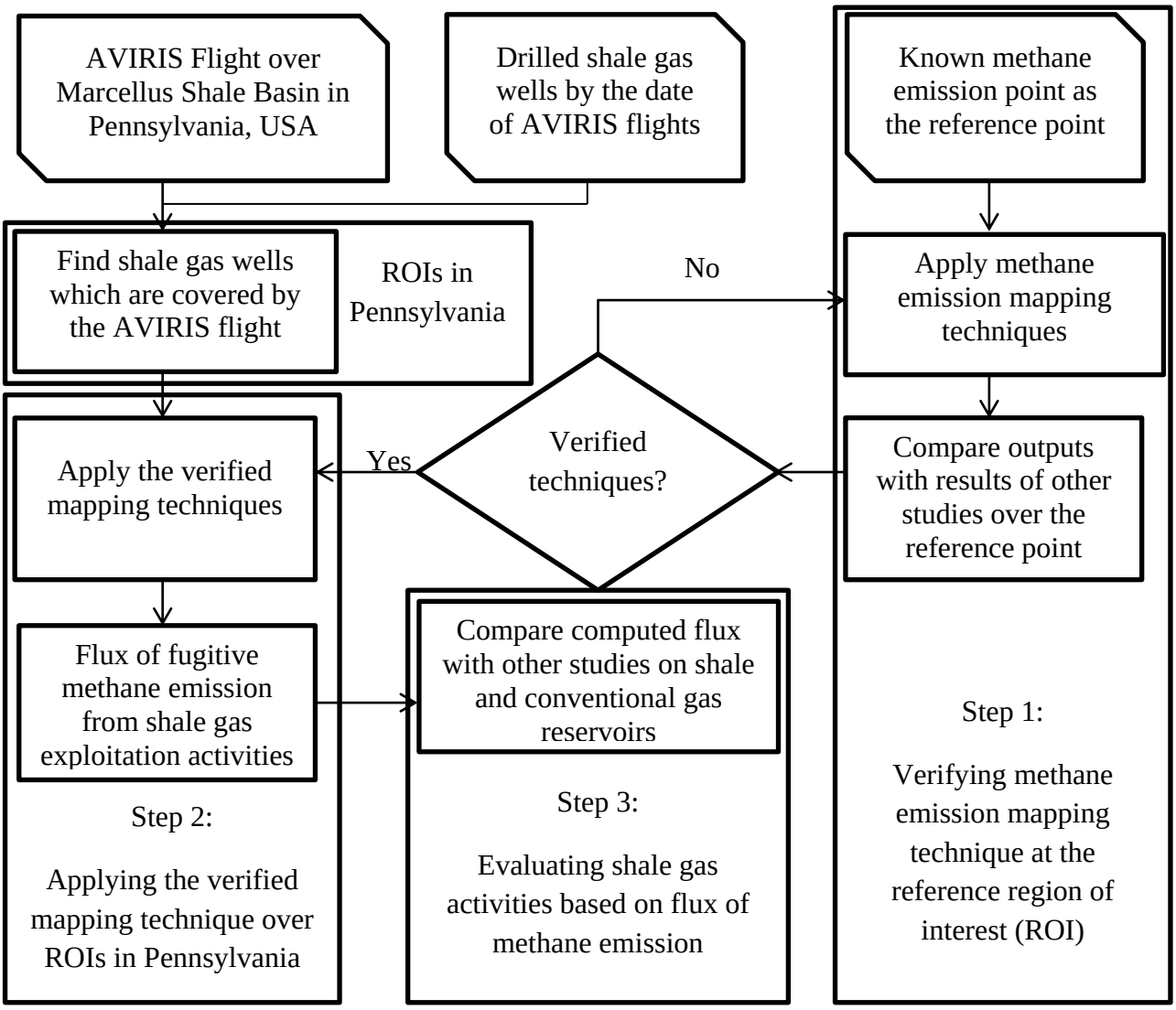

Diagram 4- General steps of verifying the methane emission mapping and evaluation methods

Mapping methane emissions using AVIRIS imagery has been reported by other researchers using spectral residual (Roberts et al. 2010), band ratio (Bradley et al. 2011), and cluster-tuned matched filter (Thorpe et al. 2014) techniques.

2.3.2 Extent of Methane Emissions Study Area

This study was focused on shale gas exploitation over the Marcellus shale basin in Pennsylvania, USA. It consists of desk work, and no field work was done, so there was a need to have a reference point where flux of methane emission is already known. Based on other studies (Bradley et al., 2011; Thorpe, Frankenberg and Roberts, 2014) over the COP in California, USA, using AVIRIS imagery, the COP which is one of the largest global natural methane seep (Leifer, Kamerling, Luyendyk and Wilson, 2010, p. 331) was chosen as the reference point. Finally, based on the at-sensor radiation model over the COP (the reference point) in CA, USA, flux of fugitive methane emission from shale gas exploitation in the Marcellus shale basing in PA, USA, was estimated.

2.3.2.1 AVIRIS Flight, CA, USA (AVIRIS_CA)

On 19-June 2008, there was an AVIRIS flight over the COP, CA, USA. Throughout this thesis this flight is called "**AVIRIS_Ca**lifornia" (AVIRIS_CA) (Fig. 13). The same **r**egion **o**f

interest (ROI) as Bradley et al. (2011), and Thorpe, Frankenberg and Roberts (2014) studied using AVIRIS imagery was considered. The ROI is pointed out in Fig. 13, and called "**R**egion **o**f **I**nterest _**Ca**lifornia" (ROI_CA) throughout this thesis, and it is completely sea water.

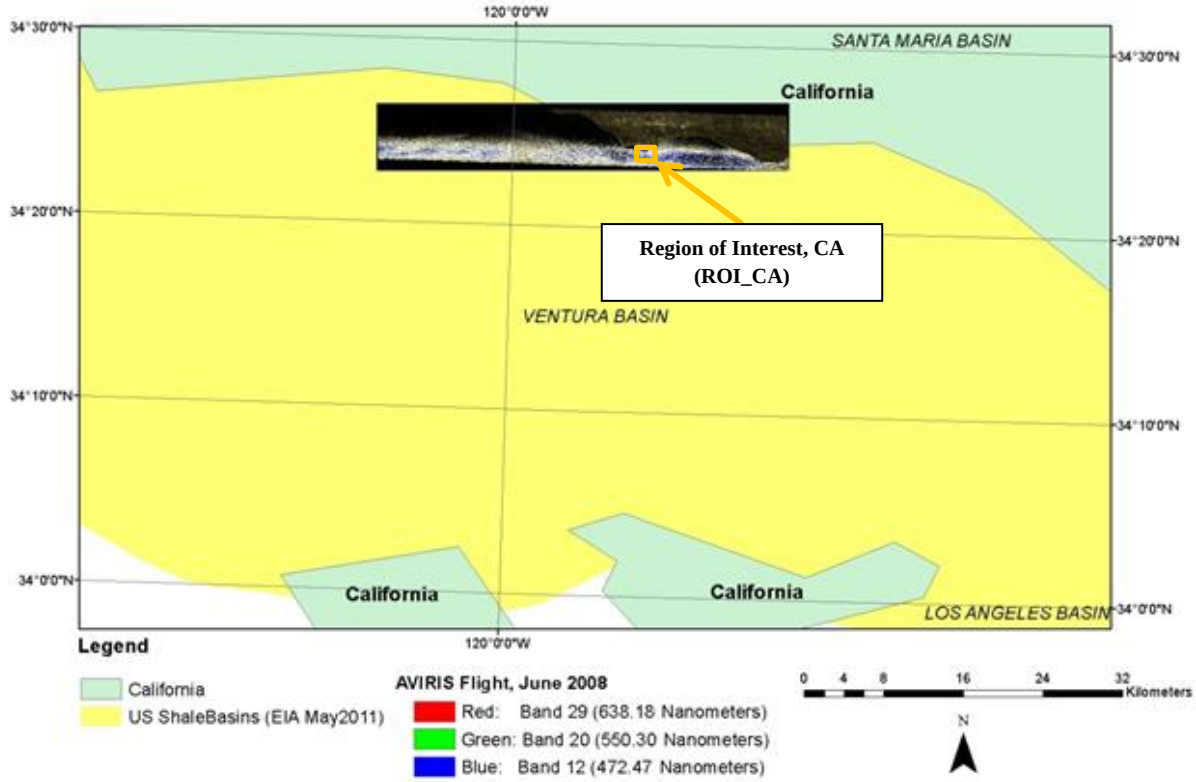

Figure 13- AVIRIS flight (JPL/NASA, 2015) in true colour over coal and oil basin (U.S. EIA, 2015c), CA, USA (ArcGIS, 2012a)

The flight information is written in Table 4, and was retrieved from metadata of the flight provided by JPL/NASA.

Table 4- AVIRIS_CA flight information

Date	Time (Local)		Latitude		Longitude		Altitude (km)
19 June 2008	Start	End	Start	End	Start	End	10
	12:50:00	20:00:00	34.383333	34.383333	-120.083	-119.7333	

2.3.2.1.1 Reference Point, CA, USA (ROI_CA)

In this study the reference point, which is called ROI_CA, is shown in Fig. 14. As it is shown in Fig. 14, the ROI_CA is fully sea water.

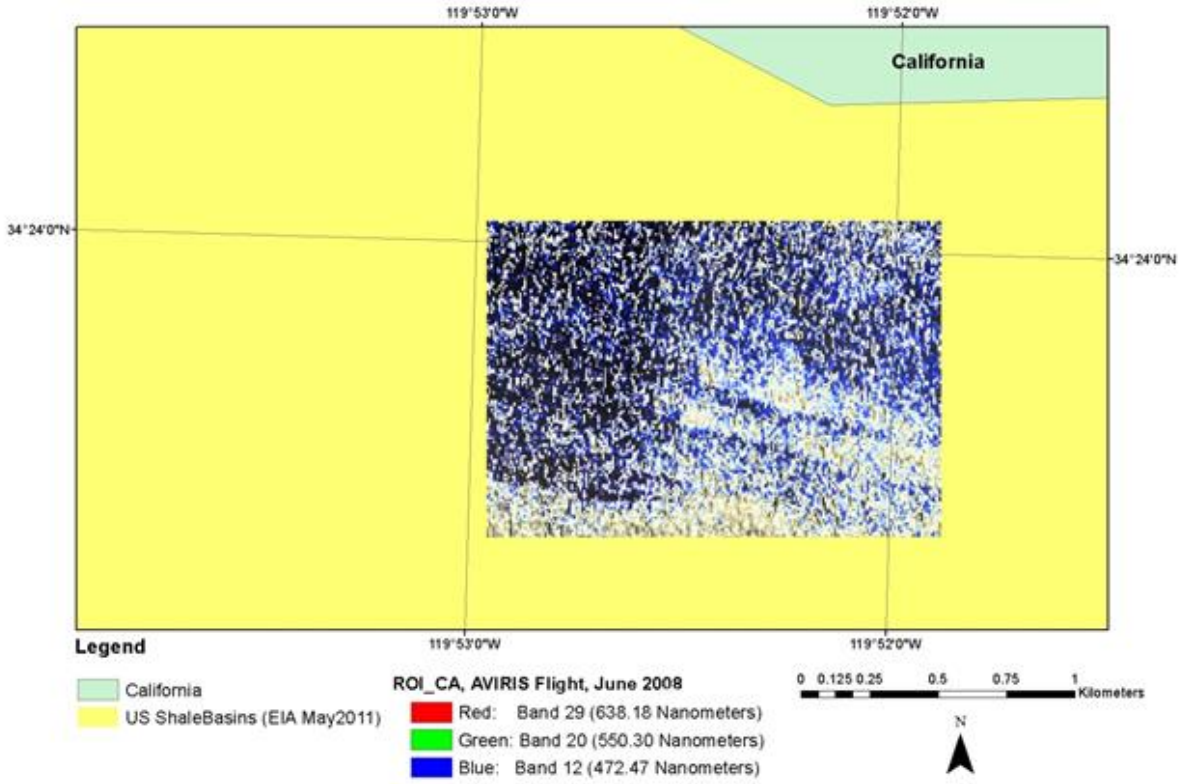

Figure 14- ROI_CA in true colour during AVIRIS_CA flight (JPL/NASA, 2015) over coal and oil point (U.S. EIA, 2015c), CA, USA (ArcGIS, 2012a)

The information of the centre point of ROI_CA is given in Table 5. The information in Table 5 was used to find relative humidity (Fig. 33a in Appendix B) pressure (Fig. 34a in Appendix B), temperature (Fig. 35a in Appendix B), and irradiance spectrum (Fig. $39a_1$ in Appendix B) profile during the flight over the ROI_CA.

Table 5- ROI_CA information of the centre point

Coordinates at centre point		Time (Local)	Spatial Resolution (m^2)
34°24'1.16"N	119°52'41.07"W	~12:50:00	7.4m*7.4m

2.3.2.2 AVIRIS Flight, PA, USA (AVIRIS_PA)

On 6-July 2009, there was an AVIRIS flight over Marcellus shale basin, PA, USA, as it is shown in Fig.15. Throughout this document this flight is called "**AVIRIS_P**ennsylvani**a**" (AVIRIS_PA). Locations of the shale gas wells in the Marcellus shale basin in PA by Feb. 2015 were retrieved from U.S. EIA (2015c). The completed shale gas wells by July 2009 (date of the AVIRIS flight over Marcellus shale basin) were extracted out of all completed wells by Feb. 2015.

As it is shown in Fig. 15, two ROIs were chosen across AVIRIS_PA, "**R**egion **o**f **I**nterest_**P**ennsylvani**a**_**A**" (ROI_PA_A) and "**R**egion **o**f **I**nterest_**P**ennsylvani**a**_**B**" (ROI_PA_B).

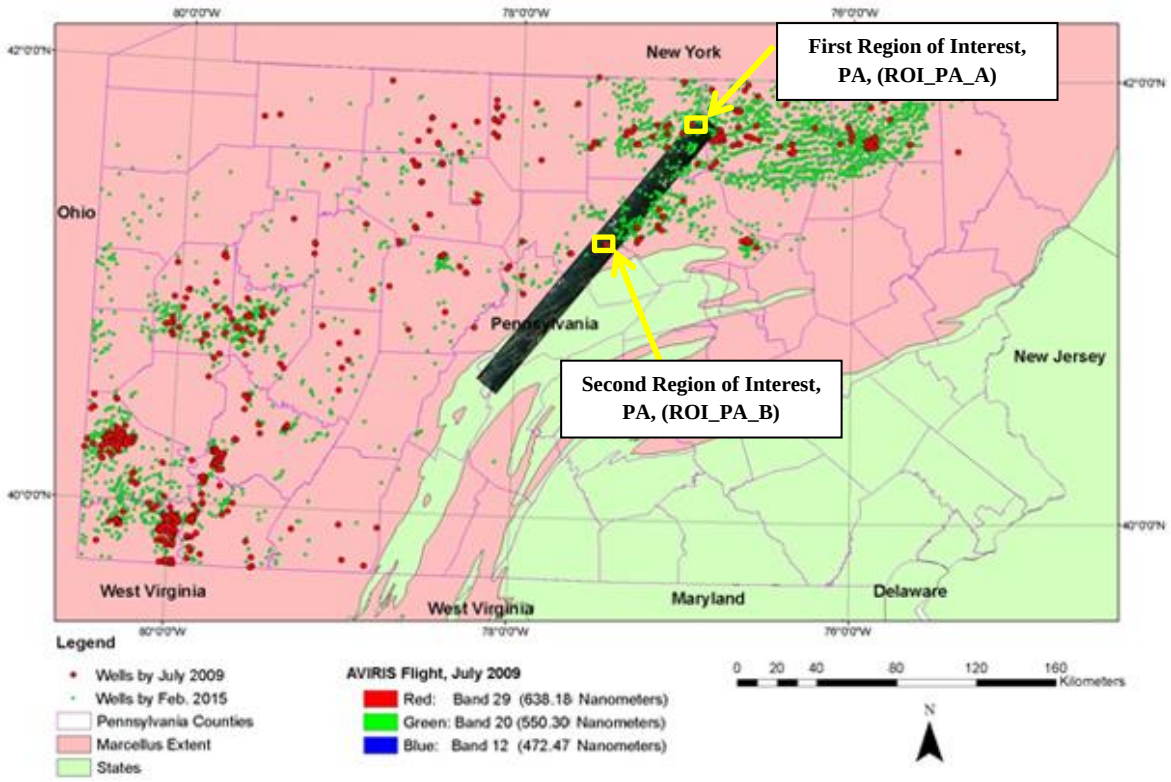

Figure 15- AVIRIS flight (JPL/NASA, 2015) in true colour and well locations (U.S. EIA, 2015c) over Marcellus shale basin(U.S. EIA, 2015c) PA, USA (ArcGIS, 2012a)

The flight information is written in Table 5, and was retrieved from metadata of the flight provided by JPL/NASA. The flight information was used to find irradiance spectrum, atmospheric gas mixture, pressure, and temperature profile during the flight over the ROI_PA_A and ROI_PA_B.

Table 6- AVIRIS_PA flight information

Date	Time (Local)		Latitude		Longitude		Altitude (km)
6 July 2009	Start	End	Start	End	Start	End	20
	14:27:06	14:43:00	43.422319	40.58808	-75.094884	-78.149853	

2.3.2.2.1 First Region of Interest, PA, USA (ROI_PA_A)

Across AVIRIS_PA, two ROIs were selected. In Fig. 16, ROI_PA_A along with drilled shale gas wells are shown.

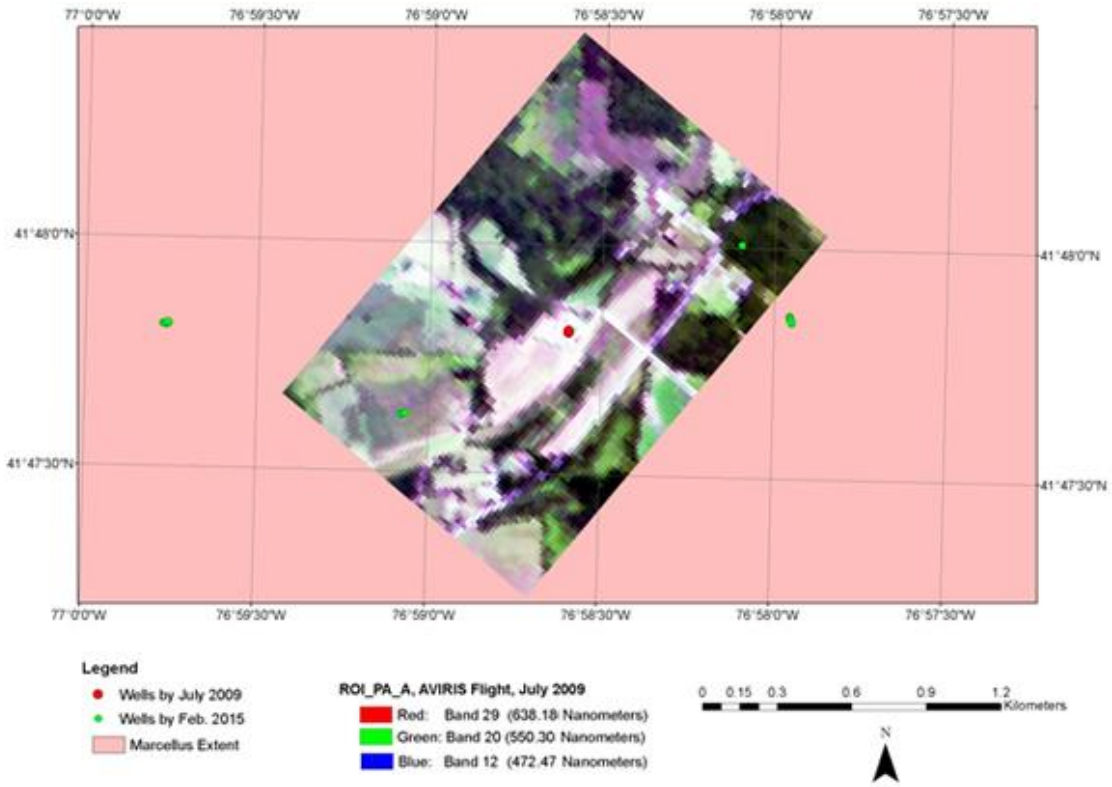

Figure 16- Shale gas wells (U.S. EIA, 2015c) and ROI_PA_A in true colour during AVIRIS_PA flight (JPL/NASA, 2015) over Marcellus shale basin (U.S. EIA, 2015c) PA, USA (ArcGIS, 2012a)

The information of the centre point of ROI_PA_A is given in Table 7. The information in Table 7 was used to find relative humidity (Fig. 33b in Appendix B) pressure (Fig. 34b in Appendix B), temperature (Fig. 35b in Appendix B), and irradiance spectrum (Fig. $39b_1$ in Appendix B) profile during the flight over the ROI_PA_A.

Table 7- ROI_PA_A information of the centre point

Coordinates at centre point		Time (Local)	Spatial Resolution (m^2)
41°48'5.72"N	76°58'43.51"W	~14:40:00	16.1m*16.1m

2.3.2.2.2 Second Region of Interest, PA, USA (ROI_PA_B)

Across AVIRIS_PA, two ROIs were selected. In Fig.17, the ROI_PA_B along with drilled shale gas wells are shown.

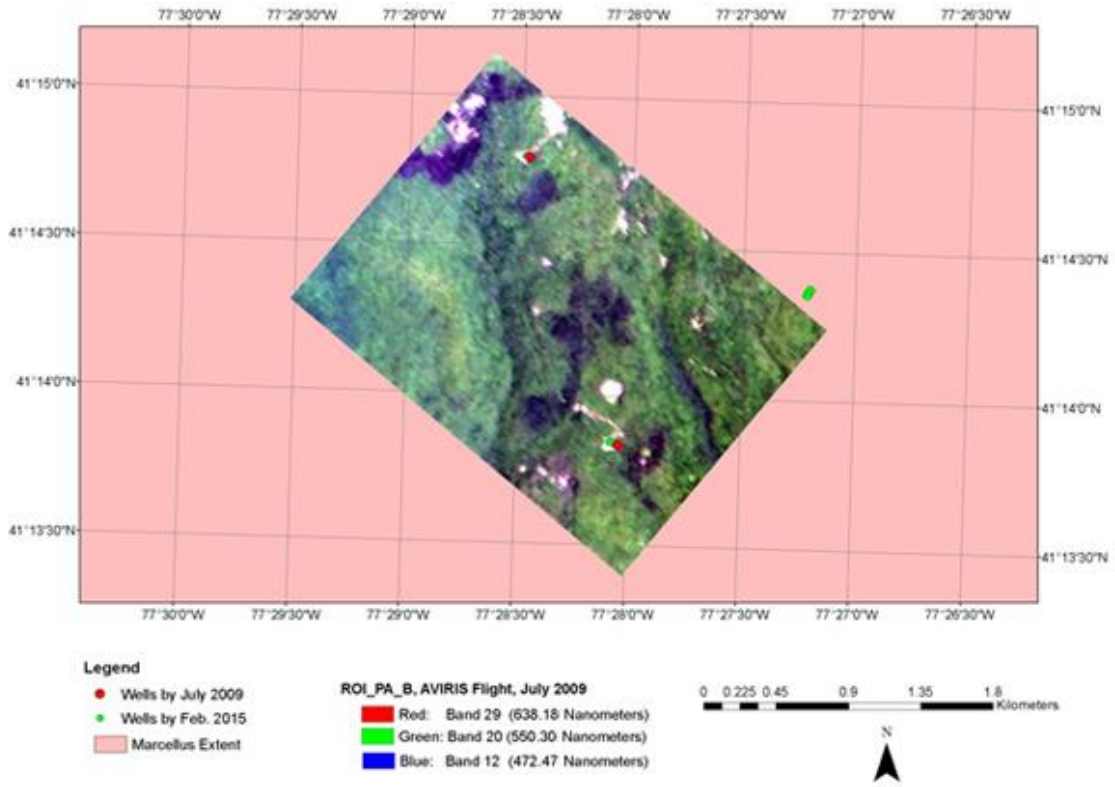

Figure 17- ROI_PA_B in true colour during AVIRIS_PA flight (JPL/NASA, 2015) over Marcellus shale basin(U.S. EIA, 2015c) PA, USA (ArcGIS, 2012a)

The information of the centre point of ROI_PA_B is given in Table 8. The information in Table 8 was used to find relative humidity (Fig. 33b in Appendix B) pressure (Fig. 34b in Appendix B), temperature (Fig. 35b in Appendix B), and irradiance spectrum (Fig. $39b_2$ in Appendix B) profile during the flight over the ROI_PA_B.

Table 8- ROI_PA_B information of the centre point

Coordinates at centre point		Time (Local)	Spatial Resolution (m^2)
41°15'9.40"N	77°28'47.81"W	~14:35:00	16.1m*16.1m

2.3.2.3 ROIs Classification

Neural **n**etwork **c**lassification (NNC) of ENVI is a powerful tool for classifying ROIs for hyperspectral imagery (Subramanian et al., 1997). Over the ROI_CA, which is sea water all across the ROI, it was necessary to consider effects from tides. Based on Diagram 5, pixels across ROI_CA were classified based on tides effects (Fig. $41a_2$ in Appendix B). Samples for considering effects from tides are shown in Fig. $40c_2$ (Appendix B).

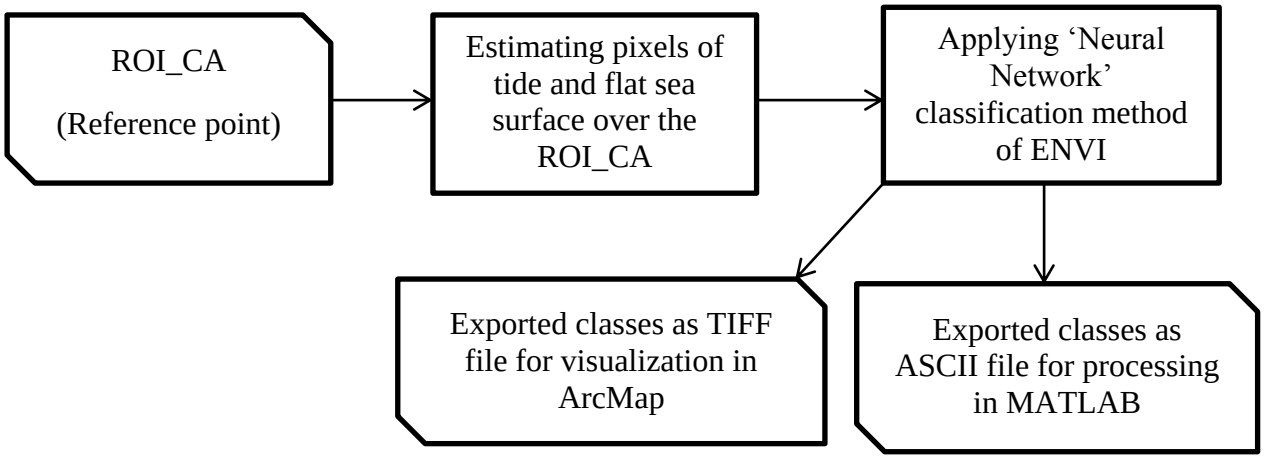

Diagram 5- Steps of classifying tide and flat sea surface at the reference point (ROI_CA)

In this study, samples over ROI_PA_A and ROI_PA_B for land cover classification were picked using Google Earth (Google, 2013) (Table 9). Then spectral separability of samples was statistically tested. Finally, the two ROIs were classified based on samples (Fig. $40a_2$ and Fig. $40b_2$) for each ROI in Pennsylvania as it is shown in Diagram 6.

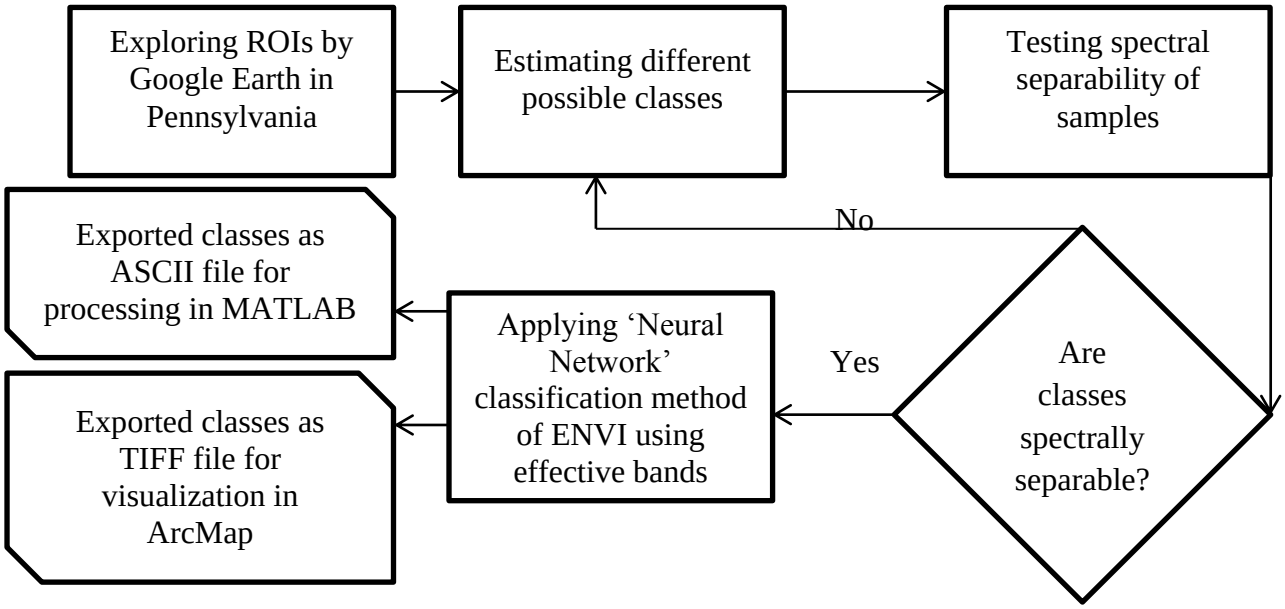

Diagram 6- Steps of land cover classification at ROI_PA_A and ROI_PA_B, PA, USA

The spectral separability test of classes was based on the mean, minimum and maximum DN values of selected samples for each class to analyse if the classes are spectrally separable.

Neural network is designed to classify land cover based on recognition of human (Ndehedehe, Ekpa, Simeon and Nse, 2013). In Table 9, possible available land cover classes across ROI_PA_A and ROI_PA_B based on the author's recognition using Google Earth over the ROIs are shown.

Table 9- Observed land cover classes using Google Earth based on the author's recognition

ROI	Observed Classes from Google Earth						
ROI_PA_A	Deciduous	Conifer	Grass	Light Bare Soil	Dark Bare Soil	Urban	Paving
ROI_PA_B	Bare Soil	Vegetation	Water	-	-	-	-

In Table 10, selected bands for discriminating land cover classes, as they are mentioned in Table 9, across ROI_PA_A and ROI_PA_B, are shown. The bands were selected based on spectrums across the three ROIs (Fig. 40 in Appendix B).

Table 10- Selected spectral AVIRIS band to apply neural network classification using ENVI

ROI	Spectral AVIRIS Bands for Classification				
ROI_PA_A	35	46	71	135	197
ROI_PA_B	47	69	93	139	-
ROI_CA	19	55	94	-	-

2.3.3 High resolution transmission (HITRAN) database

High resolution **tran**smission (HITRAN) molecular absorption compilation and database were established by in 1960s by noticeable and high effort from the Air Force Geophysics Laboratory (AFGL) (Rothman et al., 1986). A wide variety of computer codes uses HITRAN for simulating transmission and light emission in atmosphere. Currently HITRAN (Harvard-Smithsonian Center for Astrophysics (CFA), Cambridge, MA and V.E. Zuev Insitute of Atmosperic Optics (IAO), Tomsk, 2015) is available on web (http://hitran.iao.ru/). In this study, HITRAN was used to model atmospheric transmission above the study area up to the flight height. Diagram 7 demonstrates general steps of methane emission mapping and evaluation.

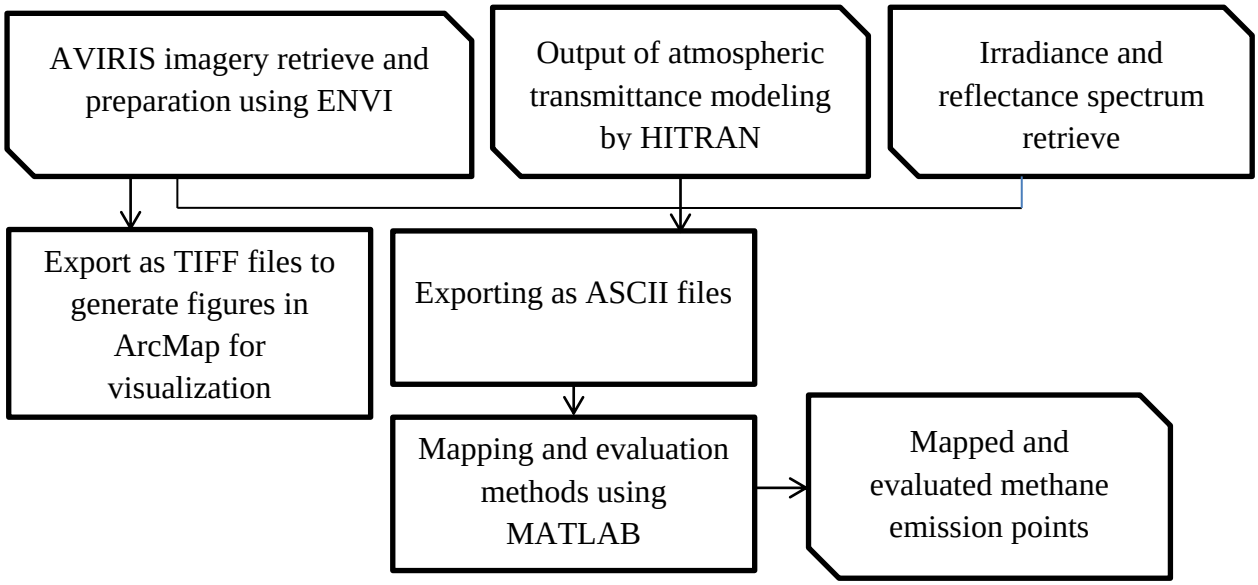

Diagram 7- General steps of methane emission mapping and evaluation

2.3.3.1 Atmospheric Transmittance Modelling

In order to calculate flux of natural methane emissions from natural seeps and probable methane emissions at the shale gas well pads, atmospheric transmittance spectrums from ground level (H=0) up to flights' height were modelled using HITRAN on web (http://hitran.iao.ru/).

2.3.3.1.1 Atmospheric Transmittance Modelling Diagram

In order to use HITRAN on web, for the two flights, gas mixture, temperature and pressure profile from H=0 up to flight height were prepared. In Diagram 8, the detailed steps of data preparation before running HITRAN and how the outputs were used are demonstrated.

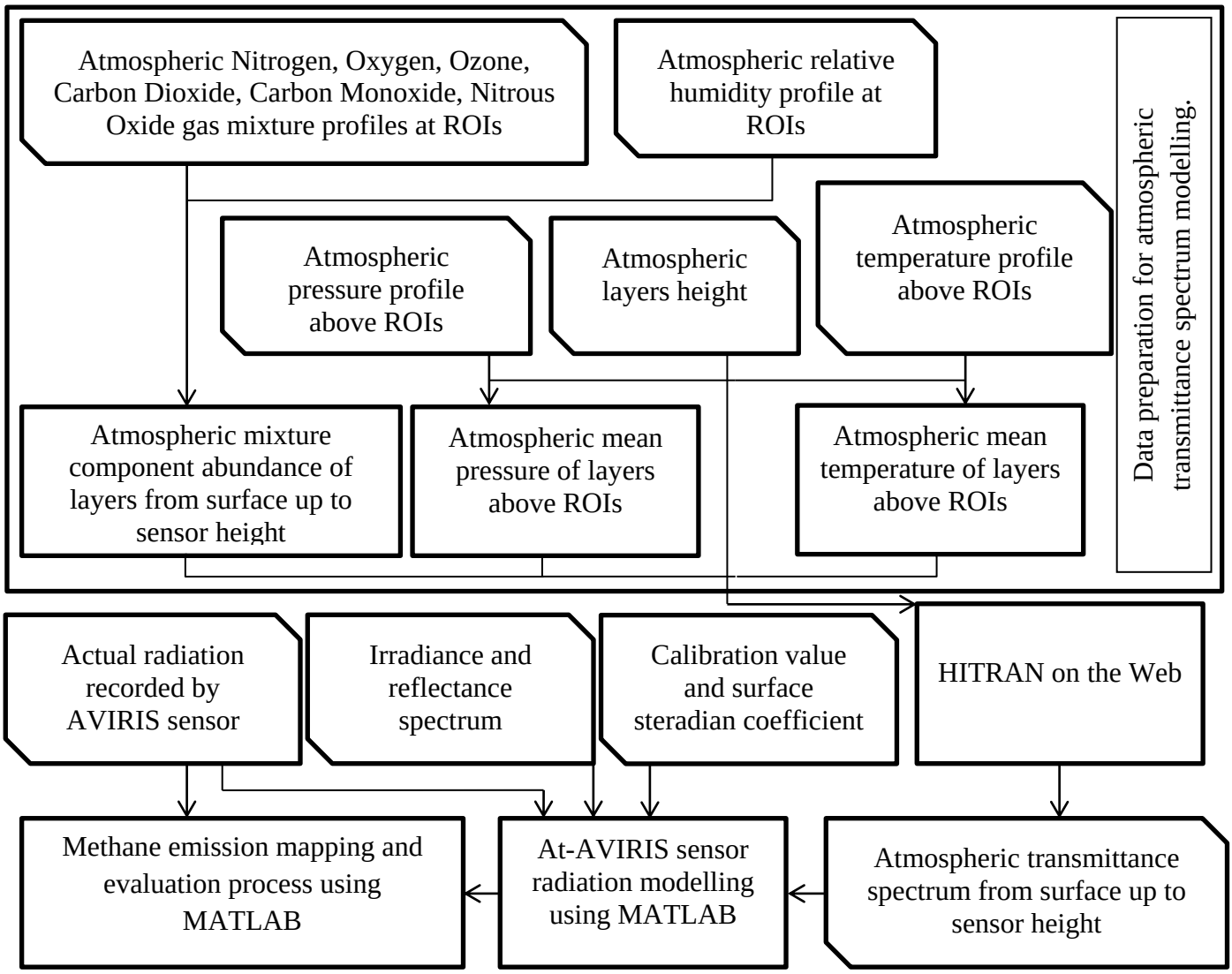

Diagram 8- Steps of HITRAN atmospheric modelling data preparation and its relationship with methane emission mapping and evaluation

2.3.3.1.2 Atmospheric Gas Mixture Profile

Generally, the mixing ratio in the atmosphere is as shown in Fig.18. In this study, US summer gas mixture standard atmospheric model at high latitudes for AVIRIS_PA, and US summer gas mixture standard model at mean latitudes for AVIRIS_CA, were considered at ground level (H=0) based on the location and flights' date. From the US standard atmospheric model, atmospheric gas mixture of Nitrogen (N_2), Oxygen (O_2), Carbon Monoxide (CO), Ozone

(O_3), CO_2, N_2O and CH_4 were used at H=0, and then using Fig. 18 the mixing ratio of the gases were estimated up to each flight's height. Vertical profiles of atmospheric relative humidity (RH) (Fig. 33 in Appendix B), pressure (P) (Fig. 34 in Appendix B), and temperature (T) (Fig. 35 in Appendix B) during the flights' times and locations were requested from **A**tmospheric **C**orrection **P**arameter **C**alculator (ACPC) website of NASA.

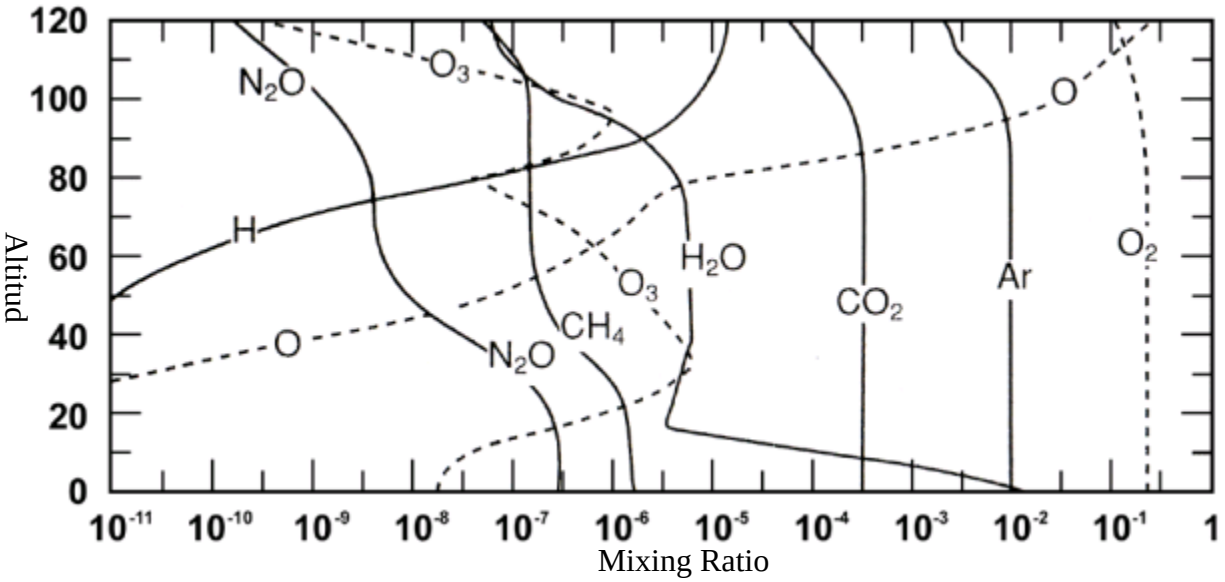

Figure 18- Atmospheric Gas Mixture Profile, adopted from Brasseur et al. (1999; p. 9) in Schlatter (2009, p.21)

2.3.3.1.3 Pressure, Temperature and Relative Humidity Profile

In order to model atmospheric transmittance from ground level (H=0) up to flights' height over the ROIs in PA and CA, first it was necessary to find data of atmospheric gas mixture in the time of flights. The P, T and RH for the AVIRIS_PA were available from 367 meter height while for AVIRIS_CA they started from 6 meter height. So, from H=0 up to H=367 meter extrapolations were done for P, T and RH for AVIRIS_PA but not for AVIRIS_CA. Based on RH, P and T, H_2O profiles, H_2O mixing ratio was calculated using New York City Meteorological Network (NYCMetNet) website (The Optical Remote Sensing Laboratory of The City College of New York, 2012).

2.3.3.1.4 Atmospheric Layers

In order to complete data preparation to use HITRAN on the web, the atmosphere above ROIs was separated into layers. The atmosphere above AVIRIS_PA, AVIRIS_CA was separated into 21 and 12 layers respectively, based on the available data. And finally, by getting mean value for gases, P and T along the height of each atmospheric layer, data preparation to model atmospheric transmittance was completed (Table 22 and Table 23 in Appendix B).

2.3.3.1.5 Atmospheric Layers above AVIRIS_CA

The flight altitude over Pennsylvania on 19-June 2008 was at altitude of 10 km. The atmosphere between AVIRIS_CA and ground lever was separated into 12 layers (Table 22 in Appendix B). The first layer was considered from H=0 up to H=100 m, second layer from

H=100 m up to H=500 m, third layer from H=500 m up to H=1 km and from H=1 km up to H=10 km one layer for every 1 km was defined.

2.3.3.1.6 Atmospheric Layers above AVIRIS_PA

The flight altitude over Pennsylvania on 6-July 2009 was at an altitude of 20 km. The atmosphere between AVIRIS_PA and ground lever was separated into 21 layers (Table 23 in Appendix B). The first layer was considered from H=0 up to H=367 m, second layer from H=367 m up to H=1 km, and from H=1 km up to H=20 km one layer every for 1 km was defined.

2.3.3.1.7 Reflectance Spectrum

Reflectance spectrum for each class was retrieved from ASTER Spectral Library of JPL/NASA (ASTER/NASA, 2015). In Fig. 42 (Appendix B), reflectance spectrums of different classes are shown.

2.3.3.1.8 Irradiance Spectrum

At-surface irradiance spectrum at the estimated time when AVIRIS aircraft was flying over ROIs was retrieved using solar spectrum calculator of **p**hoto**v**oltaic (PV) light house website (PV Lighthouse, 2015). The at-surface spectrums are shown in Fig. 39 (Appendix B). In order to validate the spectrum from PV light house website, integration of at-surface spectrums were compared with real data of total amount of energy received from sun at surface. The total amount of energy received from sun was retrieved from **E**arth **S**ystem **R**esearch **L**aboratory (ESRL) of **N**ational **O**ceanic and **A**tmospheric **A**dministration (NOAA) (ESRL/NOAA, 2015) and shown in Fig. 39 (Appendix B).

2.3.4 Calibration Values and Steradian Coefficient Calculation

The unit of at-surface irradiance is ($W/(nm.m^2)$), and unit of recorded radiation by AVIRIS; after conversion from ($\mu W/(nm.cm^2.st)$), is ($W/(nm.m^2.st)$). In order to find calibration value and steradian coefficient of each pixel, the band with maximum transmittance was considered (Diagram 9). As it is shown in Fig. 36 (Appendix B), at band 73 there is the highest value of atmospheric transmittance which is 0.99996, so at this band there is almost no effect from atmospheric gases. The calibration values and steradian coefficients are shown in Fig. 41 (Appendix B).

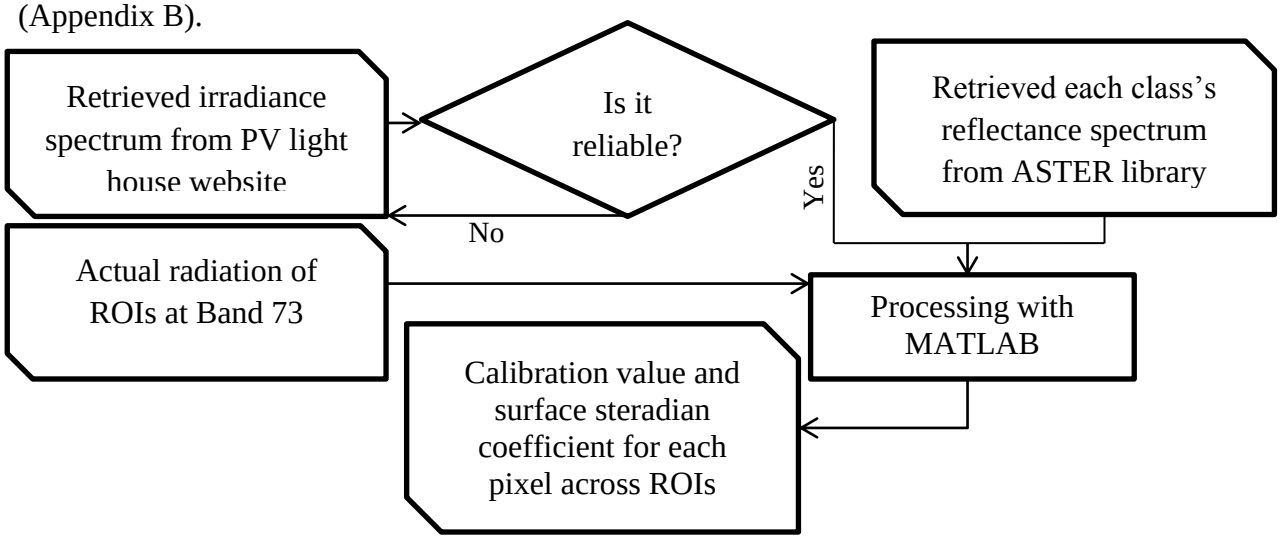

Diagram 9- Steps of calibration values and surface steradian coefficients calculation

Based on the fact that there is almost no atmospheric effect at band 73, in order to find the calibration value and steradian coefficient for each pixel, irradiance and reflectance spectrums and actual radiation recorded by AVIRIS was considered. The ratio of irradiance times reflectance for each pixel over the actual radiation at band 73 gives calibration value and steradian coefficient of each pixel.

2.3.5 Actual Radiation of AVIRIS imagery

In order to map and evaluate amount of possible methane emissions over the ROIs, several steps were taken. In Diagram 10, steps of AVIRIS imagery preparation for mapping and evaluating methane emission are shown. In order to convert DN values to actual radiation, gain values in Table 24 (Appendix B) were used. Note that "Dark object Subtraction" (DOS) is almost the most common method to remove atmospheric path radiation (Cheng et al., 2012).

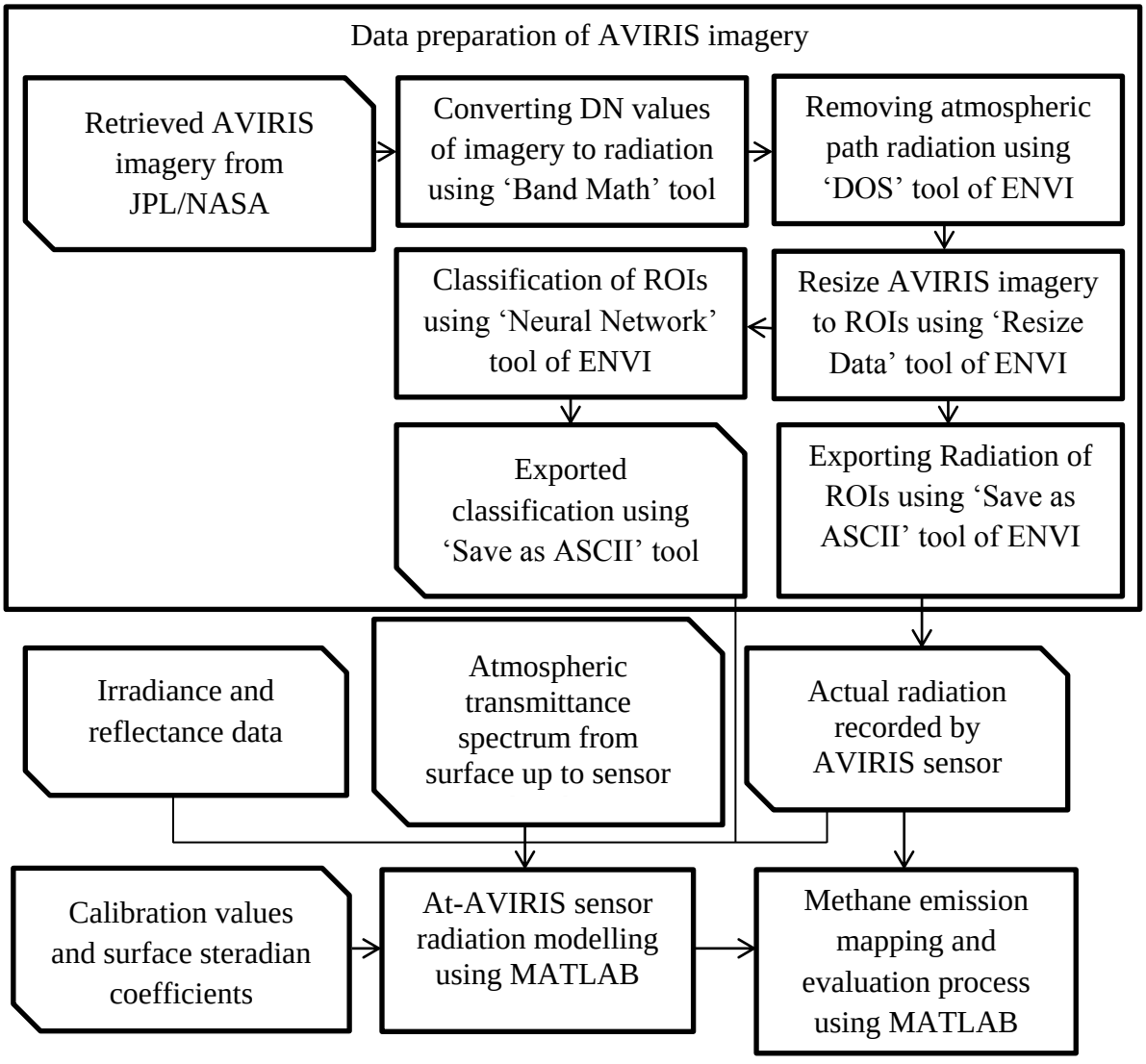

Diagram 10- Steps of actual radiation of AVIRIS imagery preparation and its relationship with methane emission mapping and evaluation

2.3.6 Core Equations

The main equations used in this study are Planck's law and Beer-Lambert's law. Planck's law was used to introduce a new methane emission mapping technique. Beer-Lambert's law is one of the main laws for HITRAN to model atmospheric transmittance spectrum.

2.3.6.1 Planck's Law (Energy Element)

In quantum physics, according to Planck's law, the energy of each element is only proportional to its frequency.

$$\mathbf{E = h * \nu} \qquad \textbf{Equation 5}$$

where, h is planck's constant and ν is the frequency of energy element. It is assumed that for each AVIRIS band there is an energy element. So, based on Eq. 5 radiation times the nominal wavelength of the energy element should be the same at different bands. The band interval for AVIRIS is about 10nm (Table 24 in Appendix B). So, for the bands where there is absorption from atmospheric gases subtracting two effective bands gives negative values. Effective bands are those bands by which a gas plume can be detected. A new methane emission mapping technique is introduced in this study using Eq. 5.

2.3.6.2 Planck's Law (Black Body Radiation)

According to planck's law every object with temperature greater than 0 k, has "**B**lack **B**ody" (BB) radiation. Emissivity (ε) which has value from 0 to 1 shows how objects behave like ideal BB; for the ideal BB emissivity is equal to 1.

$$\mathbf{B_\lambda(\lambda, T) = \frac{2hC^2}{\lambda^5} * \frac{1}{e^{\frac{hC}{\lambda kT}} - 1}} \qquad \textbf{Equation 6}$$

where, C is light speed, λ is wavelength, h is Planck constant, k is Boltzman constant and T is temperature. In Table 5, the contants value along with the SI units are given.

Table 11- Constants and units of Planck's law

B_λ	Speed of light	λ (wavelength)	h (Planck constant)	k (Boltzman constant)	T
$w \cdot sr^{-1} \cdot m^{-3}$	299792458 $m.s^{-1}$	meter	$6.62606957(29) \times 10^{-34}$ J.s	$1.3806488(13) \times 10^{-23}$ JK^{-1}	kelvin

$$L_{at-Sensor} = L_{atmospheric-Path} + B_\lambda * \tau_{atmosphere} + \frac{E_{irr}}{steradiance\ factor} * \rho * \tau_{atmosphere} * \tau_{plume}$$

Equation 7

where $L_{at\text{-}sensor}$ is radiation (watt/(nm.m^2.st)) recorded by AVIRIS, $L_{atmospheric\text{-}Path}$ is atmospheric path radiance (watt/(nm.m^2.st)), E_{irr} is at surface irradiance (watt/(nm.m^2)), B_λ is BB radiation of gas plume, ρ is surface reflectance and τ is transmittance for the area where there is no plume, τ_{plume}=1. In order to remove atmospheric path radiation, DOS tool of ENVI was used. Eq. 7 was reduced to Eq. 8.

$$\mathbf{L_{at-Sensor}} = \mathbf{B_{\lambda}} * \boldsymbol{\tau}_{\mathbf{atmosphere}} + \frac{E_{irr}}{steradiance\ coefficient} * \boldsymbol{\rho} * \boldsymbol{\tau}_{\mathbf{atmosphere}} * \boldsymbol{\tau}_{\mathbf{plume}} \quad \textbf{Equation 8}$$

2.3.6.3 Beer-Lambert's law

Beer-Lambert's law expresses that if light travels through a medium with optical depth of l and absorption coefficient of β, transmission can be calculated according to Eq. 10.

$$\boldsymbol{\tau}(\mathbf{l}, \boldsymbol{\beta}) = \boldsymbol{e}^{(-\boldsymbol{\beta} * \boldsymbol{l})} \quad \textbf{Equation 9}$$

where β known as absorption coefficient, is in the unit of $cm^2 .mol^{-1}$ and l has unit of cm.

$$\boldsymbol{\beta}(\boldsymbol{\omega}) = \mathbf{N}(\mathbf{P}, \mathbf{T}) \sum_{i=1}^{q} \boldsymbol{n}^{(i)} * \sum_{j=1}^{q(i)} \boldsymbol{I}^{(ij)}(\mathbf{T})\, \boldsymbol{\Phi}(\boldsymbol{\omega}, \boldsymbol{\omega}^{(\mathbf{ij})} - \boldsymbol{\omega}, \boldsymbol{\omega}^{(\mathbf{ij})} + \boldsymbol{\omega}; \mathbf{P}, \mathbf{T}) \quad \textbf{Equation 10}$$

where $I^{(ij)}$ is the integral intensity of the j^{th} line for the i^{th} isotopic species, Φ(ij) is the line shape of the j^{th} line, N is the volume concentration of all gas molecules at the pressure P and temperature T.

2.3.7 Methane Emission Mapping Techniques

In order to evaluate the amount of methane emissions, it was necessary to first map possible areas of methane emission. In this study, two mapping techniques were applied; band ratio and residual energy techniques. Residual energy is a new technique which is introduced in this thesis.

2.3.7.1 Band Ratio Technique

Band ratio for mapping methane emission pixels by AVIRIS was used by others(Leifer et al. 2006; Roberts et al. 2010; Bradley et al. 2011) . Among all AVIRIS introduced bands (Leifer et al., 2006; Bradley et al., 2011; Roberts et al., 2010) for this technique, the author of this study noticed band 202 as nominator and band 177 as denominator produce better results in ROI_CA. Based on the output of HITRAN, band 202 (Fig. 36 in Appendix B) represents the wavelength range of atmospheric CH_4 absorption, and band 177 represents atmospheric absorption by H_2O and CO_2 (Fig. 37 in Appendix B). The constraints mentioned in Diagram 11 were based on band 202 and band 177 scatter plot described in Bradley et al. (2011, p. 2).

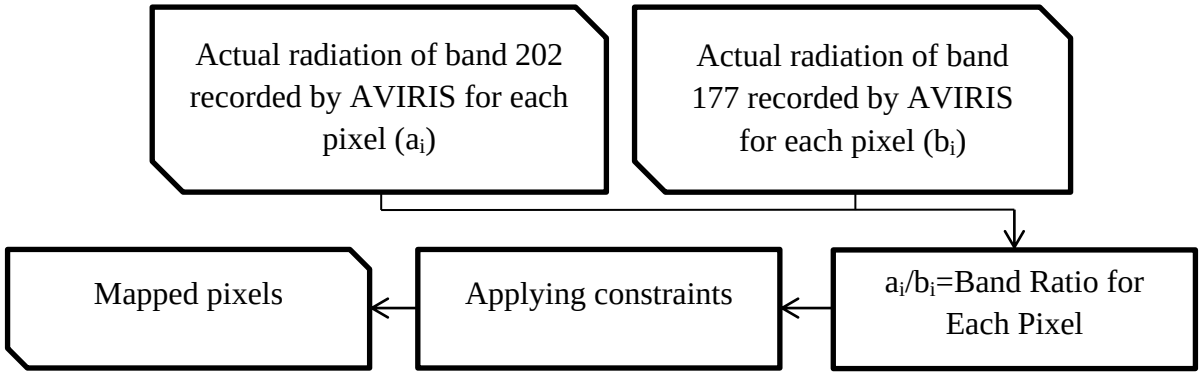

Diagram 11- Steps of band ratio method for methane emission mapping

2.3.7.2 Residual Energy Technique

In 2013, it was claimed that the band ratio technique is not capable for terrestrial areas (Thorpe et al., 2013), so cluster-tuned matched filter over ROI_CA and also terrestrial area in Inglewood, Los Angeles, USA was introduced where are both known for CH_4 emissions. The residual energy technique with application to AVIRIS for mapping methane emissions is introduced in this thesis. The residual energy technique works well using band 202 and 177 for methane emission mapping on the same areas that Thorpe et al. (2013) studied. The results of the new technique by this study matched the previous works (Fig. 42, and Fig. 43 in Appendix C), so the residual energy technique for mapping methane emissions in ROI_PA_A and ROI_PA_B was used. The residual energy technique is based on Planck's law (Eq. 5) and radiation residual technique introduced by Roberts et al. (2011).

2.3.8 Radiation Modelling at Sensor Height

In order to estimate atmospheric methane concentration at mapped pixels, by using Eq. 8, Eq. 9 and Eq. 10, it is necessary to model at-sensor radiation using the atmospheric transmittance spectrum (HITRAN output), irradiance spectrum along with calibration values and steradian coefficients and reflectance spectrum of each class at ROIs. In Diagram 12, general steps of at-sensor radiation modelling are explained. The MATLAB code of the radiation modelling is provided in Appendix D.

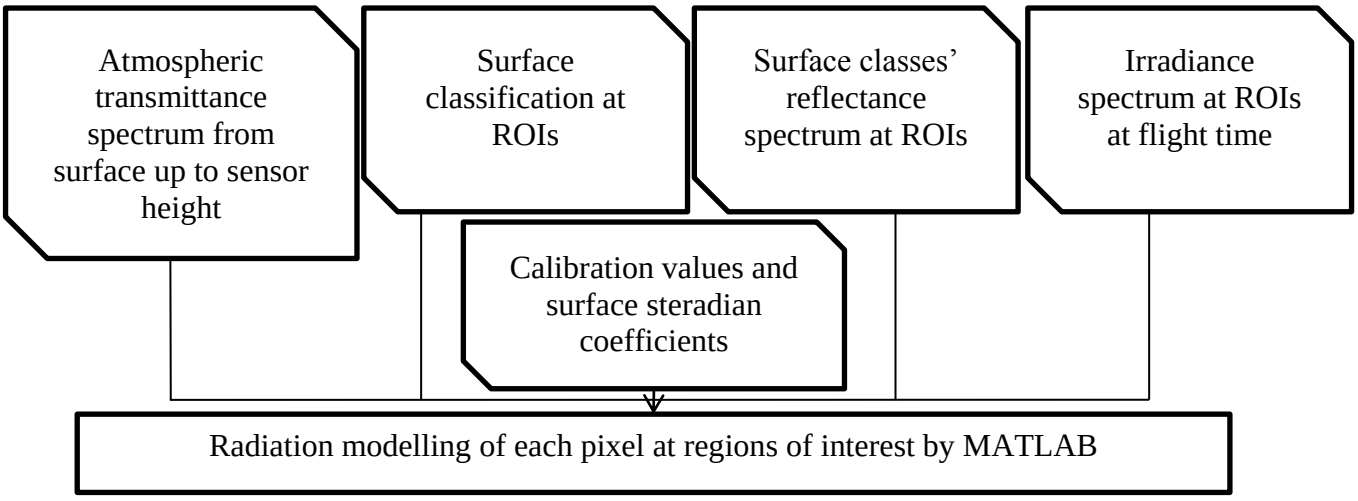

Diagram 12- General steps of at-sensor radiation modelling

2.3.9 Fugitive Methane Evaluation

After mapping and finding change in atmospheric concentration of methane (ppb), based on the known flux of methane emission at the reference point (ROI_CA), possible fluxes of fugitive emission in ROI_PA_A and ROI_PA_B were estimated. In Diagram 13, steps of how the flux estimation at the reference point (ROI_CA) was done are demonstrated.

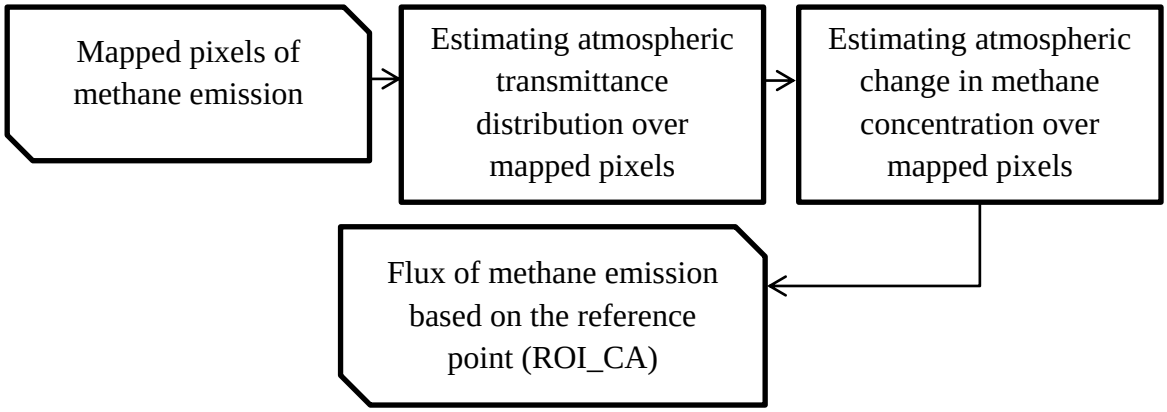

Diagram 14- General steps of methane emission evaluation

2.3.9.1 Atmospheric change in Methane concentration

By reconstructing Eq. 8 to Eq. 11, plume transmittance over mapped pixels was estimated.

$$\boldsymbol{\tau}_{plume}^{i} = \frac{(actual\ radiation_{202}^{i} - B_{\lambda} * \tau_{atmosphere})}{at-sensor\ radiation\ model_{202}^{i}} \qquad \textbf{Equation 11}$$

Finally, actual transmittance over mapped areas was estimated by multiplying plume transmittance to atmospheric transmittance at band 202.

After calculating transmittance over mapped pixels, atmospheric methane concentrations over mapped pixels were estimated using Eq. 9.

2.3.9.2 Fugitive Methane Emission Flux

The most important part of this study in methane emission evaluation was calculating fugitive methane emission over natural gas production per each shale gas well in ROI_PA_A and ROI_PA_B. After calculating methane concentration at mapped pixels, the methane concentration per unit of area was calculated at ROI_CA, ROI_PA_A and ROI_PA_B. The methane emission flux is known for ROI_CA till 1998 (Quigtey et al., 1999), so the flux evaluation in ROI_PA_A and ROI_PA_B in 2008, were calculated based on the range of methane emission in ROI_CA mentioned by Quigtey et al. (1999). In Diagram 14, general steps of methane emission flux calculation are written.

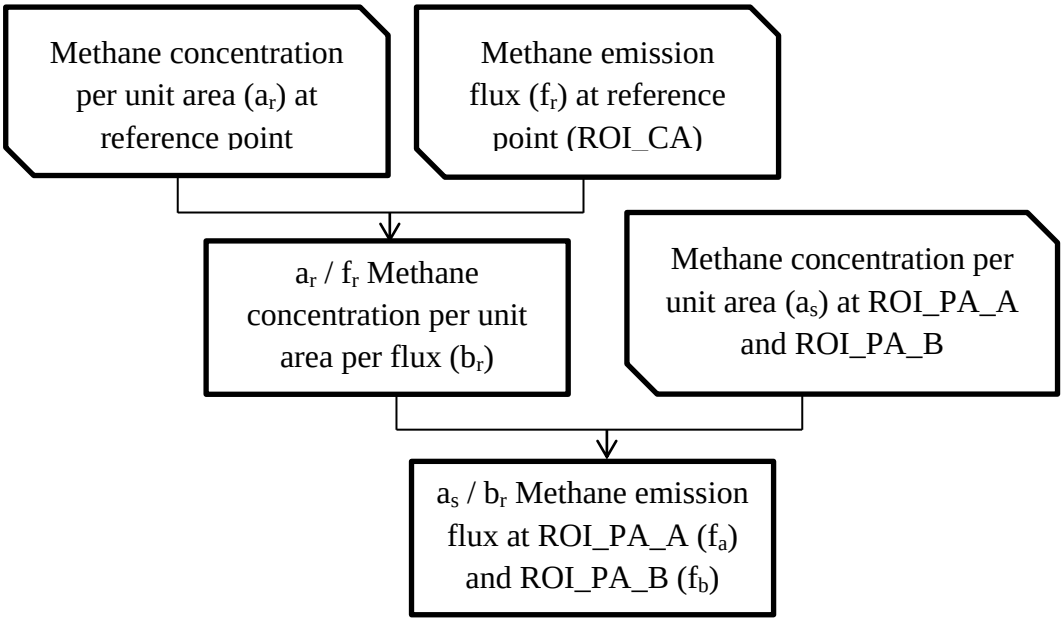

Diagram 154- Steps of fugitive methane emission flux estimation at ROI_PA_A and ROI_PA_B

In oil and gas sector fugitive methane emission is calculated in percentage by Eq. 12 (Howarth, Santoro and Ingraffea, 2011).

$$\textbf{Fugitive Methane Emission}\ (\%) = \frac{\textbf{fugitive emission flux}}{\textbf{Production flux}} * \mathbf{100} \qquad \textbf{Equation 12}$$

So, in order to evaluate the flux of fugitive methane emission in percentage, it is just required to know the natural gas production plus the flux of fugitive methane emission.

3 Results and Discussions

In this chapter, results of climate simulations and methane emissions mapping and evaluation are presented and discussed.

3.1 Climate Simulations

The main and core outputs of climate simulations by the EdGCM are shown in Fig. 19 and Fig. 20. In Fig. 19, the three global maps are presenting anomalies of "Age of Natural Gas" (ANG) scenario no. 5 based on ANG control run in 2021-2030 (Fig. 19a), 2031-3040 (Fig. 19b) and 2041-2050 (Fig. 19c). In this study it was assumed that ANG control run is representative of global real temperature. As it was expected, the global mean temperature is less in ANG scenario no.5 compared to ANG control run, but which is more important is the ANG scenarios anomalies based on ANG control run which are presented in Table 15.

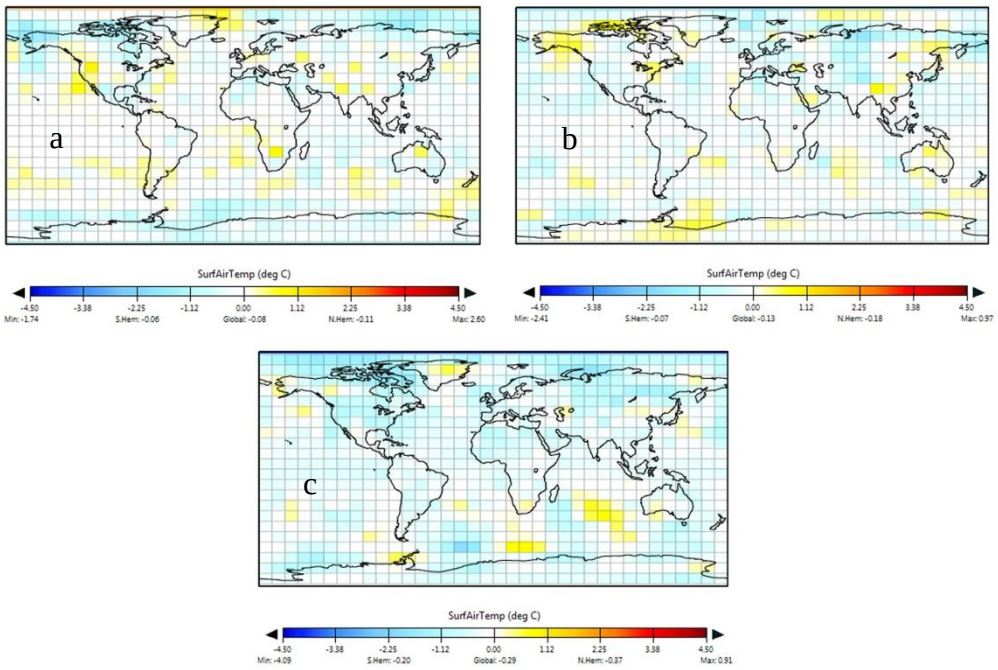

Figure 19- Global decadal temperature anomaly in ANG scenario no.5, visualized by EVA, the (a) map is from 2021 until 2030, the (b) map is from 2031 until 2040, and the (c) map is from 2041 until 2050

The outputs of EdGCM for all ANG scenarios show that the cooling effects of reducing atmospheric CO_2 in northern hemisphere is larger than southern hemisphere which is also reported by IPCC (2007).

After, exporting the maps by EdGCM as ASCII files, the information was used in MATLAB to plot Fig. 20. Although the trends show increase in global mean temperature in Fig. 20 and satisfy the output maps of the EdGCM (Fig. 19), it seems ASCII exporting tool of EdGCM is not working well, as there is no difference between ANG scenarios and ANG control run until 2035. However the positive slope of the trends (Fig. 20) are as expected and further evaluations were based on information taken from output maps of the EdGCM (Fig. 20).

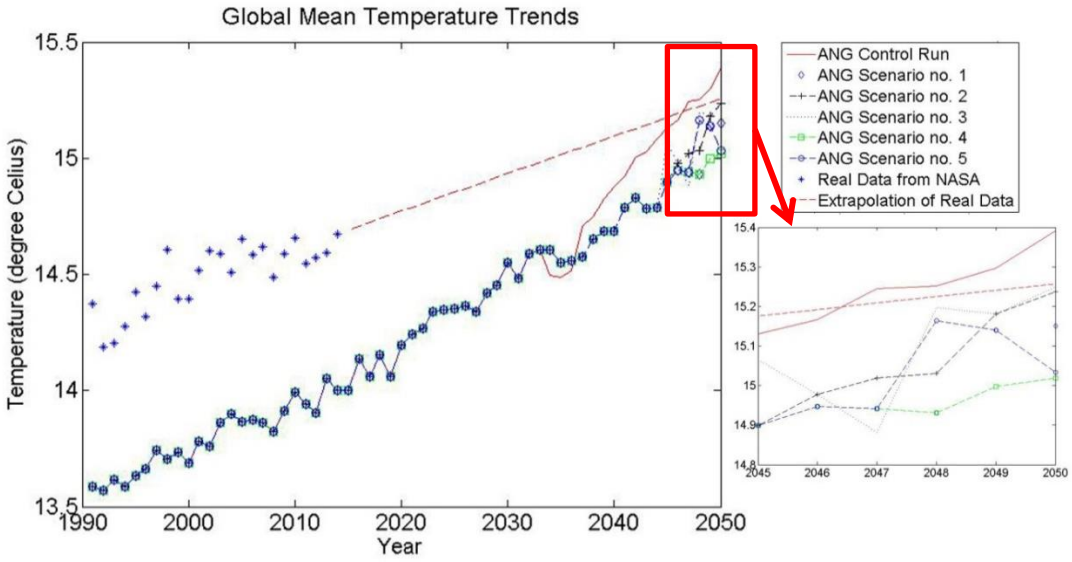

Figure 20- Global temperature trends in ANG scenarios, real data is from GISS/NASA (2015), and linear extrapolation of real data

As it is shown in Fig. 20, it is obvious that the EdGCM there is a gap between the EdGCM outputs and real data. The control run is representative of global mean temperature and ANG scenarios anomalies are based on the ANG control run.

In Table 12, the linear fitting model (Eq. 1) over real data and ANG scenarios (Table 1) are presented. In a report of the IPCC (2014a), the use of linear fitting model over temperature data was reported. As it can be understood from R-Square of linear fitting model over real data, the global mean temperature increases linearly and the ANG scenarios follow linear increase as well, but the slope of increase in ANG scenarios is almost two times higher than the slope of increase in reality. In Table 12, a is the slope value and b is the intercept value of the linear fitting models over outputs of ANG simulations by the EdGCM. In Table 12, the fourth column show the ratio between slope of each scenario's fitting model (a_i) over the slope of real data's fitting model ($a_{real\ data}$).

Table 12- Fitting properties over real data and the ANG scenarios

	a	b (Temperature in 1990)	$a_i/a_{real\ data}$	R-Square
Real Data	0.01248	14.3152	1	0.8272
ANG Control Run	0.02893	13.4007	2.3181	0.9564
ANG Scenario no. 1	0.02527	13.4673	2.0248	0.9804
ANG Scenario no. 2	0.02579	13.4621	2.0665	0.9752
ANG Scenario no. 3	0.02609	13.4591	2.0905	0.9696
ANG Scenario no. 4	0.02483	13.4717	1.9896	0.9847
ANG Scenario no. 5	0.02544	13.4756	2.0385	0.9781

In Table 13, the outputs of global mean temperature simulation under different ANG scenarios are presented in three different decadal periods (2021-2030, 2031-2040, and 2041-2050).

Table 13- Global mean temperature in the ANG scenarios in three different decadal periods (2021-2030, 2031-2040, and 2041-2050)

	2021-2030	2031-2040	2041-2050
ANG Control Run	14.45	14.72	15.16
ANG Scenario no. 1	14.31	14.63	15.03
ANG Scenario no. 2	14.35	14.65	15.04
ANG Scenario no. 3	14.37	14.69	15.04
ANG Scenario no. 4	14.37	14.61	14.90
ANG Scenario no. 5	14.37	14.59	14.87

By assuming that the ANG control run scenario (first column in Table 13) is the representative of global real temperature, potential temperature anomalies in the ANG scenarios (column 3 to column 7 of Table 13) based on the global mean temperature of ANG control run are presented in Table 14.

Table 14- Potential decadal anomalies of the ANG scenarios based on the ANG control run

	2021-2030	2031-2040	2041-2050
ANG Scenario no. 1anomalies	-0.14	-0.09	-0.13
ANG Scenario no. 2 anomalies	-0.1	-0.07	-0.12
ANG Scenario no. 3 anomalies	-0.08	-0.03	-0.12
ANG Scenario no.4 anomalies	-0.08	-0.11	-0.26
ANG Scenario no.5 anomalies	-0.08	-0.13	-0.29

Although, it was assumed that ANG control run is presenting real data but the slop of increase in real global mean temperature were not considered in Table 14. Based on the slope ratio between scenarios and slope of increase in real data presented in Table 12, anomalies in Table 15 were used as actual temperature saved under each ANG scenario.

Table 15- Actual decadal anomalies of the ANG scenarios based on the ANG control run

	2021-2030	2031-2040	2041-2050
Scenario no. 1anomalies	-0.10482	-0.07861	-0.11355
Scenario no. 2 anomalies	-0.08915	-0.0624	-0.10698
Scenario no. 3 anomalies	-0.07215	-0.02705	-0.10822
Scenario no.4 anomalies	-0.06866	-0.09441	-0.22316
Scenario no.5 anomalies	-0.07035	-0.11432	-0.25502

Fig. 21 was plotted based on global mean temperature in pre-industrial era (13.7°C), and values in Table 15.

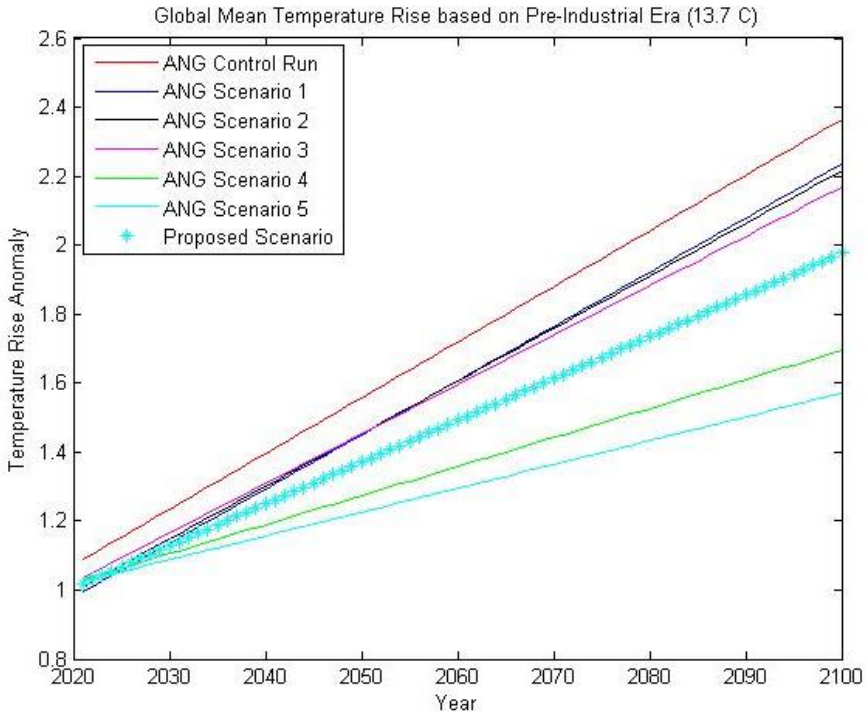

Figure 21- Global temperature anomaly of ANG proposed scenarios based on pre-industrial global mean temperature (13.7°C)

Based on the ANG scenarios (Fig. 21) the author proposes a scenario by which global mean temperature will not pass beyond 2°C policy until 2100 (Table 16 and Fig. 21).

Table 16- Proposed fossil fuel combustion scenario by this thesis study until 2100

Resources	Natural Gas	Oil	Coal
Contribution (%)	58.784	19.24	8.496

Based on World Bank (2010, p. 19) report, adaptation cost for keeping about 2°C policy until 2050 using net sum method is 81.1 billion dollar (2005 USD) per year. Based on Fig. 21, by current anthropogenic anthropogenic GHGs emission we will exceed 2°C policy around 2078, but by implementing the proposed scenario in Table 16, we will exceed at the end of 21st century. So if the energy policy makers follow the proposed scenario in Table 16, by using the Eq. 13, there will be USD 19.82 billion (2005 USD) saved per year. The calculation is based on the assumption that the adaptation costs remain 81.1 billion dollar (2005 USD) per year until end of 2078.

$$\text{Annual saved} = \frac{(2100-2010)*81.1-(2078-2010)*81.1}{2100-2010} \qquad \textbf{Equation 13}$$

3.2 Methane Emission Mapping and Evaluation

In this part, results of mapping and evaluation over the mapped pixels are provided. In Fig. 30 and in Fig. 31 in Appendix B, the introduced methane emission mapping technique,

residual energy, was compared with other studies. As the residual energy technique shows similar patterns in mapping methane emission pixels both in heterogeneous and homogenous areas, this technique was used for evaluation of methane emissions in ROI_CA, ROI_PA_A, and ROI_PA_B. As, this study was desk work, the band ratio technique was considered as a flag, so further evaluations were based on mapped pixels by residual energy method. In Fig. 22d, the absorption anomaly distribution by methane plume is presented where hot points with high value of absorption (14%) are shown in red. Fig. 22e was produced after estimating values in Fig.22d. Comparing Fig. 22e with Fig. 22d show that pixels with higher concentration of atmospheric methane, absorb more energy. By using Fig. 22e and spatial resolution of AVIRIS in ROI_CA methane concentration per square meter over mapped pixels was calculated (Table 17)

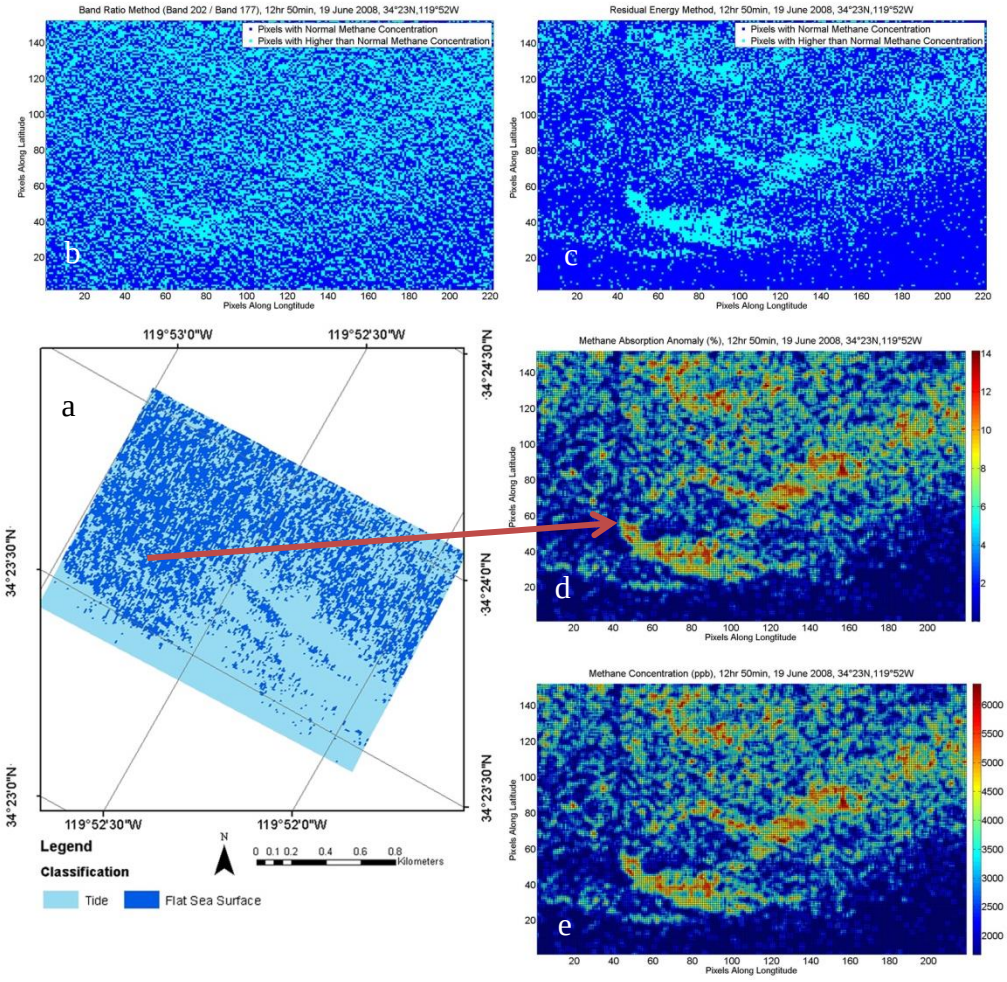

Figure 22- Mapping and evaluation of ROI_CA, the (a) map shows classes in ROI_CA, the (b) shows mapped methane emission pixels by band ratio technique, the (c) shows mapped methane emission pixels by residual energy technique, the (d) shows methane absorption anomaly, and (e) shows atmospheric methane concentration

After verifying the functionality of the new mapping technique, residual energy, the mapping and methane emission evaluation were done over the shale gas exploitation areas; ROI_PA_A (Fig. 23) and ROI_PA_B (Fig. 24). In addition, band ratio technique was also

applied in all ROIs. As it is shown in Fig. 23, there is probable fugitive methane emission from shale gas well-pads in ROI_PA_A. The probable emission increased the absorption by about 2.5% at the hot points (Fig. 23d). After estimating methane absorption (Fig. 23d), methane concentration was calculated (Fig. 23e). Finally, the methane concentration per square meter was calculated in ROI_PA_A over mapped pixels for flux calculation (Table 17).

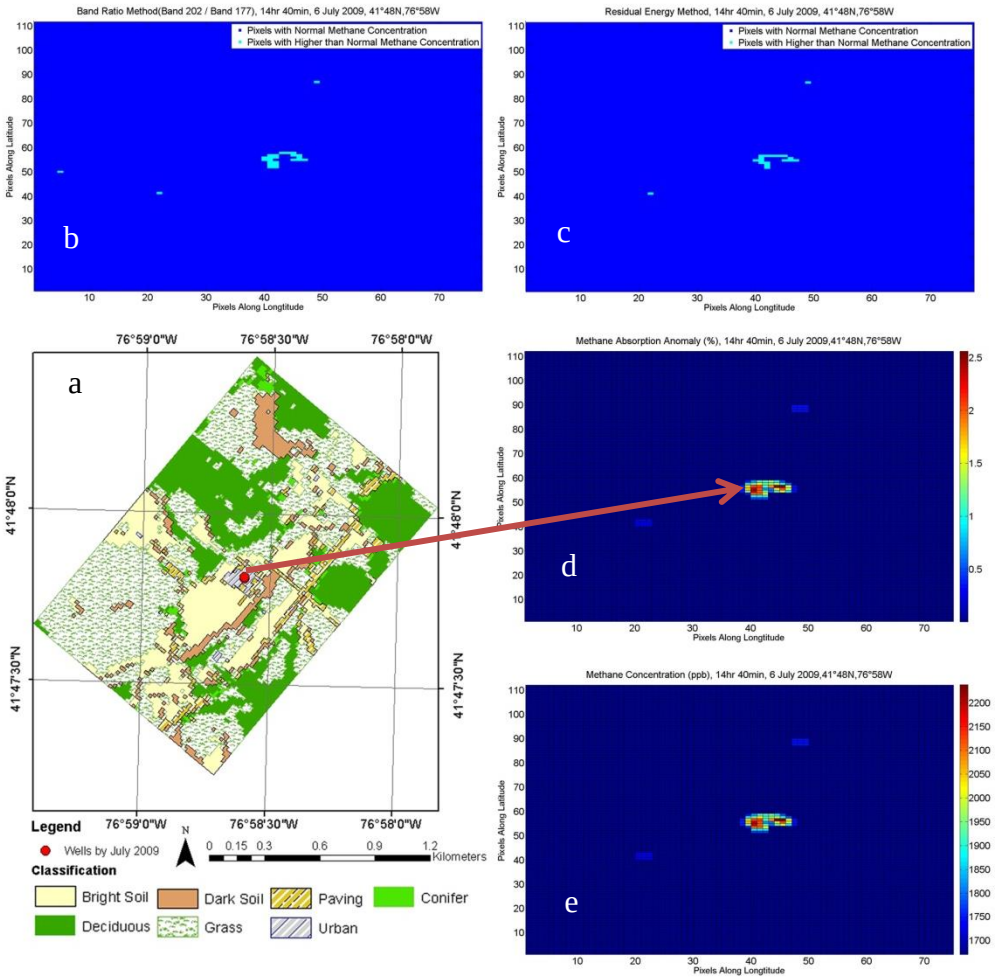

Figure 23- Mapping and evaluation of ROI_PA_A, the (a) map shows land cover classes in ROI_PA_A, the (b) shows mapped methane emission pixels by band ratio technique, the (c) shows mapped methane emission pixels by residual energy technique, the (d) shows methane absorption anomaly, and (e) shows atmospheric methane concentration

In Fig. 24, the results of mapping and evaluation over ROI_PA_B are presented. As it is shown in Fig. 24c, the results of mapping are pointing to the same pixels as band ratio technique indicates (Fig. 24b). As it is shown in Fig. 24c, the mapped pixels of possible methane emission are not from the shale gas well pad areas but from surroundings. After mapping possible pixels of methane emission in ROI_PA_B, absorption by methane plume was calculated (Fig. 24d). Later atmospheric methane concentrations were estimated (Fig. 24d). Finally, same as other ROIs, the methane concentration per square meter was calculated over mapped pixels and reported in Table 17.

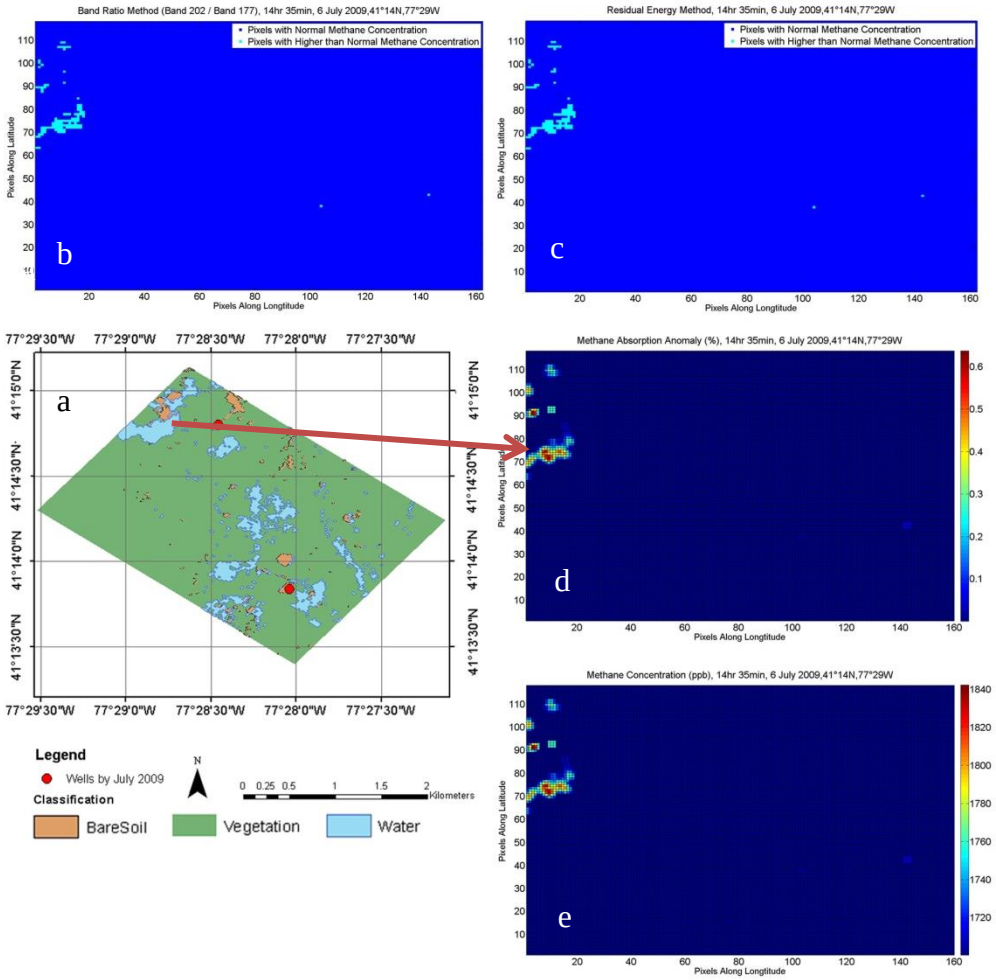

Figure 24- Mapping and evaluation of ROI_PA_B, the (a) map shows land cover classes in ROI_PA_B, the (b) shows mapped methane emission pixels by band ratio technique, the (c) shows mapped methane emission pixels by residual energy technique, the (d) shows methane absorption anomaly, and (e) shows atmospheric methane concentration

In order to calculate the fugitive methane emission in ROI_PA_A and ROI_PA_B, first methane density at mapped pixels were calculate using Fig. 22, Fig. 23 and Fig. 24 along with spatial resolution of imagery provided in Table 5, Table 7, and Table 8. The results of methane density calculation are provided in Table 17.

Table 17- Atmospheric methane concentration per unit of area

ROI	Reference Point (ROI_CA)	ROI_PA_A	ROI_PA_B
Methane density (ppb/m^2)	32.395	0.594	0.202

3.2.1 Methane Flux Evaluation

In this study ROI_CA was considered as reference point where the methane emission from natural seep was reported unti1998 (Fig. 25). The AVIRIS flight over the reference point was

in June 2008, but there was not any other study on methane flux over the ROI in 2008, so minimum and maximum values in Fig. 25 was used as possible flux values in ROI_CA in order to estimate flux in ROI_PA_A and ROI_PA_B (Diagram 14).

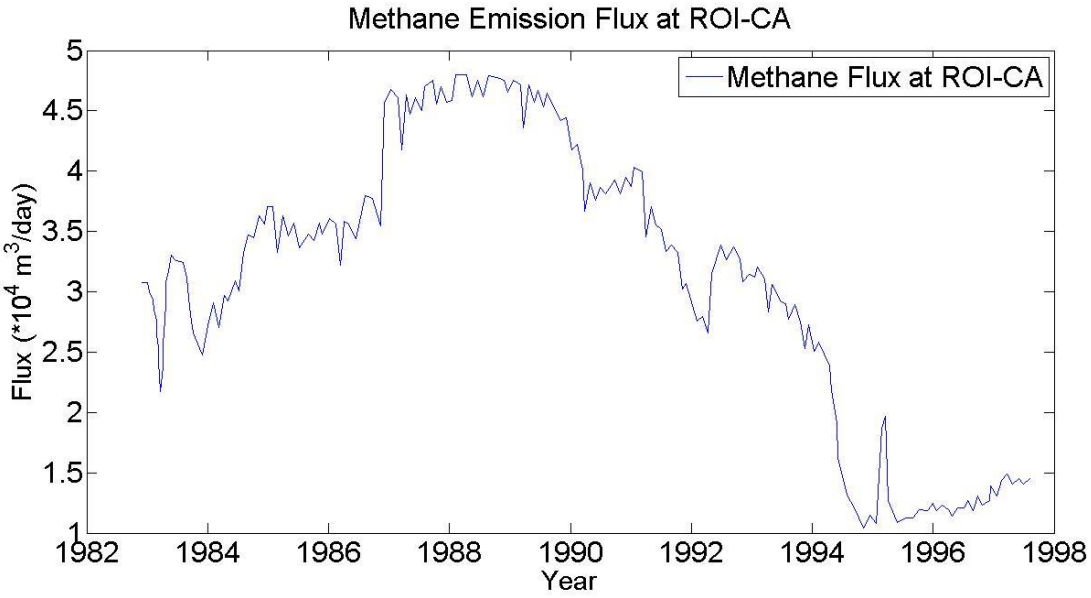

Figure 25-Methane flux at ROI_CA redrawn from Quigtey et al. (1999, p. 1050)

The mean value of natural gas production in Marcellus shale basin, PA, USA in July 2009 when there was AVIRIS flight over ROIs in Pennsylvania was retrieved from U.S. EIA (Table 18). However, the natural production flux per each well was not available, so the production flux in July 2009 was used as minimum and production flux in May 2015 as maximum in order to calculate the fugitive flux emission using Eq. 12.

Table 18- Natural gas production per well per day in Marcellus (U.S. EIA, 2015a)

Date	Natural Gas (Mcf/d) Production per Rig in Marcellus Shale Basin
Jul-09	971
May-15	8,176

The centrepiece results of methane mapping and evaluation part of this study are shown in Fig. 26 and Fig. 27. The fugitive methane emission was calculated using Eq. 12, Table 17, Fig. 25 and Table 18.

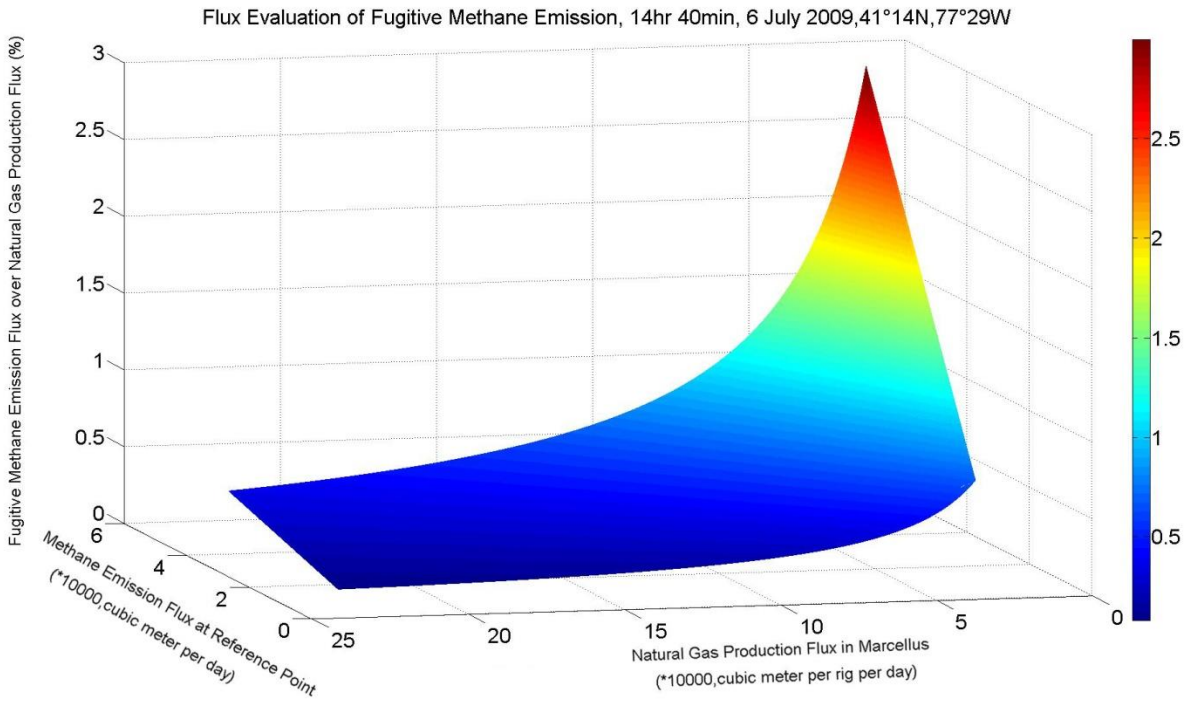

Figure 26- Fugitive methane emission flux evaluation in ROI_PA_A

In Fig. 27, the possible fugitive methane emission from natural gas production in ROI_PA_B is shown. However, it is not clear that whether the mapped pixels (Fig. 24) are showing possible methane emissions from shale gas exploitation or it is natural methane emission.

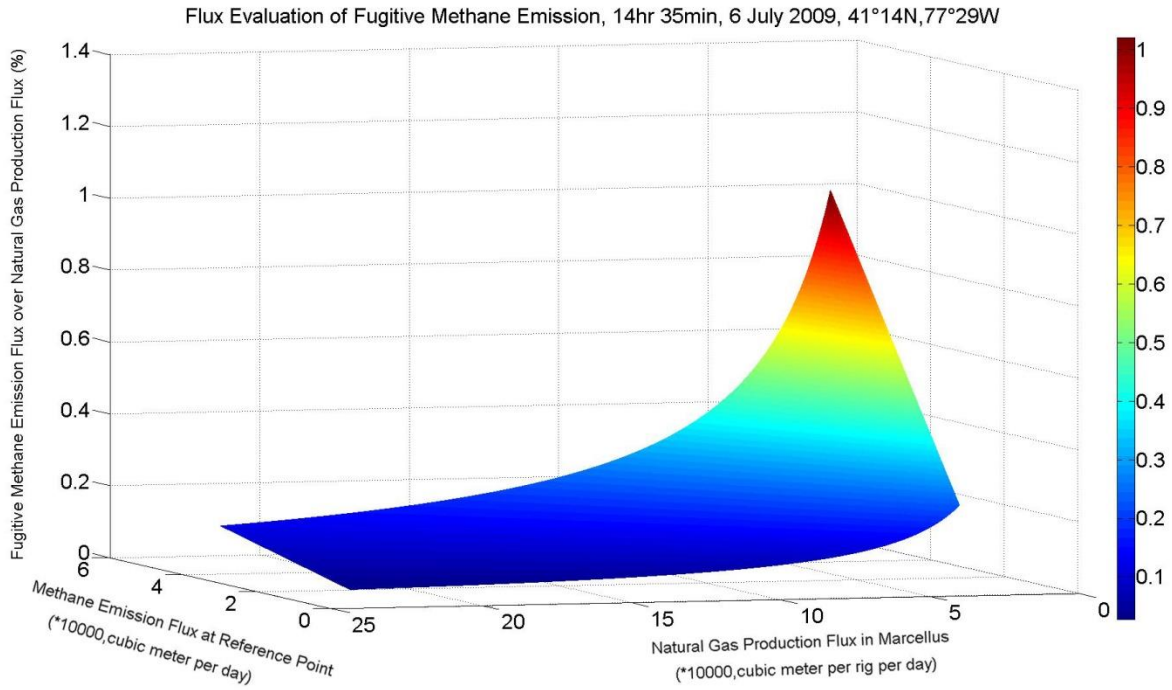

Figure 27- Methane emission flux evaluation in ROI_PA_B

In this study the reference point was ROI_CA, in which there is known methane seep, but the methane emission flux at reference point in June 2008 is not clear, so the only data was used

as it is shown in Fig. 25. The minimum and maximum fugitive methane emission from wellhead during shale gas production is considered by the maximum and minimum methane flux at reference point (ROI_CA), with assumption that the shale gas production in ROI_PA_A was 971 Mcf/d per rig as mentioned in Table 18. In this study, in ROI_PA_A during the AVIRIS flight there were two wells, which are not enough. In Table 19, the flux evaluation of fugitive methane emission at ROI_PA_A by this study is compared with other studies.

Table 19- Fugitive methane emission evaluation

	Fugitive emission from natural gas production at wellhead						
Research	Other studies.					This study ROI_PA_A	
	(Howarth, Santoro and Ingraffea, 2011)		(Hausfather and Muller, 2014)		(Karion et al., 2013)		
Fugitive emission (%)	Min	Max	Min	Max	Mean	Min	Max
	0.3	1.9	1.7	2.8	2.5	0.67	3

The results of this thesis might be considered in acceptable range, but still more wells should be taken into consideration. Although, maximum value reported by the thesis is higher than other studies, based on decline in methane emission at ROI_CA (Quigtey et al., 1999), it is more plausible that real value of fugitive methane emission is close to the minimum value reported by the thesis in Table 19.

Although, when the thesis author started the work there was no study over Marcellus shale basin using remote sensing, Peischl et al. (2015, p.2119) reported fugitive methane emission of 1.0–2.1% from the Haynesville region during production operations, 1.0–2.8% from the Fayetteville region, and 0.18–0.41% from the Marcellus region in northeastern Pennsylvania, USA. Peischl et al. (2015, p. 2138) state that “climate impact of using natural gas as a fuel in power plants would be less than that of coal’’.

4 Conclusions and Future Works

In this chapter the conclusions based on the thesis study and future works are presented.

4.1 Conclusions

This thesis work was separated into two parts, climate simulations and fugitive methane emissions mapping and evaluation. Based on the climate simulations part, it is possible to slow down global warming by switching to the "golden age of natural gas" as it is also reported by IEA (2012), so policy makers can trust on this age. Based on the climate simulations, if the policy makers move on supplying global energy demand mainly by natural gas combustion in the next decades, we can keep the 2°C policy until the end of 21st century, and there would then be less cost for adaptation to climate change. In the fugitive methane emission mapping and evaluation part of this study, fugitive methane emissions from wellheads over the shale gas drilling areas using remote sensing imagery were mapped and the flux of the emissions for each pixels was estimated. The fugitive emissions from shale gas production wellheads may be considered in normal range of fugitive methane emissions compared to the conventional natural gas production wellheads. In this study, for mapping methane plumes a new easy and straight-forward mapping technique (residual energy technique) was introduced which is capable to detect methane plumes both in homogenous and heterogeneous areas.

4.2 Future Works

Studying the climate change at global scale is complicated. Thus many input driving forces should be taken into consideration. It is recommended to improve this study by considering more greenhouse gases as driving forces for climate simulations. The global CO_2 sink played an important role in this study, so it is necessary to know what the capacity of the planet Earth is to uptake anthropogenic CO_2.

It was mentioned by Quigtey et al., (1999, p. 1050) that oil and gas production may lead to reduce the natural methane emission at global scale. Maybe increasing oil and gas extraction in the past decades resulted in a decrease in CH_4 emission increase (Fig. 28 in Appendix A). So, it is important to know how combusting hydrocarbons and converting CH_4 to CO_2 helps to not only secure energy demand but also take climate issues at global scale into account.

Kvenvolden and Cooper (2003, p. 140) expresses that "recent global estimates of crude-oil seepage rates suggest that about 47% of crude oil currently entering the marine environment is from natural seeps." Leifer, Kamerling, Luyendyk and Wilson (2010, p. 331) states that ''In general, the relationship between terrestrial gas seepage, migration pathways, and hydrocarbon reservoirs is difficult to assess.'' The new technique of methane emissions mapping presented in this work may be used not only for evaluating methane emission from natural and human activities, but can also play a role along with geological studies for exploring new hydrocarbon resources.

In one of regions of interest in Pennsylvania, there was a possible methane emission from surrounding areas. As it is shown in Fig. 24, the pixels of possible emissions are pointing somewhere outside of shale gas well pads. It is not certain what the source of the emission

was. It might be a result disposing or storing returned formation water on surface without proper filtering. It might be a result of natural CH_4 emission, or might be result of fracking. So site sampling and isotope analysis are required. However, the number of gas wells in this study certainly is not enough to extend the results to the whole shale gas activities, even to the shale gas activities throughout the Marcellus shale basin in Pennsylvania. So, more research should be done to study flux of fugitive methane emissions

In order to detect trace gases for monitoring human or natural activities, the presented residual energy technique may be helpful, but more studies are recommended to effective wavelength bands for trace gas detection.

5 References

Alvarez, R. a., Pacala, S.W., Winebrake, J.J., Chameides, W.L. and Hamburg, S.P., 2012. Greater focus needed on methane leakage from natural gas infrastructure. *Proceedings of the National Academy of Sciences*, 109(17), pp.6435–6440.

Anon, 2012. *American Geophysical Union*. [online] Wiley. Available at: <http://onlinelibrary.wiley.com/doi/10.1029/2012EO500006/pdf>. [Accessed 16 Jan. 2015].

ArcGIS, 2012a. *Basic Information of States*. [online] Available at: <http://www.arcgis.com/home/item.html?id=f7f805eb65eb4ab787a0a3e1116ca7e5> [Accessed 1 Jan. 2015].

ArcGIS, 2012b. *Boundary of Pennsylvania Counties*. [online] Available at: <http://www.arcgis.com/home/item.html?id=04e3f70b4b7f401faafd431da9355ab4> [Accessed 1 Jan. 2015].

ASTER/NASA, 2015. *Reflectance Spectrum*. [online] Available at: <http://speclib.jpl.nasa.gov/documents> [Accessed 10 Mar. 2015].

BP, 2014. *BP Energy Outlook 2035*. [online] Available at: <http://www.bp.com/content/dam/bp/pdf/Energy-economics/Energy-Outlook/Energy_Outlook_2035_booklet.pdf>.[Accessed 10 Mar. 2015].

Bradbury, J. and Obeiter, M., 2013. *A Close Look at Fugitive Methane Emissions from Natural Gas*. [online] Available at: <http://www.wri.org/blog/2013/04/close-look-fugitive-methane-emissions-natural-gas> [Accessed 15 May 2015].

Bradley, E.S., Leifer, I., Roberts, D. a., Dennison, P.E. and Washburn, L., 2011. Detection of marine methane emissions with AVIRIS band ratios. *Geophysical Research Letters*, [online] 38(10), pp.3–6. Available at: <http://onlinelibrary.wiley.com/doi/10.1029/2011GL046729/abstract>. [Accessed 11 Feb. 2015].

Buckle, S. and Mactavish, F., 2013. *The slowdown in global mean surface temperature rise*. [online] London. Available at: <https://www.imperial.ac.uk/media/imperial-college/grantham-institute/public/publications/grantham-notes/The-slowdown-in-global-mean-surface-temperature-rise---Grantham-Note-1.pdf>.[Accessed 14 Jan. 2015].

De Castro, C., Carpintero, Ó., Frechoso, F., Mediavilla, M. and de Miguel, L.J., 2013. A top-down Approach to Assess Physical and Ecological Limits of Biofuels. *Energy*, [online] 64, pp.506–512. Available at: <http://dx.doi.org/10.1016/j.energy.2013.10.049>. [Accessed 1 May 2015].

Chandler, M. a., Richards, S.J. and Shopsin, M.J., 2005. EdGCM: Enhancing climate science education through climate modeling research projects. *In Proceedings of the 85th Annual Meeting of the American Meteorological Society, 14th Symposium on Education*. [online] Available at: <http://edgcm.columbia.edu/support2/faq/>.[Accessed 21 Feb. 2015].

Chandler, M.A., 2015. *EdGCM*. [online] Available at: <http://www.giss.nasa.gov/staff/mchandler.html> [Accessed 1 May 2015].

Cheng, K.S., Su, Y.F., Yeh, H.C., Chang, J.H. and Hung, W.C., 2012. A path radiance estimation algorithm using reflectance measurements in radiometric control areas. *International Journal of Remote Sensing*, 33(5), pp.1543–1566.

Ciais, P., Sabine, C., Bala, G., Bopp, L., Brovkin, V., Canadell, J., Chhabra, A., DeFries, R., Galloway, J., Heimann, M., Jones, C., Quéré, C. Le, Myneni, R.B., Piao, S. and Thornton, P., 2013. *Carbon and Other Biogeochemical Cycles. In: Climate Change 2013: The Physical Science Basis. Contribution of Working Group I to the Fifth Assessment Report of the Intergovernmental Panel on Climate Change [Stocker, T.F., D. Qin, G.-K. Plattner, M. Tignor,*. [online] *Cambridge University Press, Cambridge, United Kingdom and New York, NY, USA.* Available at: <http://www.ipcc.ch/report/ar5/wg1/docs/review/WG1AR5_SOD_Ch06_All_Final.pdf>. [Accessed 8 Jan. 2015].

Columbia Univeristy and NASA, 2012. *EVA. (1.6.6)*. Available at: <http://edgcm.columbia.edu/download-edgcm/> [Accessed 28 Jan. 2015].

Columbia University and NASA, 2013. *EdGCM. (4.0 beta)*. Available at: <http://edgcm.columbia.edu/download-edgcm/> [Accessed 28 Jan. 2015].

Critchlow, A., 2015. Current CO2 Emission is Unsustainable. [online] Available at: <http://www.telegraph.co.uk/finance/newsbysector/energy/11417968/BP-says-CO2-emissions-unsustainable-warns-on-global-warming.html>.[Accessed 15 Feb. 2015].

Crouch, J.R., Shen, Y., Austin, J. a. and Dinniman, M.S., 2008. An Educational Interactive Numerical Model of the Chesapeake Bay. *Computers and Geosciences*, [online] 34(3), pp.247–258. Available at: <http://www.sciencedirect.com/science/article/pii/S0098300407001501>. [Accessed 8 Feb. 2015].

Darbee, P. a and Field, C.B., 2010. *Climate Change for Policymakers and Business Leaders*. [online] *Chief Executive*. Available at: <http://energyseminar.stanford.edu/sites/all/files/eventimage/PGE climange change for policymakers and business leaders.pdf>.[Accessed 23 Feb. 2015].

Directorate-General for Climate Action, 2010. *EU action on climate*. [online] Available at: <http://ec.europa.eu/clima/consultations/docs/0005/background_info_en.pdf> [Accessed 29 Feb. 2015].

EEA, 2013a. *Atmospheric Concentration of Carbon Dioxide (ppm)*. [online] Available at: <http://www.eea.europa.eu/data-and-maps/figures/atmospheric-concentration-of-co2-ppm-1> [Accessed 5 Jan. 2015].

EEA, 2013b. *Atmospheric Concentration of Methane (ppb)*. [online] Available at: <http://www.eea.europa.eu/data-and-maps/figures/atmospheric-concentration-of-ch4-ppb-1> [Accessed 5 Jan. 2015].

EEA, 2013c. *Atmospheric Concentration of Nitrous Oxide (ppb)*. [online] Available at: <http://www.eea.europa.eu/data-and-maps/figures/atmospheric-concentration-of-n2o-ppb-1> [Accessed 5 Jan. 2015].

ESRI, 2013. *ArcMap version 10.2.2*. Redlands, California, USA: Environmental Systems Research Institute. Available at: https://desktop.arcgis.com/en/desktop/

ESRL/NOAA, 2015. *At-surface Irradiation Energy*. [online] Available at: <http://www.esrl.noaa.gov/gmd/grad/surfrad/> [Accessed 15 Mar. 2015].

Evangelinos, C., Lermusiaux, P.F.J., Geiger, S.K., Chang, R.C. and Patrikalakis, N.M., 2006. Web-enabled Configuration and Control of Legacy codes: An Application to Oocean Modeling. *Ocean Modelling*, [online] 13(3-4), pp.197–220. Available at: <http://www.sciencedirect.com/science/article/pii/S1463500305000806#>. [Accessed 3 Jan. 2015].

EXELIS, 2013. *ENVI version 5.1*. Boulder, Colorado, USA: Exelis Visual Information Solutions. Available at: http://www.exelisvis.com/ProductsServices/ENVIProducts/ENVI.aspx

Fekete, 2014. *Reservoir Fluid Types*. [online] Available at: <http://www.fekete.com/SAN/WebHelp/FeketeHarmony/Harmony_WebHelp/Content/HTML_Files/Reference_Material/General_Concepts/Reservoir_Fluid_Types.htm> [Accessed 2 May 2015].

Forster, P., Ramaswamy, V., Artaxo, P., Berntsen, T., Betts, R., Fahey, D.W., Haywood, J., Lean, J., Lowe, D.C., Myhre, G., Nganga, J., Prinn, R., Raga, G., And, M.S. and Dorland, R. Van, 2007. Changes in Atmospheric Constituents and in Radiative Forcing. *Change*, [online] 30(22), pp.129–234. Available at: <http://en.scientificcommons.org/23467316>. [Accessed 1 Jan. 2015].

GISS/NASA, 2015. *Global land-Ocean Temperature Index in 0.01 degrees Celsius, Base Period: 1951-1980*. [online] Available at: <http://data.giss.nasa.gov/gistemp/tabledata_v3/GLB.Ts+dSST.txt> [Accessed 31 Jan. 2015].

Google, 2013. *Google Earth (7.1.2.2041)*. Available at: <https://www.google.com/earth/> [Accessed 24 Nov. 2014].

GSFC/NASA, 2014. *Atmospheric Correction Parameter Calculator*. [online] Available at: <http://atmcorr.gsfc.nasa.gov/> [Accessed 15 Mar. 2015].

Halliburton, 2011. *EBN Final Report*. [online] Available at: <https://www.ebn.nl/wp-content/uploads/2014/11/Volledige-rapporten_2011_NFDP_Halliburton.pdf>.[Accessed 14 Oct. 2014].

Harvard-Smithsonian Center for Astrophysics (CFA), Cambridge, MA, U. and V.E. Zuev Insitute of Atmosperic Optics (IAO), Tomsk, R., 2015. *HITRAN on the Web*. [online] Available at: <http://hitran.iao.ru/> [Accessed 22 Feb. 2015].

Hausfather, Z. and Muller, R., 2014. *New EPA Report Reveals Significantly Lower Methane Leakage from Natural Gas*. [online] Berkeley. Available at: <http://static.berkeleyearth.org/memos/epa-report-reveals-lower-methane-leakage-from-natural-gas.pdf>. [Accessed 22 Feb. 2015].

Howarth, R.W., 2014. A Bridge to Nowhere: Methane Emissions and the Greenhouse Gas Footprint of Natural Gas. *Energy Science & Engineering*, [online] 2(2), pp.47–60. Available at: <http://doi.wiley.com/10.1002/ese3.35> [Accessed 9 Dec. 2014].

Howarth, R.W., Santoro, R. and Ingraffea, A., 2011. Methane and the Greenhouse-Gas Footprint of Natural Gas from Shale Formations. *Climatic Change*, [online] 106(4), pp.679–690. Available at: <http://www.acsf.cornell.edu/Assets/ACSF/docs/attachments/Howarth-EtAl-2011.pdf>. [Accessed 14 Feb. 2015].

Huning, L.S. and Margulis, S. a., 2015. Watershed Modeling Applications with a Modular Physically-based and Spatially-Distributed Watershed Educational Toolbox. *Environmental Modelling & Software*, [online] 68, pp.55–69. Available at: <http://linkinghub.elsevier.com/retrieve/pii/S1364815215000572>. [Accessed 5 June 2015].

IEA, 2012. Golden Rules for a Golden Age of Gas. *World Energy Outlook Special Report*, [online] p.150. Available at: <http://www.worldenergyoutlook.org/media/weowebsite/2012/goldenrules/weo2012_goldenrulesreport.pdf>. [Accessed 11 Feb. 2015].

IEA, 2014. *World Energy Outlook, Executive Summary*. [online] International Energy Agency. Available at: <http://www.iea.org/Textbase/npsum/WEO2013SUM.pdf>. [Accessed 13 Feb. 2015].

IEA, 2015. *World Energy outlook*. [online] Available at: <http://www.iea.org/publications/scenariosandprojections/> [Accessed 15 May 2015].

IPCC, 1990a. *IPCC First Assessment Report (FAR)*. [online] Available at: <https://www.ipcc.ch/publications_and_data/publications_ipcc_first_assessment_1990_wg1.shtml>. [Accessed 7 Jan. 2015].

IPCC, 1990b. *Radiative Forcing*. [online] Available at: <https://www.ipcc.ch/ipccreports/far/wg_I/ipcc_far_wg_I_chapter_02.pdf>. [Accessed 8 Jan. 2015].

IPCC, 2007a. *Climate Change 2007 Synthesis Report [Core Writing Team, Pachauri, R.K and Reisinger, A. (eds.)]*. [online] *IPCC, Geneva, Switzerland, 104 pp.* Available at: <http://www.ipcc.ch/pdf/assessment-report/ar4/syr/ar4_syr_full_report.pdf>. [Accessed 6 Jan. 2015].

IPCC, 2007b. *Summary for Policymakers. In: Climate Change 2007: The Physical Science Basis. Contribution of Working Group I to the Fourth Assessment Report of the Intergovernmental Panel on Climate Change [Solomon, S., D. Qin, M. Manning, Z. Chen, M. Marquis, K.B. Ave*. [online] *Cambridge University Press, Cambridge, United Kingdom and New York, NY, USA.* Available at:

<http://www.ipcc.ch/publications_and_data/ar4/wg1/en/ch5s5-es.html>. [Accessed 6 Jan. 2015].

IPCC, 2014a. *Climate Change 2014 Synthesis Report Summary Chapter for Policymakers*. [online] *IPCC*. Available at: <http://ipcc.ch/pdf/assessment-report/ar5/syr/AR5_SYR_FINAL_SPM.pdf>. [Accessed 4 Jan. 2015].

IPCC, 2014b. *Climate Observations*. [online] Available at: <http://www.ipcc-data.org/observ/clim/index.html> [Accessed 10 Jan. 2015].

IPCC, 2015. *IPCC Organization*. [online] IPCC. Available at: <http://www.ipcc.ch/organization/organization.shtml> [Accessed 15 Sep. 2014].

Jackson, R.B.R., Down, A., Phillips, N.G., Ackley, R.C., Cook, C.W., Plata, D.L. and Zhao, K., 2014. Natural gas pipeline leaks across Washington, DC. *Environmental science & technology*, 48(3), pp.2051–8.

JPL, 2015. *Home*. [online] Available at: <http://aviris.jpl.nasa.gov/aviris/index.html> [Accessed 3 May 2015].

JPL/NASA, 2015. *2006-Present AVIRIS flight Locator Tool*. [online] Available at: <http://aviris.jpl.nasa.gov/alt_locator/> [Accessed 1 Feb. 2015].

Karion, A., Sweeney, C., Pétron, G., Frost, G., Michael Hardesty, R., Kofler, J., Miller, B.R., Newberger, T., Wolter, S., Banta, R., Brewer, A., Dlugokencky, E., Lang, P., Montzka, S. a., Schnell, R., Tans, P., Trainer, M., Zamora, R. and Conley, S., 2013. Methane Emissions Estimate from Airborne Measurements over a Western United States Natural Gas Field. *Geophysical Research Letters*, [online] 40(16), pp.4393–4397. Available at: <http://onlinelibrary.wiley.com/doi/10.1002/grl.50811/abstract>. [Accessed 2 Feb. 2015].

Kelly, S., 2015. *Methane Emission in Marcellus Shale -Basin, PA, USA*. [online] Available at: <http://www.desmogblog.com/2014/04/16/study-find-marcellus-drilling-methane-leaks-1-000-times-epa-estimates-casting-doubt-bridge-fuel-notion> [Accessed 10 Feb. 2015].

Kvenvolden, K. a. and Cooper, C.K., 2003. Natural Seepage of Crude Oil into the Marine Environment. *Geo-Marine Letters*, [online] 23(3-4), pp.140–146. Available at: <https://walrus.wr.usgs.gov/reports/reprints/Kvenvolden_GML_23.pdf>. [Accessed 28 Jan. 2015].

Lanckriet, S., Araya, T., Cornelis, W., Verfaillie, E., Poesen, J., Govaerts, B., Bauer, H., Deckers, J., Haile, M. and Nyssen, J., 2012. Impact of Conservation Agriculture on Catchment Runoff and Soil Loss under Changing Climate Conditions in May Zeg-zeg (Ethiopia). *Journal of Hydrology*, [online] 475, pp.336–349. Available at: <http://dx.doi.org/10.1016/j.jhydrol.2012.10.011>. [Accessed 18 Feb. 2015].

Leifer, I., Kamerling, M.J., Luyendyk, B.P. and Wilson, D.S., 2010. Geologic Control of Natural Marine Hydrocarbon Seep Emissions, Coal Oil Point Seep Field, California. *Geo-Marine Letters*, [online] 30(3-4), pp.331–338. Available at: <http://www.geol.ucsb.edu/faculty/luyendyk/Luyendyk_pdf/Leifer et al Geo-Mar Lett %2710.pdf>. [Accessed 17 Jan. 2015].

Leifer, I., Roberts, D., Margolis, J. and Kinnaman, F., 2006. In situ sensing of methane emissions from natural marine hydrocarbon seeps: A potential remote sensing technology. *Earth and Planetary Science Letters*, [online] 245(3-4), pp.509–522. Available at: <http://www.sciencedirect.com/science/article/pii/S0012821X06000823>. [Accessed 23 Jan. 2015].

Lieskovsky, J., Yan, R. and Gorgen, S., 2014. *Marcellus Region Production Continues Growth*. [online] Available at: <http://www.eia.gov/todayinenergy/detail.cfm?id=17411> [Accessed 1 May 2015].

Marcellus center for outreach and research/Penn State University, 2009. *Marcellus Maps and Graphics*. [online] Available at: <http://www.marcellus.psu.edu/resources/maps.php> [Accessed 15 Feb. 2015].

Murray, J. and King, D., 2012. Oil's tipping point has passed. *Nature*, 481(January), pp.433–435. [online] Available at: <http://www.nature.com/nature/journal/v481/n7382/full/481433a.html>. [Accessed 20 Dec. 2014].

Myhre, G., Shindell, D., Bréon, F.-M., Collins, W., Fuglestvedt, J., Huang, J., Koch, D., Lamarque, J.-F., Lee, D., Mendoza, B., Nakajima, T., Robock, A., Stephens, G., Takemura, T. and Zhan, H., 2013. *Anthropogenic and natural radiative forcing*. [online] *Climate Change 2013: The Physical Science Basis. Contribution of Working Group I to the Fifth Assessment Report of the Intergovernmental Panel on Climate Change*. Available at: <https://www.ipcc.ch/pdf/assessment-report/ar5/wg1/WG1AR5_Chapter08_FINAL.pdf>. [Accessed 7 Jan. 2015].

Nakicenovic, N., Alcamo, J., Davis, G., Vries, B. de, Fenhann, J., Gaffin, S., Gregory, K., Griibler, A., Jung, T.Y., Kram, T., Rovere, E.L. La, Michaelis, L., Mori, S., Morita, T., Pepper, W., Pitcher, H., Lynn Price, Keywan Riahi, A.R., Rogner, H.-H., Sankovski, A., Schlesinger, M., Shukla, P., Smith, S., Swart, R., Rooijen, S. van, Victor, N. and Dadi, Z., 2000. *Special Report on Emissions Scenarios*. [online] *... Report on Emissions Scenarios*. Available at: <http://www.ipcc.ch/ipccreports/sres/emission/emissions_scenarios.pdf>. [Accessed 4 Feb. 2015].

Ndehedehe, C., Ekpa, A., Simeon, O. and Nse, O., 2013. Understanding the Neural Network Technique for Classification of Remote Sensing Data Sets. *New York Science Journal*, 6(8), pp.26–33.

NOAA, 2007. *How do Human Activities Contribute to Climate Change and How do They Compare with Natural Influences?* [online] Available at: <http://oceanservice.noaa.gov/education/pd/climate/factsheets/howhuman.pdf>. [Accessed 15 Feb. 2015].

NOAA, 2012. *Global CO2 Sink*. [online] Available at: <http://www.noaanews.noaa.gov/stories2012/20120801_esrlcarbonstudy.html> [Accessed 15 Jan. 2015].

Peischl, J., Ryerson, T.B., Aikin, K.C., Gouw, J. a, Gilman, J.B., Holloway, J.S., Lerner, B.M., Nadkarni, R., Neuman, J. a, Nowak, J.B., Trainer, M., Warneke, C. and Parrish, D.D.,

2015. Quantifying Atmospheric Methane Emissions from the Haynesville, Fayetteville, and northeastern Marcellus shale gas production regions. *Geophysical Research: Atmospheres*. [online] Available at: <http://onlinelibrary.wiley.com/doi/10.1002/2014JD022697/abstract>. [Accessed 10 May. 2015].

PV Lighthouse, 2015. *Solar Spectrum*. [online] Available at: <http://www.pvlighthouse.com.au/calculators/solar spectrum calculator/solar spectrum calculator.aspx> [Accessed 15 Mar. 2015].

Qin, D., Manning, M., Chen, Z., Marquis, M., Averyt, K.B. and Kingdom, U., 2007. *FAQ-From the Report Accepted by Working Group I of the Intergovernmental Panel on Climate Change*. [online] *IPCC, 2007: Climate Change 2007: The Physical Science Basis. Contribution of Working Group I to the Fourth Assessment Report of the Intergovernmental Panel on Climate Change*. Available at: <http://www.ipcc.ch/pdf/assessment-report/ar4/wg1/ar4-wg1-faqs.pdf>.

Quigtey, D.C., Homafius, J.S., Luyendyk, B.P., Francis, R.D., Clark, J. and Washburn, L., 1999. Decrease in Natural Marine Hydrocarbon Seepage Near Coal Oil Point, California, Associated with Offshore Oil Production. *Geology*, [online] 27(11), pp.1047–1050. Available at: <http://seeps.geol.ucsb.edu/articles/1999 Quigley et al Geology.pdf>.

Raupach, M.R., Gloor, M., Sarmiento, J.L., Canadell, J.G., Frölicher, T.L., Gasser, T., Houghton, R. a., Le Quéré, C. and Trudinger, C.M., 2014. The declining uptake rate of atmospheric CO2 by land and ocean sinks. *Biogeosciences*, 11(13), pp.3453–3475.

Roberts, D. a., Bradley, E.S., Cheung, R., Leifer, I., Dennison, P.E. and Margolis, J.S., 2010. Mapping methane emissions from a marine geological seep source using imaging spectrometry. *Remote Sensing of Environment*, [online] 114(3), pp.592–606. Available at: <http://dx.doi.org/10.1016/j.rse.2009.10.015>. [Accessed 1 Feb. 2015].

Rothman, L.S., Gamache, R.R., Goldman, A., Brown, L.R., Toth, R.A., Pickett, H.M., Poynter, R.L., J.-M.Flaud, Camy-Peyret, C., Barbe, A., Husson, N., Rinsland, C.P. and Smith, M.A.H., 1986. The HITRAN database : 1986 edition. [online] Available at: <https://www.osapublishing.org/view_article.cfm?gotourl=https://www.osapublishing.org/DirectPDFAccess/3049C1A2-BEDF-C2B6-358B93D803AD7036_30734/ao-26-19-4058.pdf?da=1&id=30734&seq=0&mobile=no&org=>. [Accessed 17 Jan. 2015].

Ruamsuke, K., Dhakal, S. and Marpaung, C.O.P., 2015. Energy and economic impacts of the global climate change policy on Southeast Asian countries: A general equilibrium analysis. *Energy*, 81, pp.446–461.

Schlatter, T.W., 2009. Atmospheric Composition and Vertical Structure. [online] 6, pp.1–54. Available at: <http://ruc.noaa.gov/AMB_Publications_bj/2009 Schlatter_Atmospheric Composition and Vertical Structure_eae319MS-1.pdf>. [Accessed 10 Jan. 2015].

Shaftel, H., 2015. *Global Climate Change*. [online] Available at: <http://climate.nasa.gov/400ppmquotes/> [Accessed 15 May 2015].

Sorrell, S., Speirs, J., Bentley, R., Brandt, A. and Miller, R., 2009. *Global Oil Depletion: An Assessment of the Evidence for a Near-term Peak in Global Oil Production*. [online] *Energy*

Policy, Available at: <http://linkinghub.elsevier.com/retrieve/pii/S0301421510003204>. [Accessed 15 Dec. 2014].

Subramanian, S., Gat, N., Sheffield, M., Barhen, J. and Toomarian, N., 1997. Methodology for hyperspectral image classification using novel neural network. *Algorithms for Multispectral and Hyperspectral Imagery III*, [online] 3071(April), pp.1–10. Available at: <http://www.techexpo.com/WWW/opto-knowledge/NNET.pdf>. [Accessed 15 Jan. 2015].

The MathWorks Inc., 2012. *MATLAB. version 2012a*. Natick, Massachusetts, USA. Available at: <http://se.mathworks.com/support/compilers/R2012a/win64.html> [Accessed 1 Sep. 2013].

The Optical Remote Sensing Laboratory of The City College of New York, 2012. *Dewpoint & mixing ratio calculator*. [online] Available at: <http://nycmetnet.ccny.cuny.edu/index.php> [Accessed 20 Feb. 2015].

Thorpe, a K., Roberts, D. a, Dennison, P.E., Bradley, E.S. and Funk, C.C., 2012. Point source emissions mapping using the Airborne Visible/Infrared Imaging Spectrometer (AVIRIS). *SPIE Proceedings-Algorithms and Technologies for Multispectral, Hyperspectral, and Ultraspectral Imagery XVIII*, [online] 8390, pp.839013–1/9. Available at: <http://www.geog.ucsb.edu/~akthorpe/documents/Andrew_K_Thorpe_2012_SPIE.pdf>. [Accessed 1 Jan. 2015].

Thorpe, a. K., Frankenberg, C. and Roberts, D. a., 2014. Retrieval techniques for airborne imaging of methane concentrations using high spatial and moderate spectral resolution: Application to AVIRIS. *Atmospheric Measurement Techniques*, [online] 7(2), pp.491–506. Available at: <http://www.atmos-meas-tech.net/7/491/2014/amt-7-491-2014.html>. [Accessed 5 Jan. 2015].

Thorpe, A.K., Roberts, D. a., Bradley, E.S., Funk, C.C., Dennison, P.E. and Leifer, I., 2013. High resolution mapping of methane emissions from marine and terrestrial sources using a Cluster-Tuned Matched Filter technique and imaging spectrometry. *Remote Sensing of Environment*, 134, pp.305–318. [online] Available at: <http://dx.doi.org/10.1016/j.rse.2013.03.018>. [Accessed 1 Jan. 2015].

U.S. EIA, 2013. *World Energy Consumption Outlook*. [online] Available at: <http://www.eia.gov/todayinenergy/detail.cfm?id=12251> [Accessed 15 May 2015].

U.S. EIA, 2015a. *Drilling Productivity Report*. [online] Available at: <http://www.eia.gov/petroleum/drilling/> [Accessed 5 May 2015].

U.S. EIA, 2015b. *Gross Natural Gas Production (Billion Cubic Feet)*. [online] Available at: <http://www.eia.gov/cfapps/ipdbproject/iedindex3.cfm?tid=3&pid=3&aid=1&cid=US,&syid=1990&eyid=2012&unit=BCF> [Accessed 2 Jan. 2015].

U.S. EIA, 2015c. *Maps: Exploration, Resources, Reserves, and Production*. [online] Available at: <http://www.eia.gov/pub/oil_gas/natural_gas/analysis_publications/maps/maps.htm> [Accessed 1 Jan. 2015].

U.S. EIA, 2015d. *Pennsylvania Wells Data*. [online] Available at: <https://github.com/FracTrackerAlliance/PA> [Accessed 1 Jan. 2015].

U.S. EIA, 2015e. *Total Carbon Dioxide Emission from Primary Energy Resoruces Combustion*. [online] Available at: <http://www.eia.gov/cfapps/ipdbproject/iedindex3.cfm?tid=90&pid=44&aid=8&cid=ww,&syid=1980&eyid=2012&unit=MMTCD> [Accessed 10 Jan. 2015].

U.S. EIA, 2015f. *Total Primary Energy Consumption (Quadrillion Btu)*. [online] Available at: <http://www.eia.gov/cfapps/ipdbproject/IEDIndex3.cfm?tid=44&pid=44&aid=2> [Accessed 10 Jan. 2015].

U.S. EIA, 2015g. *USA Shale Gas Production*. [online] Available at: <http://www.eia.gov/dnav/ng/ng_prod_shalegas_s1_a.htm> [Accessed 1 Jan. 2015].

U.S. EPA, 2013a. *Global Greenhouse Gas Emissions Data*. [online] Available at: <http://www.epa.gov/climatechange/ghgemissions/global.html>. [Accessed 10 Jan. 2015].

U.S. EPA, 2013b. *Overview of Greenhouse Gases*. [online] Available at: <http://epa.gov/climatechange/ghgemissions/gases/ch4.html>. [Accessed 1 Jan. 2015].

Wilcox, J., Gopstein, a M., Arent, D., Wofsy, S., Brown, N.J., Bradley, R. and Stucky, G.D., 2014. Methane Leaks from North American Natural Gas Systems. *Science*, 343(6172), pp.733–735. [online] Available at: <http://www.sciencemag.org/content/343/6172/733.full>. [Accessed 1 Jan. 2015].

World Bank, 2010. Economics of Adaptation to Climate Change: Synthesis Report. *The Worldbank*, [online] pp.1 – 136. Available at: <http://documents.worldbank.org/curated/en/2010/01/16436675/economics-adaptation-climate-change-synthesis-report>. [Accessed 10 April 2015].

World Energy Council, 2015. *World Energy Issues Monitor 2015*. [online] Available at: <https://www.worldenergy.org/data/issues/> [Accessed 1 May 2015].

6 Appendices

In this section, required data for climate simulation (Appendix A) and methane emission mapping and evaluation (Appendix B) is provided. At the end of this section, link addresses to access to the dataset (Appendix C) where the data was retrieved (Table 25, Table 26 and Table 27), also the programming code by MATLAB (Appendix D) are provided.

6.1 Appendix A (Climate Simulation)

The only driving force in temperature rise in climate simulation in this study was atmospheric change of GHGs.

6.1.1 EdGCM input

The input of EdGCM was based on historical real data of GHGs and extrapolations.

6.1.1.1 Real Data of Atmospheric GHGs Concentrations

In Fig. 28 the available variation trends in atmospheric GHGs from two sources (IPCC, and EEA) are shown.

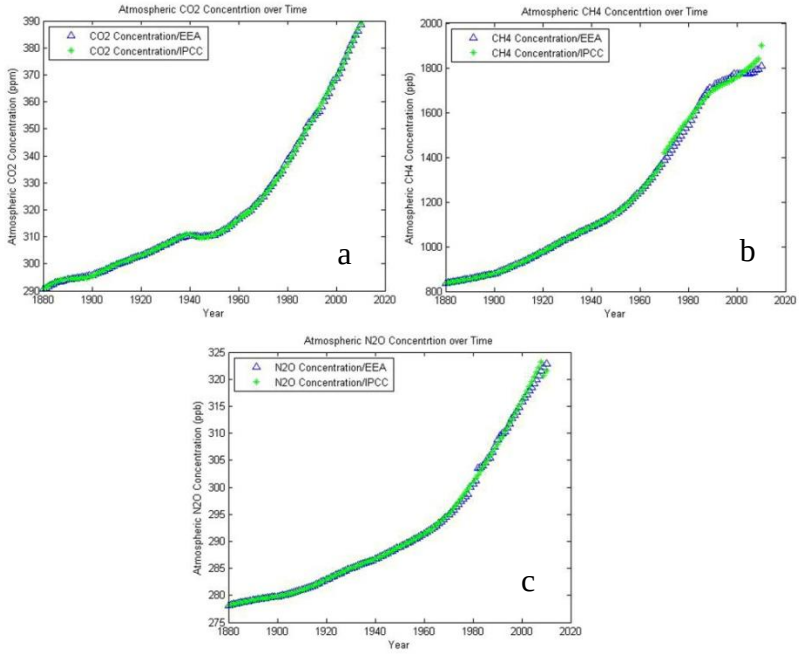

Figure 28-Atmospheric GHGs concentration, green stars are adopted from IPCC (2014b), blue rectangles in (a) are retrieved from EEA (2013a), in (b) are retrieved from EEA (2013b), and in (c) are retrieved from EEA (2013c)

6.1.1.2 Extrapolated Atmospheric Concentrations of GHGs

Data preparation for N_2O and CH_4 was based on fitting over mean historical data values from IPCC and EEA database since 1750, and extrapolating the fitting models to estimate future atmospheric concentration of CH_4 and N_2O for ANG scenarios.

Based on the IPCC and EEA data since 1750 until 1990, there is exponential increase in atmospheric CH_4 concentration, but since 1990 until 2012 the increase in atmospheric CH_4 concentration had slowed down considerably, so in order to get better data preparation for atmospheric CH_4 concentration for simulations, two fitting models over the data with highest

accuracy among all possible models were done; Gaussian and exponential fitting. Finally, mean values of the two models were considered as future atmospheric CH_4 concentration for ANG scenarios. In Fig. 29, the extrapolated data for ANG scenarios until 2050 is presented.

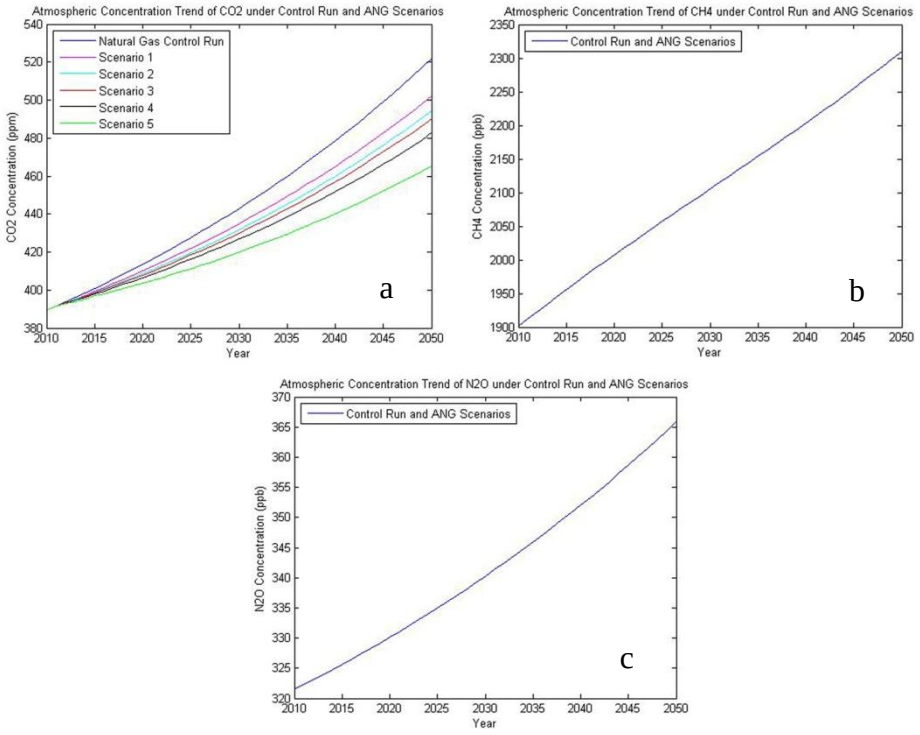

Figure 29- Atmospheric GHGs input for simulations by EdGCM, the (a) graph shows CO_2 variation trend, the (b) graph shows CH_4 variation trend, and the (c) graph shows N_2O variation trend

In Table 20 the fitting properties over atmospheric CH_4 concentrations are represented.

Table 20- Fitting models properties over mean value of atmospheric CH_4 concentration data from 1750 until 2012 from two datasets (EEA, 2013b)

Fitting model	Equation	a		b		c		d	R-square
Exponential	a*exp(b*year)+c*exp(d*x)	4.897e5		-0.003824		4.887e-6		97e-4	0.9872
Gaussian	a1*exp(-((year-b1)/c1)^2)+ a2*exp(-((year-b2)/c2)^2)	a1	a2	b1	b2	c1	c2	-	0.9982
		731.6	5.3e16	2005	3.8e4	47.73	6440		

As it can be understood from R-square values in Table 4, both models were fitted over the data by both models well.

In Table 21 the fitting properties over atmospheric N_2O concentrations are represented.

Table 21- Fitting model properties over atmospheric N_2O concentration data from 1750 until 2012 from two datasets

Fitting model	Equation	a		b		c		R-square
Gaussian	a1*exp(-((year-b1)/c1)^2)+ a2*exp(-((year-b2)/c2)^2)	a1	a2	b1	b2	c1	c2	0.999
		84.65	3.83e14	2086	2.4e5	83.43	4.5e4	

As it can be understood from R-square values of Gaussian models in Table 21 were fitted over the data by Gaussian model well.

6.2 Appendix B (Methane Emission Mapping and Evaluation)

In order to evaluate methane emission at ROIs it was necessary to model atmospheric transmittance spectrum which was done by HITRAN on web.

6.2.1 Methane Emission Mapping Techniques

In this part, the new technique of mapping CH4 plume (residual energy) compared with other techniques in homogeneous area (Fig. 30), and heterogeneous area (Fig. 31).

6.2.1.1 Homogeneous Area (ROI_CA, CA, USA)

In Fig. 30, the results of mapping CH_4 emission at ROI_CA which is homogeneous ROI using different methods are shown. As it can be understood from Fig. 30, the methane emission mapping techniques give similar pattern.

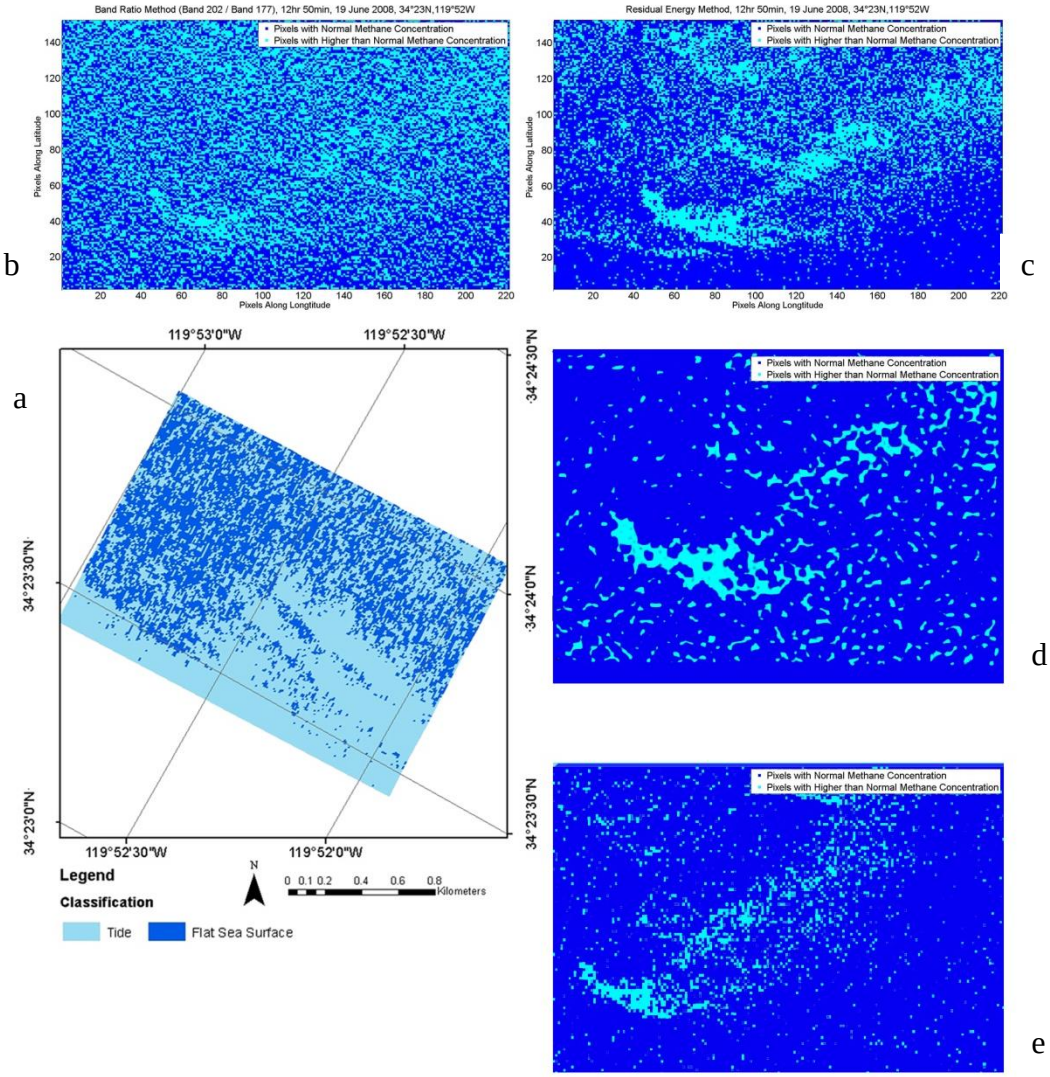

Figure 30- Comparison of residual energy technique with other techniques over ROI_CA, CA, USA, the (a) map shows ROI_CA (homogeneous ROI) produced by ArcMap, the (b) map shows result of band ratio technique, the (c) graph shows residual energy technique, the (d) graph shows result of radiation

residual technique and redrawn from Bradley et al. (2011, p. 2), and the (e) map shows result of cluster-tuned matched filter technique and redrawn from Thorpe, Frankenberg, and Roberts (2014, p. 502)

6.2.1.2 Heterogonous Area (Inglewood, LA, USA)

In Fig. 31, the results of mapping CH_4 emission at a ROI in Inglewood, LA, USA which is heterogeneous ROI using different methods are shown. As it can be understood from Fig. 31, the two techniques point to almost the same methane emission pixels.

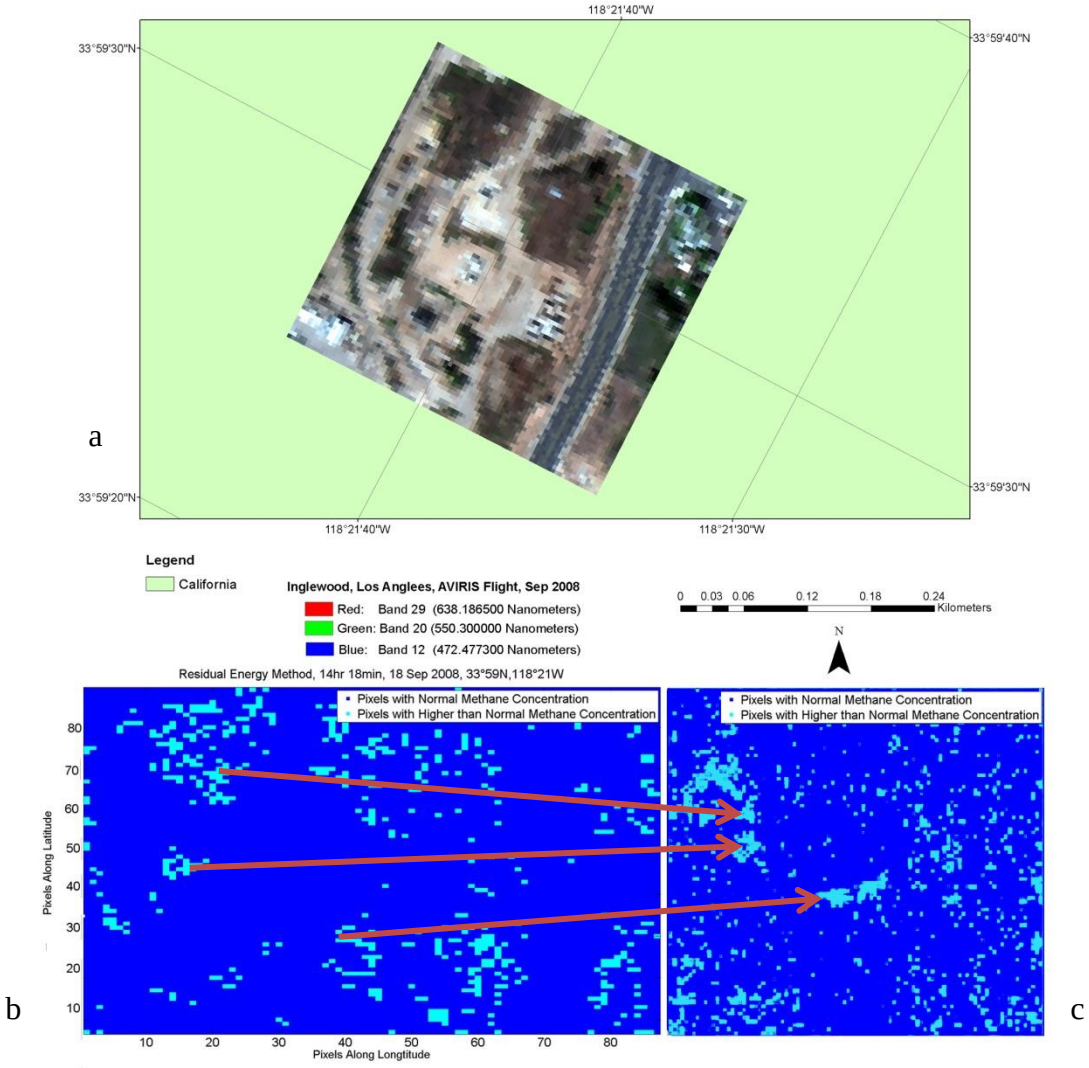

Figure 31- Comparison of residual energy technique with the technique introduced by Thorp et al. (2014) in Inglewood, LA, USA, the (a) map shows the heterogeneous ROI in Inglewood in true colouring, the (b) shows result of residual energy method, and the (c) is output of cluster- tuned matched filter technique redrawn from Thorp et al. (2014, p. 499)

6.2.2 Methane Emission Evaluation

After mapping the pixels of methane emission, it is time to evaluate the emission which deals with quantifying the flux of fugitive methane emission from the mapped pixels.

6.2.2.1 HITRAN on web Modelling Input

In this part the data preparation for modelling atmospheric transmittance spectrum at ROIs, are provided in figures (from Fig. 32 to Fig. 35).

6.2.2.1.1 Atmospheric Gas Profile

The general mixing ratio of profile of O_2, O_3, N_2O, CO_2 and CH_4 are presented in Fig. 32.

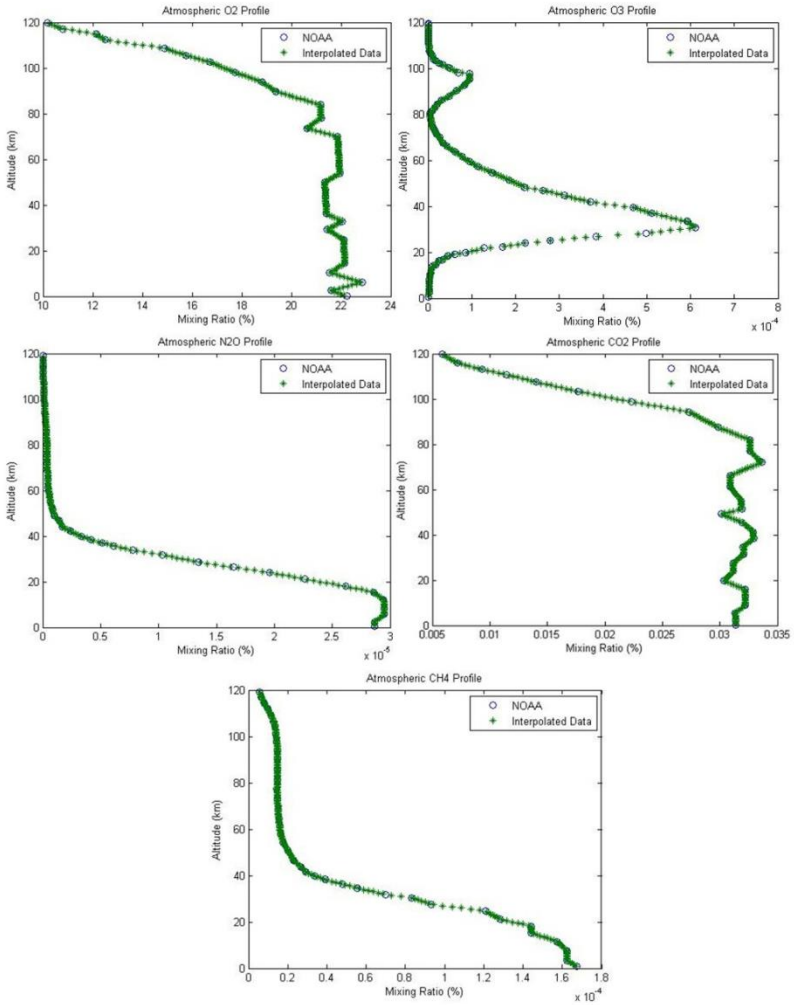

Figure 32- Mixing ratio of some of atmospheric gases, redrawn from Brasseur et al. (1999, p. 9) in Schlatter (2009, p. 21)

6.2.2.1.2 Atmospheric Relative Humidity

The relative humidity profile for each flight was requested from Atmospheric Correction Parameter Calculator of NASA (Fig. 33).

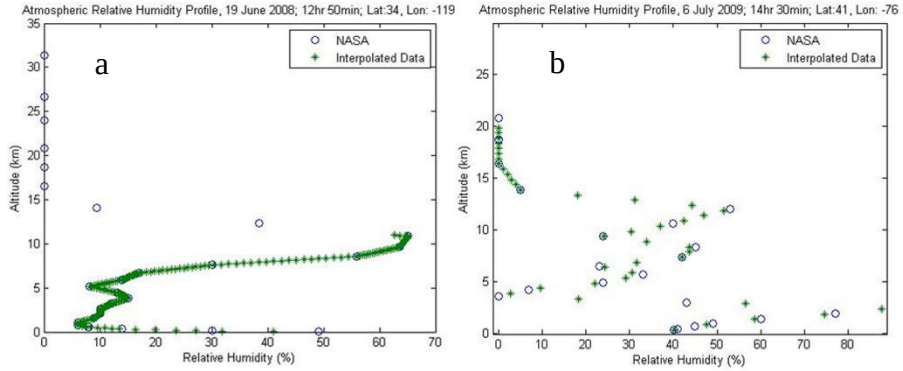

Figure 33- Atmospheric relative humidity profile; the (a) graph is for ROI_CA and the (b) graph is for ROI_PA_A and ROI_PA_B (GSFC/NASA, 2014)

6.2.2.1.3 Atmospheric Pressure Profile

The relative pressure profile for each flight was requested from Atmospheric Correction Parameter Calculator of NASA (Fig. 34).

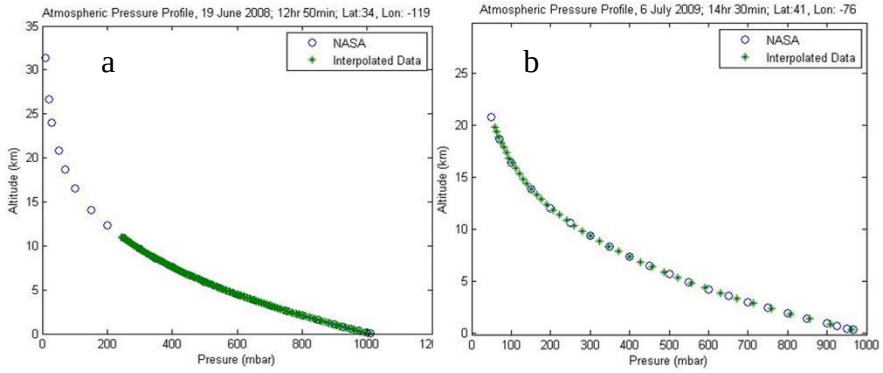

Figure 34- Atmospheric pressure profile; the (a) graph is for ROI_CA and the (b) graph is for ROI_PA_A and ROI_PA_B (GSFC/NASA, 2014)

6.2.2.1.4 Atmospheric Temperature Profile

The relative temperature profile for each flight was requested from Atmospheric Correction Parameter Calculator of NASA (Fig. 35).

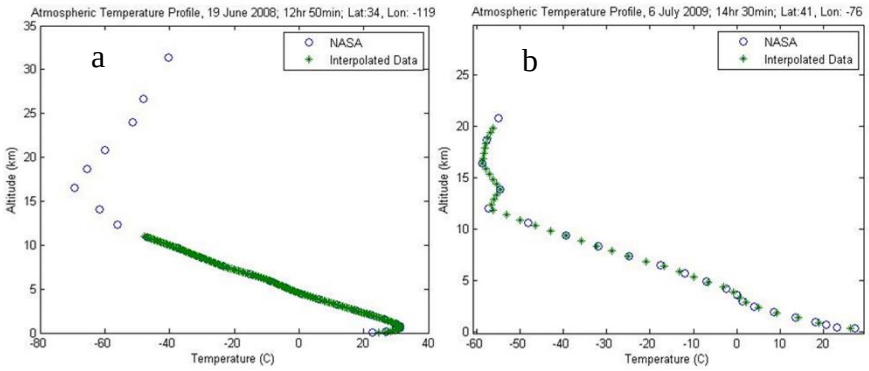

Figure 35- Atmospheric temperature profile; the (a) graph is for ROI_CA and the (b) graph is for ROI_PA_A and ROI_PA_B (GSFC/NASA, 2014)

6.2.2.1.5 Atmospheric Layers

After retrieving atmospheric mixing ratio profile of gases along with pressure and temperature profiles, the data was prepared for modelling atmospheric transmittance spectrum for each flight (Table 22 and Table 23).

6.2.2.1.5.1 Reference Point (ROI_CA)

In Table 22, the data used for atmospheric transmittance modelling by HITRAN on web for ROI_CA is presented.

Table 22- Atmospheric properties of ROI_CA for modelling by HITRAN on web

Atmospheric Layers	Height (m)	Mixing Ratio of Atmospheric Gases								Temperature (C)	Pressure (mbar)
		H2O (%)	CO2 (%)	O3 (%)	N2O (%)	CO (%)	CH4 (%)	O2 (%)	N2 (%)		
0	100	0.77839	0.031368114	1.81183E-06	2.86829E-05	0.000015	0.000167	21.71234351	77.393229	24.57092308	1013.25
1	400	0.42932	0.031368114	1.81183E-06	2.86829E-05	0.000015	0.000167	22.11234351	77.393229	29.53026126	978.6036036

930.1687764	854.8418972	761.7540687	676.4274062	597.9739508	527.3825503	463.2754342	405.0857143
31.28508861	26.71071344	18.15882278	9.065724307	0.460539797	-6.226162416	-13.52192804	-22.60675657
77.393229	77.393229	77.393229	77.393229	77.393229	77.393229	77.393229	77.393229
21.8616288	21.61091409	21.90678196	22.26349596	22.62020997	22.74166748	22.43036182	22.11905616
0.000165113	0.000163226	0.000162455	0.000162416	0.000162377	0.000162338	0.000161808	0.000160576
0.000015	0.000015	0.000015	0.000015	0.000015	0.000015	0.000015	0.000015
2.8676E-05	2.88125E-05	2.90662E-05	2.93199E-05	2.94889E-05	2.94818E-05	2.94746E-05	2.94675E-05
1.86637E-06	1.94739E-06	2.05331E-06	2.19997E-06	2.35099E-06	2.63828E-06	3.20836E-06	3.78826E-06
0.031360596	0.031353079	0.03134554	0.031337997	0.031330453	0.031582931	0.031860071	0.03213721
0.21391	0.241594	0.19363	0.166901	0.105777	0.061903	0.056432	0.049728
500	1000	1000	1000	1000	1000	1000	1000
2	3	4	5	6	7	8	9

10	1000	0.053396	0.032218369	4.37206E-06	2.94604E-05	0.000015	0.000159343	21.8077505	77.393229	-29.6817217	352.6998962
11	1000	0.03641	0.032210619	5.86788E-06	2.94533E-05	0.000015	0.00015811	21.5685522	77.393229	-36.35157486	306.1922366

6.2.2.1.5.2 Shale Gas Exploitation Areas (ROI_PA_A and ROI_PA_B)

In Table 23, the data used for atmospheric transmittance modelling by HITRAN on web for ROI_PA_A and ROI_PA_B is presented.

Table 23- Atmospheric properties of ROI_PA_A and ROI_PA_B for modelling by HITRAN on web

Atmospheric Layers	Height (m)	Mixing Ratio of Atmospheric Gases								Temperature (C)	Pressure (mbar)
		H2O (%)	CO2 (%)	O3 (%)	N2O (%)	CO (%)	CH4 (%)	O2 (%)	N2 (%)		
0	367	1.05885	0.031368	1.81E-06	2.87E-05	0.000015	0.000170	21.91234	77.393229	33.2861	1025.5
1	633	0.84282	0.031368	1.81E-06	2.87E-05	0.000015	0.000167	22.11234	77.393229	24.09936	945.6545
2	1000	0.70513	0.031361	1.87E-06	2.87E-05	0.000015	0.000165	21.86163	77.393229	14.12554	857.3691
3	1000	0.53526	0.031353	1.95E-06	2.88E-05	0.000015	0.000163	21.61091	77.393229	5.403088	760.2638

672.0942	592.7607	521.6206	457.4968	399.6837	347.7404	301.2391	259.962	223.1869	191.291
0.577329	-3.50209	-9.89484	-16.9663	-24.8592	-32.3308	-39.3558	-46.41	-52.9758	-56.2506
77.393229	77.393229	77.393229	77.393229	77.393229	77.393229	77.393229	77.393229	77.393229	77.393229
21.90678	22.2635	22.62021	22.74167	22.43036	22.11906	21.80775	21.56856	21.71393	21.85931
0.000162	0.000162	0.000162	0.000162	0.000162	0.000161	0.000159	0.000158	0.000156	0.000152
0.000015	0.000015	0.000015	0.000015	0.000015	0.000015	0.000015	0.000015	0.000015	0.000015
2.91E-05	2.93E-05	2.95E-05	2.95E-05	2.95E-05	2.95E-05	2.95E-05	2.95E-05	2.94E-05	2.92E-05
2.05E-06	2.20E-06	2.35E-06	2.64E-06	3.21E-06	3.79E-06	4.37E-06	5.87E-06	7.11E-06	8.25E-06
0.031346	0.031338	0.108026	0.031583	0.03186	0.032137	0.032218	0.032211	0.032203	0.032195
0.176806	0.071818	0.1514	0.072285	0.054466	0.031945	0.0135582	0.0089548	0.00616	0.0043681
1000	1000	1000	1000	1000	1000	1000	1000	1000	1000
4	5	6	7	8	9	10	11	12	13

163.624	140.2799	120.8398	102.2692	87.61566	74.50885	63.62699
-55.2572	-55.3657	-56.999	-58.3232	-58.2546	-57.6797	-56.7215
77.393229	77.393229	77.393229	77.393229	77.393229	77.393229	77.393229
22.00469	22.15007	22.15007	22.14474	22.13942	22.1341	22.12878
0.000149	0.000145	0.000144	0.000144	0.000144	0.00014	0.000135
0.000015	0.000015	0.000015	0.000015	0.000015	0.000015	0.000015
2.89E-05	2.87E-05	2.80E-05	2.71E-05	2.61E-05	2.50E-05	2.39E-05
1.19E-05	1.93E-05	2.40E-05	3.58E-05	4.34E-05	5.86E-05	8.89E-05
0.032187	0.03218	0.032172	0.031888	0.031414	0.03094	0.030466
0.0025699	0.0006939	0.0003428	0.0000687	0.0000214	0.000029	0.000046
1000	1000	1000	1000	1000	1000	1000
14	15	16	17	18	19	20

6.2.2.2 At Sensor Radiation Modelling Input

In order to model radiation at sensor for each ROI, atmospheric transmittance spectrum (Fig. 36), at-surface irradiance (Fig. 39), land cover classification (Fig. 40), reflectance spectrum for each class (Fig. 42) and calibration values and steradian coefficients (Fig. 43) are required. The steps of at sensor radiation modelling are explained in Diagram.13.

6.2.2.2.1 HITRAN Output (Atmospheric Transmittance and Intensity Stick Spectrum)

In Fig. 36, outputs of atmospheric transmittance spectrums using HITRAN on web are presented.

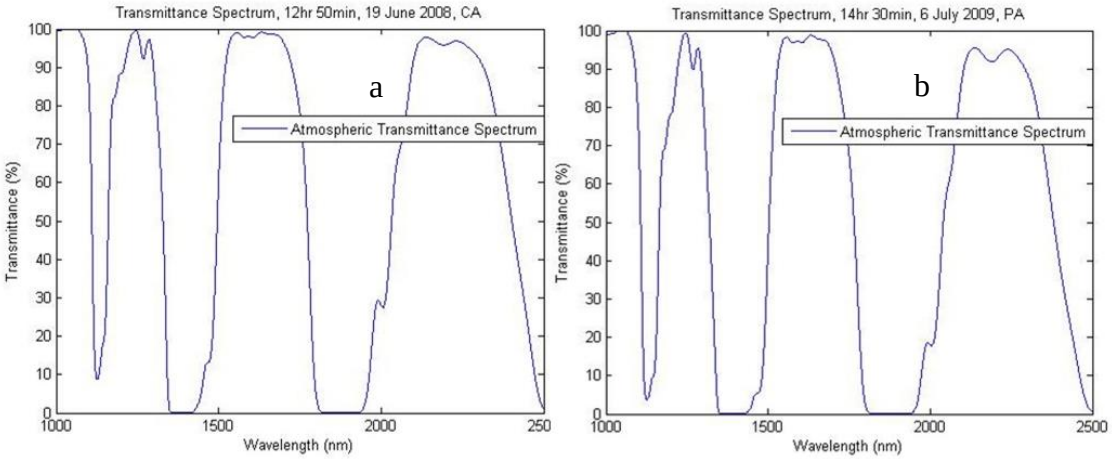

Figure 36- Atmospheric transmittance spectrum by HITRAN on web; the (a) graph was used for ROI_CA and the (b) graph was used for ROI_PA_A and ROI_PA_B

In Fig. 37, intensity stick spectrum of band 202 of AVIRIS is presented. As it is clear from Fig. 37, there is strong absorption by CH_4 in this wavelength range. This was also reported by Thorpe, Frankenberg and Roberts (2014, p.493).

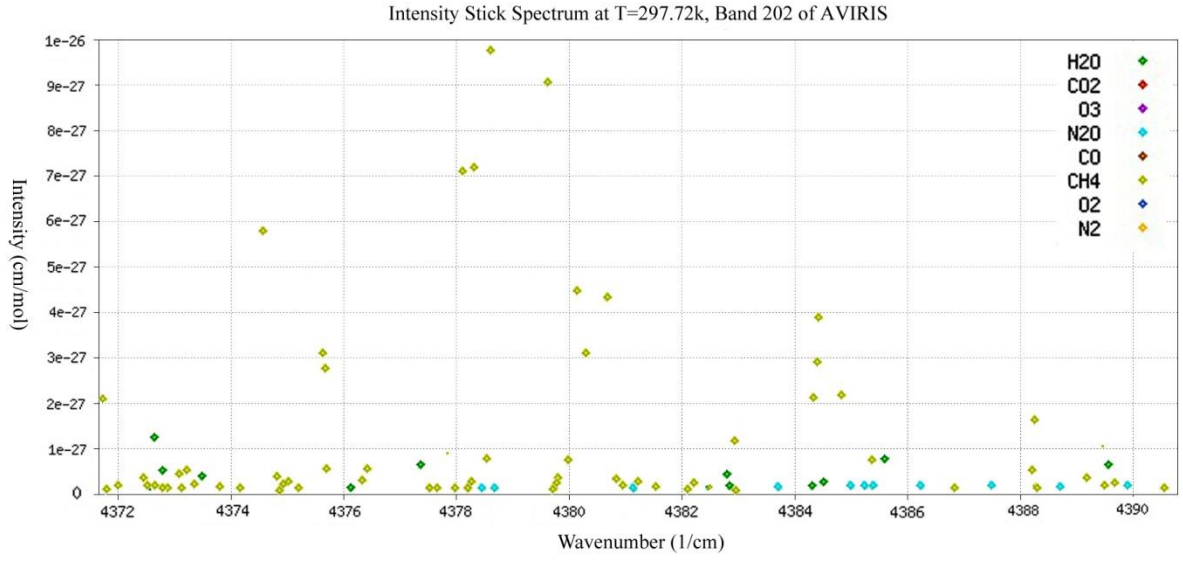

Figure 37- Intensity Stick Spectrum at Band 202 of AVIRIS

In Fig. 38, intensity stick spectrum of band 177 of AVIRIS is presented. As it is clear from Fig. 38, absorption in this wavelength range is by H_2O and CO_2, which is verified with the results by Thorpe et al., (2012, p.3)

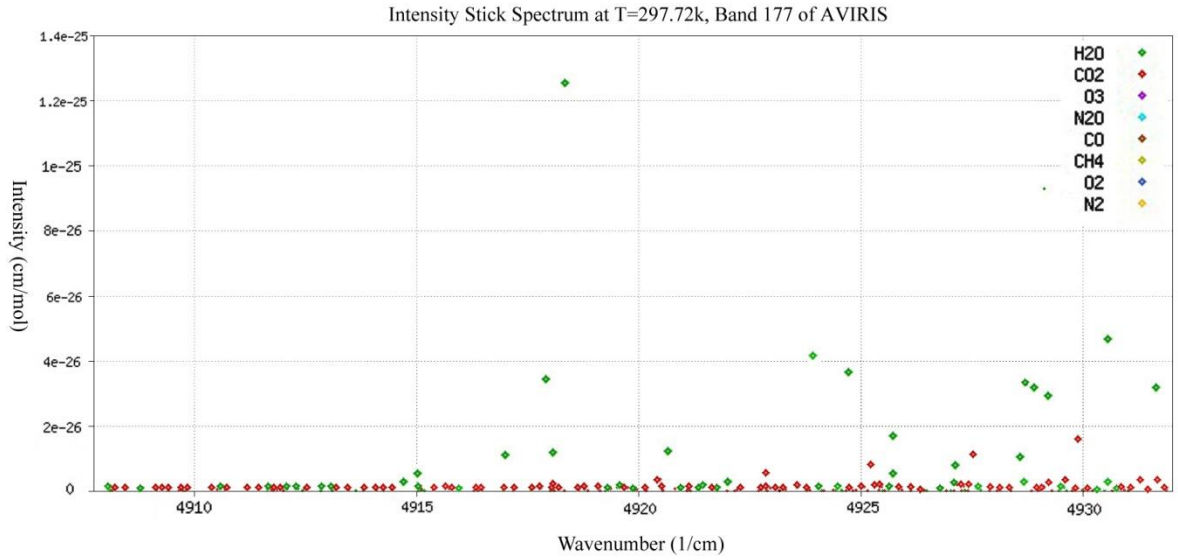

Figure 38- Intensity Stick Spectrum at Band 177 of AVIRIS

6.2.2.2.2 At Surface Irradiance

In Fig. 39, at surface irradiance spectrum for each ROI was retrieved from PV light house website. The link address to access to the website is provided in Table 26. In Fig. 39, areas under Fig. 39a_1, Fig. 39b_1 and Fig. 39b_2 are representatives of at surface energy coming from sun. The Fig. 39a_2 and Fig. 39b_3 were used to validate the irradiance spectrums (Diagram.9).

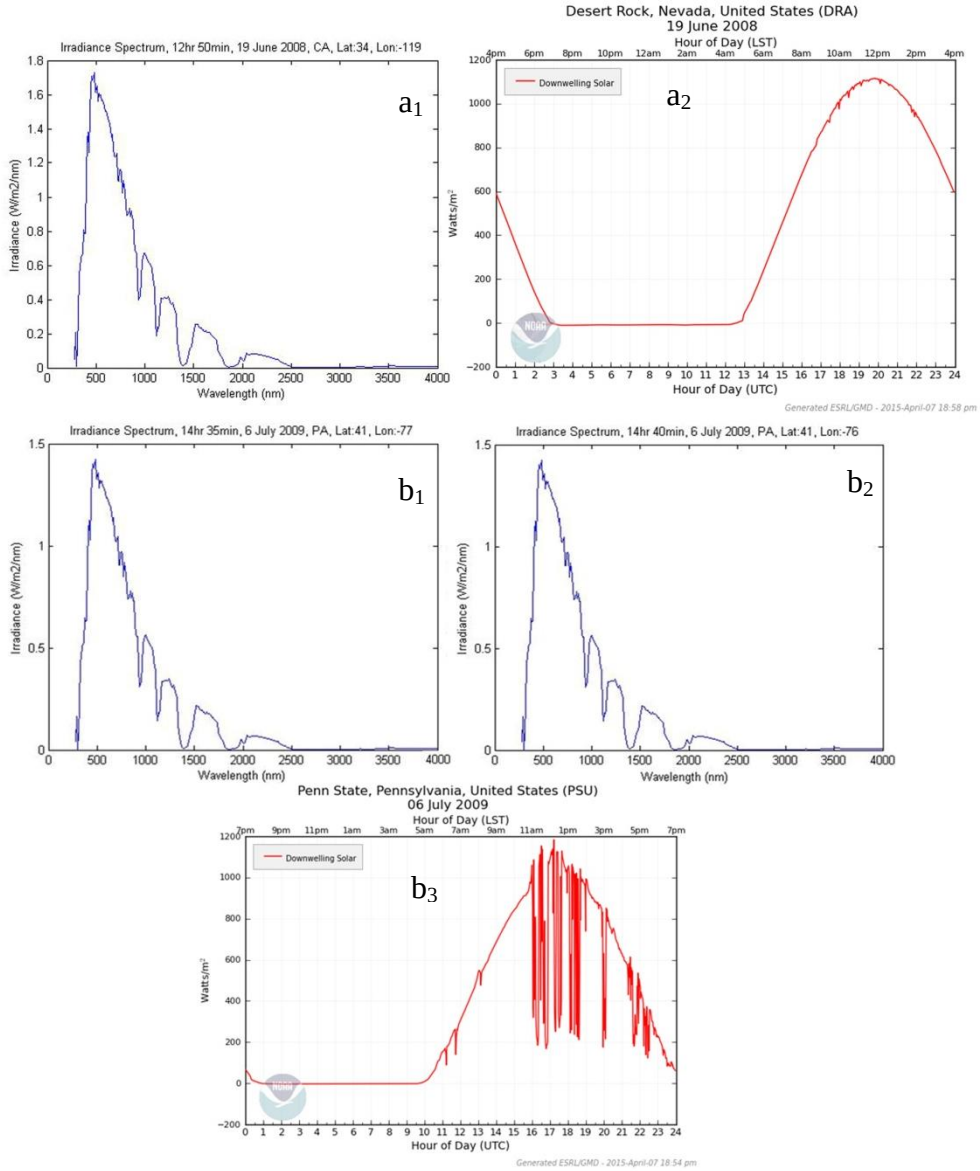

Figure 39- At surface irradiance; (a1), (b1) and (b2) are from PV light house website (PV Lighthouse, 2015), (a2), and (b3) are retrieved from NOAA (ESRL/NOAA, 2015)

6.2.2.2.3 Classification

In this section the sampling over the ROIs, band selection for neural network classification (NNC), and results of land cover classification are provided.

6.2.2.2.3.1 Sampling and Band Selection

In Fig. 40, the sampled areas across the ROIs are presented.

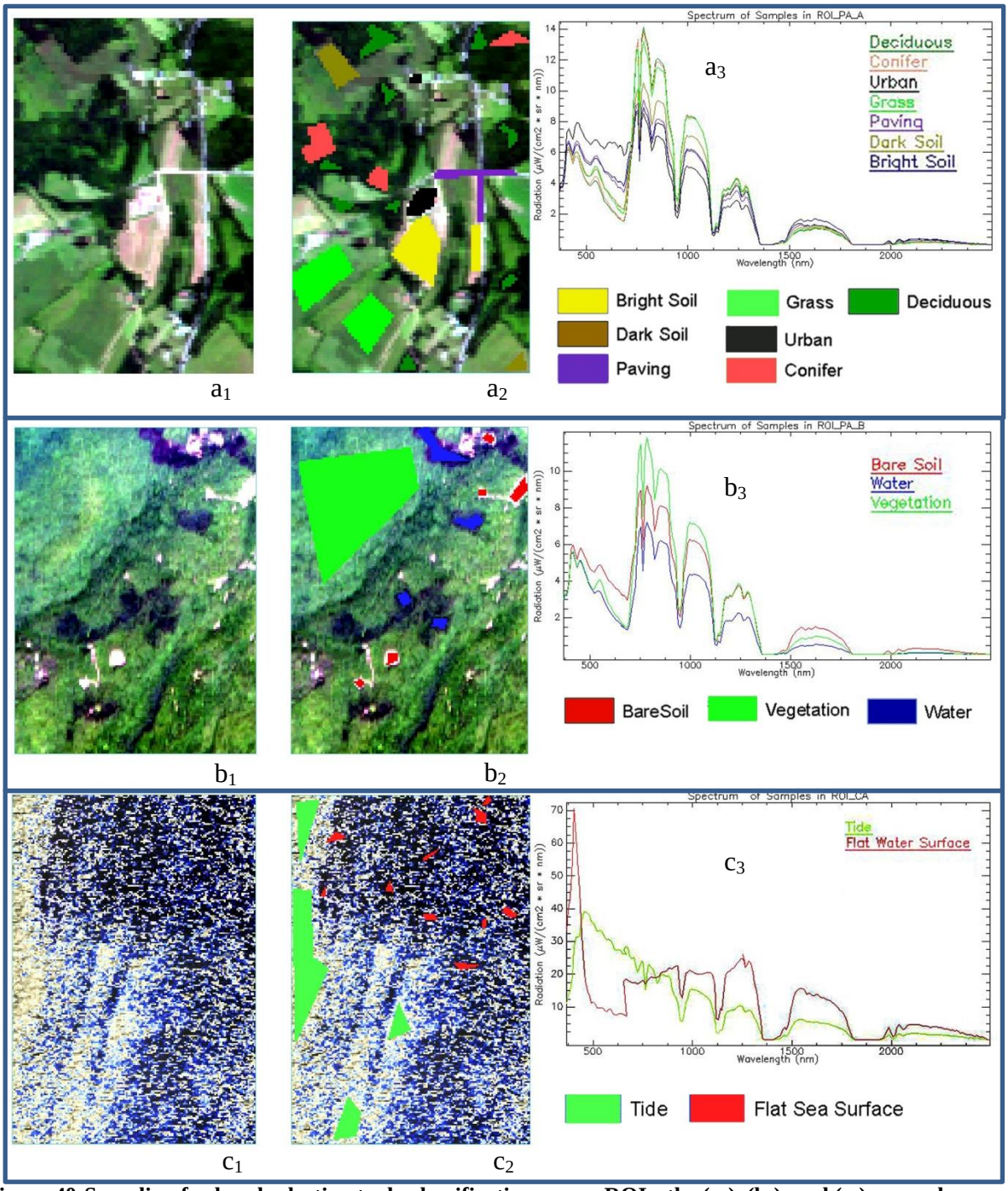

Figure 40-Sampling for band selection to do classification across ROIs, the (a_1), (b_1), and (c_1) maps show ROI_PA_A, ROI_PA_B, and ROI_CA in true colour (band 29 as red, band 20 as green, and band 12 as blue), the (a_2), (b_2), and (c_2) maps show sampled pixels, and the (a_3), (b_3), and (c_3) graphs show radiation spectrums of samples

In Fig. 41, the outputs of NNC tool of ENVI for each ROI are provided. The Fig. 41a_2, Fig. 41b_2, and Fig. 41c_2 are input of MATLAB for methane emission evaluation, which was done for checking whether the classes were imported to MATLAB correctly.

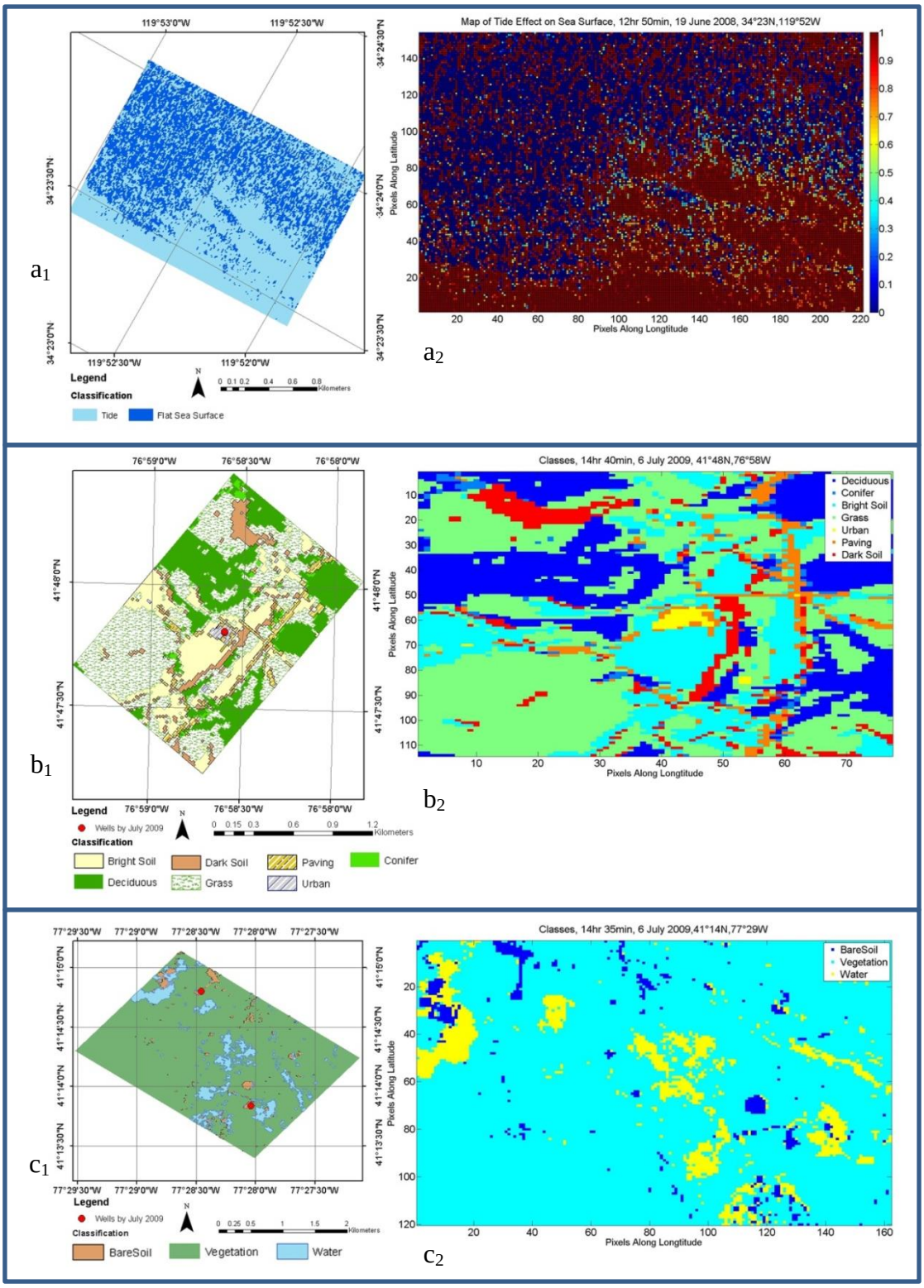

Figure 41-Classification by neural network tool of ENVI; (a_1), (b_1), and (c_1) maps show ROI_CA, ROI_PA_A, and ROI_PA_B respectively generated by ArcMap, (a_2), (b_2), and (c_2) maps show ROI_CA, ROI_PA_A, and ROI_PA_B respectively generated by MATLAB

6.2.2.2.4 Reflectance Spectrum

In Fig. 42, the reflectance spectrums for each class as shown in Fig. 37 over ROIs are plotted. The data is retrieved from ASTER reflectance library, and the link address for accessing to the ASTER library is available in Table 27.

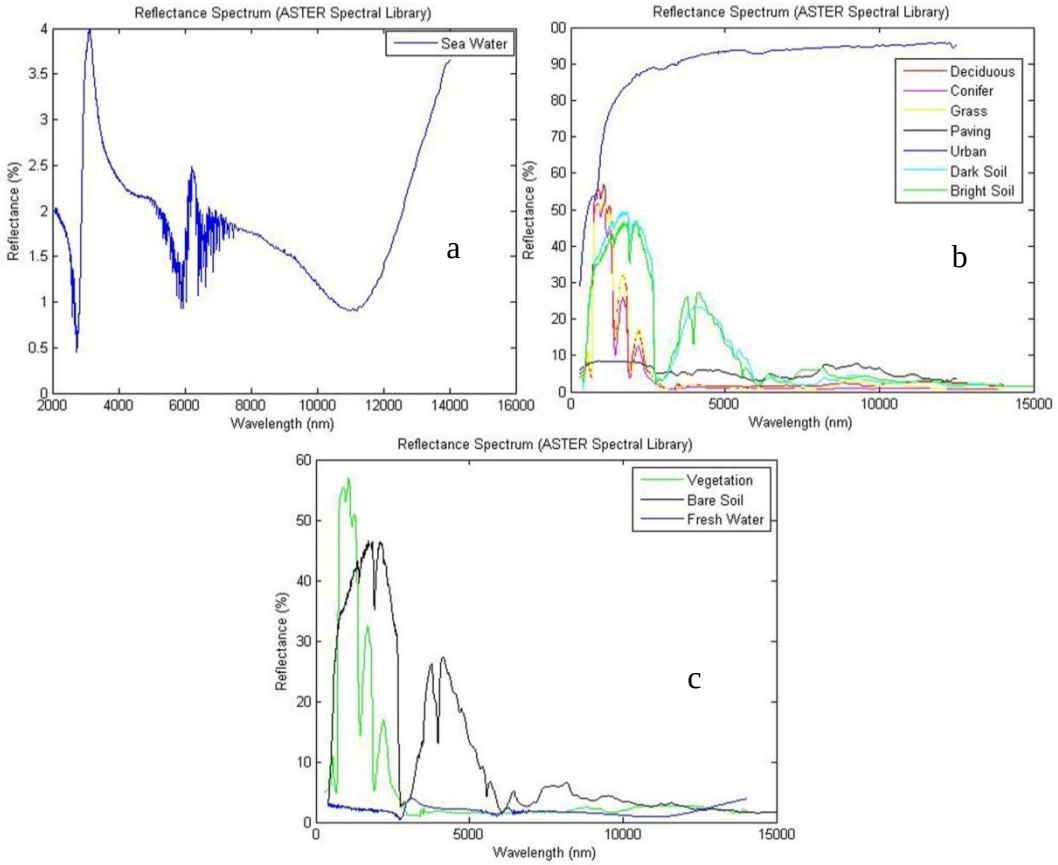

Figure 42- Reflectance spectrums for different classes; the (a) graph shows reflectance spectrum of sea water for ROI_CA, the (b) graph shows reflectance spectrums of land cover classes for ROI_PA_A and the (c) graph shows reflectance spectrums of land cover classes for ROI_PA_B (ASTER/NASA, 2015)

6.2.2.2.5 Calibration Values and Steradian Coefficients

In Fig. 43, the calibration values and steradian coefficients for each pixel across the ROIs are shown.

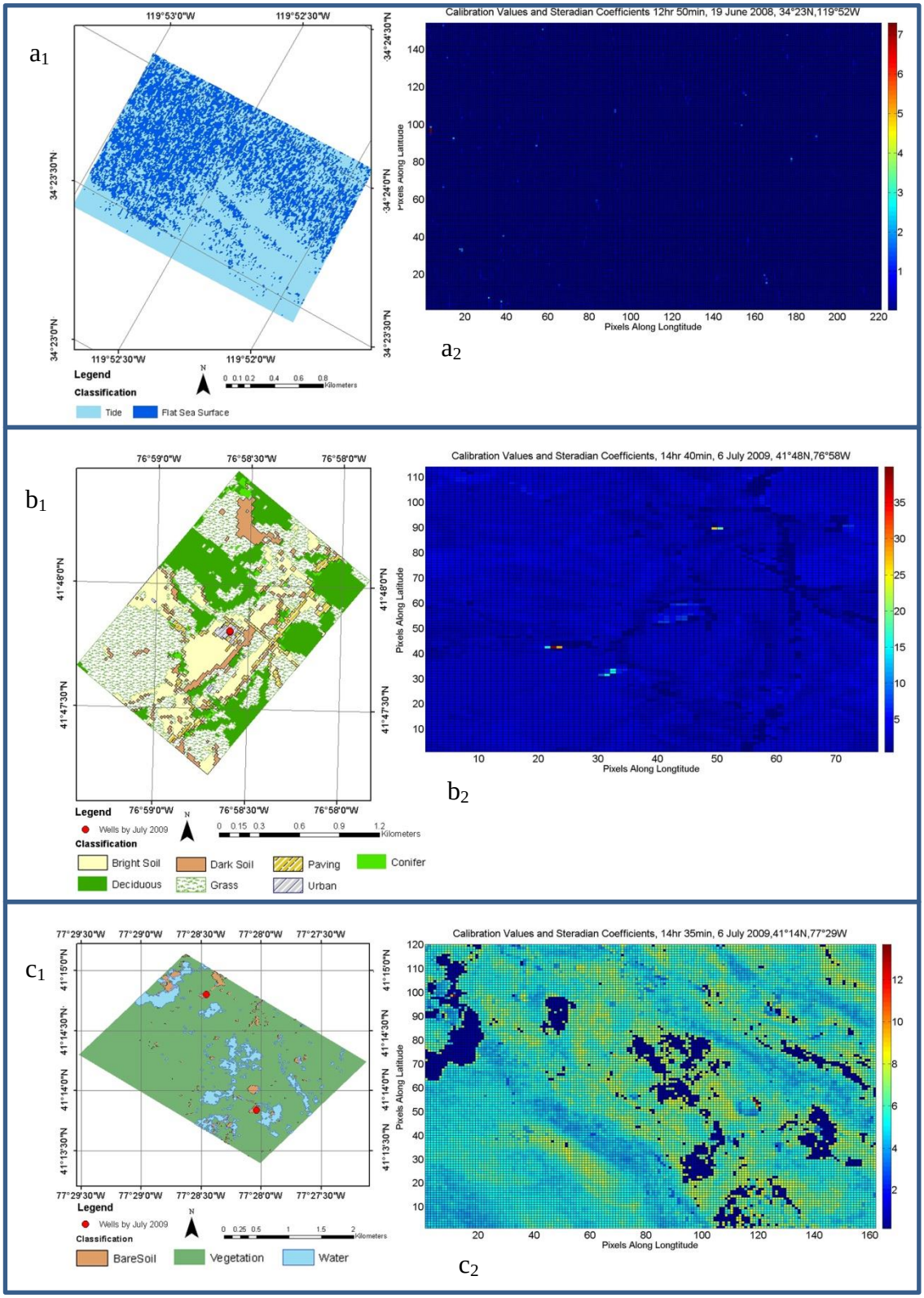

Figure 43-Calibration values and steradian coefficients; the (a_1), (b_2), and (c_1) maps show ROI_CA, the ROI_PA_A, and ROI_PA_B respectively, the (a_2), (b_2), and (c_2) maps show calibration values and steradian coefficients for ROI_CA, the ROI_PA_A, and ROI_PA_B respectively

6.2.3 AVIRIS Information

In Table 24, the information on AVIRIS band wavelength and gain value is given. AVIRIS has 224 bands which the band wavelength range is about 10 nm.

Table 24- AVIRIS Information

Band	Wavelength (nm)	Gain Value	Band	Wavelength (nm)	Gain Value	Band	Wavelength (nm)	Gain Value
1	365.9298	300	81	1120.656	300	161	1866.864	1200
2	375.594	300	82	1130.213	300	162	1876.925	1200
3	385.2625	300	83	1139.765	300	163	1886.985	1200
4	394.9355	300	84	1149.311	300	164	1897.042	1200
5	404.6129	300	85	1158.853	300	165	1907.096	1200
6	414.2946	300	86	1168.389	300	166	1917.148	1200
7	423.9808	300	87	1177.92	300	167	1927.198	1200
8	433.6713	300	88	1187.446	300	168	1937.246	1200
9	443.3662	300	89	1196.966	300	169	1947.292	1200
10	453.0655	300	90	1206.482	300	170	1957.335	1200
11	462.7692	300	91	1215.992	300	171	1967.375	1200
12	472.4773	300	92	1225.497	300	172	1977.414	1200
13	482.1898	300	93	1234.996	300	173	1987.45	1200
14	491.9066	300	94	1244.491	300	174	1997.484	1200
15	501.6279	300	95	1253.98	300	175	2007.515	1200
16	511.3535	300	96	1263.464	300	176	2017.545	1200
17	521.0836	300	97	1253.373	300	177	2027.572	1200
18	530.818	300	98	1263.346	300	178	2037.596	1200
19	540.5568	300	99	1273.318	300	179	2047.619	1200
20	550.3	300	100	1283.291	300	180	2057.639	1200
21	560.0477	300	101	1293.262	300	181	2067.656	1200
22	569.7996	300	102	1303.234	300	182	2077.672	1200
23	579.556	300	103	1313.206	300	183	2087.685	1200
24	589.3168	300	104	1323.177	300	184	2097.696	1200
25	599.0819	300	105	1333.148	300	185	2107.704	1200
26	608.8515	300	106	1343.119	300	186	2117.71	1200
27	618.6254	300	107	1353.089	300	187	2127.714	1200
28	628.4037	300	108	1363.06	300	188	2137.716	1200
29	638.1865	300	109	1373.03	300	189	2147.715	1200
30	647.9736	300	110	1383	300	190	2157.712	1200
31	657.7651	300	111	1392.969	600	191	2167.707	1200
32	667.561	300	112	1402.939	600	192	2177.699	1200
33	655.7923	300	113	1412.908	600	193	2187.689	1200
34	665.5994	300	114	1422.877	600	194	2197.677	1200
35	675.4012	300	115	1432.845	600	195	2207.662	1200
36	685.1979	300	116	1442.814	600	196	2217.645	1200
37	694.9894	300	117	1452.782	600	197	2227.626	1200
38	704.7756	300	118	1462.75	600	198	2237.604	1200

39	714.5566	300	119	1472.718	600	199	2247.581	1200
40	724.3325	300	120	1482.685	600	200	2257.554	1200
41	734.1031	300	121	1492.652	600	201	2267.526	1200
42	743.8685	300	122	1502.619	600	202	2277.495	1200
43	753.6287	300	123	1512.586	600	203	2287.462	1200
44	763.3837	300	124	1522.552	600	204	2297.427	1200
45	773.1335	300	125	1532.518	600	205	2307.389	1200
46	782.8781	300	126	1542.484	600	206	2317.349	1200
47	792.6174	300	127	1552.45	600	207	2327.307	1200
48	802.3516	300	128	1562.416	600	208	2337.262	1200
49	812.0805	300	129	1572.381	600	209	2347.216	1200
50	821.8043	300	130	1582.346	600	210	2357.167	1200
51	831.5228	300	131	1592.311	600	211	2367.115	1200
52	841.2361	300	132	1602.275	600	212	2377.061	1200
53	850.9442	300	133	1612.24	600	213	2387.005	1200
54	860.6471	300	134	1622.204	600	214	2396.947	1200
55	870.3448	300	135	1632.167	600	215	2406.886	1200
56	880.0372	300	136	1642.131	600	216	2416.823	1200
57	889.7245	300	137	1652.094	600	217	2426.758	1200
58	899.4066	300	138	1662.057	600	218	2436.69	1200
59	909.0834	300	139	1672.02	600	219	2446.62	1200
60	918.7551	300	140	1681.983	600	220	2456.548	1200
61	928.4214	300	141	1691.945	600	221	2466.473	1200
62	938.0827	300	142	1701.907	600	222	2476.396	1200
63	947.7387	300	143	1711.869	600	223	2486.317	1200
64	957.3895	300	144	1721.831	600	224	2496.236	1200
65	967.0351	300	145	1731.792	600			
66	976.6755	300	146	1741.753	600			
67	986.3106	300	147	1751.714	600			
68	995.9406	300	148	1761.675	600			
69	1005.565	300	149	1771.635	600			
70	1015.185	300	150	1781.596	600			
71	1024.799	300	151	1791.556	600			
72	1034.408	300	152	1801.515	600			
73	1044.012	300	153	1811.475	600			
74	1053.611	300	154	1821.434	600			
75	1063.204	300	155	1831.393	600			
76	1072.793	300	156	1841.352	600			
77	1082.376	300	157	1851.31	600			
78	1091.954	300	158	1861.269	600			
79	1101.526	300	159	1871.227	600			
80	1111.094	300	160	1872.384	600			

6.3 Appendix C (Access Links to Datasets)

In this section the links addresses to access to the databases used in this study are provided (Table 25, Table 26, and Table 27).

6.3.1 Natural Gas Production

In Table 25, the links for getting general information about overall natural gas production along with shale gas production is provided.

Table 25- Link addresses for accessing to information on natural gas production in USA

Database	Purpose	Link
U.S. EIA	USA gross natural gas production	http://www.eia.gov/cfapps/ipdbproject/iedindex3.cfm?tid=3&pid=3&aid=1&cid=US,&syid=1990&eyid=2012&unit=BCF
U.S. EIA	USA shale gas production	http://www.eia.gov/dnav/ng/ng_prod_shalegas_s1_a.htm

6.3.2 Climate Simulations

In Table 26, the access links for getting required data for climate simulation are presented.

Table 26- Link addresses for accessing to data retrieve for climate simulation by EdGCM

Database	Purpose		Link
U.S. EIA	Global energy consumption		http://www.eia.gov/cfapps/ipdbproject/IEDIndex3.cfm?tid=44&pid=44&aid=2
U.S. EIA	CO_2 emission from primary resources combustion		http://www.eia.gov/cfapps/ipdbproject/iedindex3.cfm?tid=90&pid=44&aid=8&cid=ww,&syid=1980&eyid=2012&unit=MMTCD
IPCC Data Distribution Centre	Atmospheric gas concentration		http://www.ipcc-data.org/observ/index.html
EEA Dataset	Atmospheric gas concentration	CO_2	http://www.eea.europa.eu/data-and-maps/figures/atmospheric-concentration-of-co2-ppm-1
		CH_4	http://www.eea.europa.eu/data-and-maps/figures/atmospheric-concentration-of-ch4-ppb-1
		N_2O	http://www.eea.europa.eu/data-and-maps/figures/atmospheric-concentration-of-n2o-ppb-1
NASA Goddard Institute for Space Studies	Actual global mean temperature		http://data.giss.nasa.gov/gistemp/tabledata_v3/GLB.Ts+dSST.txt

6.3.3 Methane Emission Mapping and Evaluation

In Table 27, access links for getting information for fugitive methane emission mapping and evaluation are provided.

Table 27- Link addresses for accessing to data retrieve for methane mapping and evaluation

Database	Purpose	Link
JPL/NASA	AVIRIS imagery	http://aviris.jpl.nasa.gov/
HITRAN	Atmospheric transmittance modelling	http://hitran.iao.ru/
ASTER Library of JPL/NASA	Reflectance spectrum	http://speclib.jpl.nasa.gov/
PV Light House	At surface irradiance spectrum	http://www.pvlighthouse.com.au/
The Optical Remote Sensing Laboratory of The City College of New York	Relative humidity to atmospheric water vapour mixing ratio	http://sky.ccny.cuny.edu/mn/pub/dewpointcalculator2.php
Earth System Research Library of NOAA	At surface energy	http://www.esrl.noaa.gov/gmd/grad/surfrad/
Atmospheric Correction Parameter Calculator of NASA	Atmospheric pressure, temperature and relative humidity profile	http://atmcorr.gsfc.nasa.gov/
ArcGIS	PA counties	http://www.arcgis.com/home/item.html?id=04e3f70b4b7f401faafd431da9355ab4
ArcGIS	Gas well locations in PA	https://github.com/FracTrackerAlliance/PA
ArcGIS	State boundary of USA	http://www.arcgis.com/home/item.html?id=f7f805eb65eb4ab787a0a3e1116ca7e5
U.S. EIA	Shale basin boundaries	http://www.eia.gov/pub/oil_gas/natural_gas/analysis_publications/maps/maps.htm
U.S. EIA	Production of Natural Gas per Rig per Day	http://www.eia.gov/petroleum/drilling/

6.4 Appendix D (MATLAB Codes)

In this study, MATLAB was used for majority of calculations, and estimations, mainly for fugitive methane emission mapping and evaluation part. In this section the main code for methane mapping and evaluation used for the reference point (ROI_CA) is provided. The same code structure with some slight modifications was used for the other two ROIs (ROI_PA_A and ROI_PA_B).

6.4.1 Reference Point (ROI_CA)

In this study, the MATLAB code had a main body as presented, with support of two functions; Transmittance_HITRAN, RadiationModelling.

6.4.1.1 Body of Code

The main part of the methane emission mapping and evaluation code was as follows:

```
clc;
close all;
clear all;
format long;
%% Inputs
% 152 samples x 276 lines x 1 band
Class=dlmread('Classification_coal_Oil_Methane.txt');
[Row,Column]=size(Class);
% Radiation values at different Wavelength
Rad_Spectrum=dlmread('Radiation_DOS_Coal_Oil_Methane_Emission.txt');

Class_Tide_Water=dlmread('Classification_Tide_Surface.txt');

% Mapping tide and flat pixels over the study area
figure
Z=Class_Tide_Water';
x = [1:Row];
y = [1:Column];
[X,Y] = meshgrid(x,y);
pcolor(X,Y,Z);
set(gca, 'FontName', 'Arial')
set(gca, 'FontSize', 24)
title('Map of Tide Effect on Sea Surface, 12hr 50min, 19 June 2008, 34°23N,119°52W')

xhandle = get(gca,'xlabel');
set(xhandle,'string','Pixels Along Longtitude','fontsize',22)

yhandle = get(gca,'ylabel');
set(yhandle,'string','Pixels Along Latitude','fontsize',22)
set(colorbar,'fontsize',14)


% (Watt/SquaredMeter/Steradian/nm)
Rad_Spectrum=abs(Rad_Spectrum)./100;
AVIRIS_Bands=dlmread('Bands_Wavelength.txt');
```

```
%Irradiance Spectrum
delimiterIn = ' ';
headerlinesIn = 1;
Irrad_Load=dlmread('Irradiance_Spectrum.txt',delimiterIn,headerlinesIn);
[M,N]=size(Irrad_Load);

for i=1:M/2
   Irrad(i,1)=Irrad_Load(i,1);
   Irrad(i,2)=Irrad_Load(373+i,1);
end

% Plotting irradiance spectrum
figure
plot(Irrad(:,1),Irrad(:,2));
xlabel('Wavelength (nm)')
ylabel('Irradiance (W/m2/nm)')
title('Irradiance Spectrum, 12hr 50min, 19 June 2008, CA, Lat:34, Lon:-119')

% Retrieving reflectance
Water=dlmread('jhu.becknic.water.sea.none.liquid.seawater.spectrum.txt');

Water(:,2)=Water(:,2)./100;
Water(:,1)=Water(:,1).*1000;

% Plotting reflectance spectrum
figure
plot(Water(:,1),Water(:,2)*100);
title('Reflectance Spectrum (ASTER Spectral Library)')
xlabel('Wavelength (nm)')
ylabel('Reflectance (%)')
legend('Sea Water')


%% Calculating the Transmittance Spectrum
% Calling Transmittance_HITRAN function
Trans_Spectrum=Transmittance_HITRAN;
% Plotting atmospheric transmittance spectrum generated by HITRAN
figure
plot(Trans_Spectrum(:,2),Trans_Spectrum(:,3).*100);
title('Transmittance Spectrum, 12hr 50min, 19 June 2008, CA')
xlabel('Wavelength (nm)')
ylabel('Transmittance (%)')
legend('Atmospheric Transmittance Spectrum')
%% Calculating calibration values and steradian coefficients at the band with max
transmittance (Band 73)

   [M,N]=max(Trans_Spectrum(:,3));
   wavelength=Trans_Spectrum(N,2);
   temp=abs(AVIRIS_Bands(1,:)-wavelength);
```

```
   [idx,idy]=min(temp);
   Band=idy;
   Row_Min=Row*(Band-1)+1;
   Row_Max=Row*(Band-1)+Row;
   Rad_Max_Tran(1:Row,1:Column)=Rad_Spectrum(Row_Min:Row_Max,:);
   temp=abs(Trans_Spectrum(:,2)-wavelength);
   [idx,idy]=min(temp);
   Trans_Value=Trans_Spectrum(idy,3);

   temp=abs(Water(:,1)-wavelength);
   [idx,idy]=min(temp);
   RefWat=Water(idy,2);
   Ref=RefWat;

   temp=abs(Irrad(:,1)-wavelength);
   [idx,idy]=min(temp);
   closests_Irrad_Wave=Irrad(idy,1);
   Irrad_Value=Irrad(idy,2);

 for i=1:Row
    for j=1:Column
       Steradian_Coeff(i,j)=Irrad_Value.*Ref.*Trans_Value./Rad_Max_Tran(i,j);
    end
 end
% Mapping calibration values and steradian coefficients
figure
Z=(Steradian_Coeff)';
x = [1:Row];
y = [1:Column];
[X,Y] = meshgrid(x,y);
pcolor(X,Y,Z);
set(gca, 'FontName', 'Arial')
set(gca, 'FontSize', 24)
title('Calibration Values and Steradian Coefficients 12hr 50min, 19 June 2008,
34°23N,119°52W')
xhandle = get(gca,'xlabel');
set(xhandle,'string','Pixels Along Longtitude','fontsize',22)
yhandle = get(gca,'ylabel');
set(yhandle,'string','Pixels Along Latitude','fontsize',22)

Tide_Count=0;
Flat_Count=0;
Sum_Tide=0;
Sum_Flat=0;
for i=1:Row
   for j=1:Column
      if Class_Tide_Water(i,j)==1
         Tide_Count=Tide_Count+1;
         Stera_Tide(1,Tide_Count)=Steradian_Coeff(i,j);
         Sum_Tide=Sum_Tide+Steradian_Coeff(i,j);
```

```
        end
        if Class_Tide_Water(i,j)==0
            Flat_Count=Flat_Count+1;
            Stera_Flat(1,Flat_Count)=Steradian_Coeff(i,j);
            Sum_Flat=Sum_Flat+Steradian_Coeff(i,j);
        end
    end
end
%% Calculation of Radiation at AVIRIS Sensor Flight Using HITRAN
%%%%% Rad at the height of AVIRIS from Irradiance, Reflectance and
%%%%% Transmittance
for Band=69:224
    Row_Min=Row*(Band-1)+1;
    Row_Max=Row*(Band-1)+Row;

    % Retrieving wavelength
    wavelength=AVIRIS_Bands(1,Band);

    % Retrieving atmospheric transmittance at the wavelength
    temp=abs(Trans_Spectrum(:,2)-wavelength);
    [idx,idy]=min(temp);
    Trans_Value=Trans_Spectrum(idy,3);

    % Retriving water reflectance
    temp=abs(Water(:,1)-wavelength);
    [idx,idy]=min(temp);
    Ref=Water(idy,2);

    % Calling radiationModelling function

Calc_Rad=RadiationModelling(Row,Column,wavelength,Class_Tide_Water,Ref,Irrad,Sterad
ian_Coeff,Trans_Value);
    Calculated_Rad(Row_Min:Row_Max,1:Column)=Calc_Rad;
end

%%
count=0;
for Band=69:224
    count=count+1;
    wavelength=AVIRIS_Bands(1,Band);
    Rad_Spectrum_1(1,count)=(Calculated_Rad(Row*(Band-1)+100,20));
    Rad_Spectrum_2(1,count)=Rad_Spectrum(Row*(Band-1)+100,20);
    temp=abs(Irrad(:,1)-wavelength);
    [idx,idy]=min(temp);
    Irrad_Value=Irrad(idy,2);
    Irrad_Spectrum_3(1,count)=Irrad_Value;
end

% Plotting actual and modelled radiation at a arbitary pixel
figure
```

```
plot(AVIRIS_Bands(1,69:224),Rad_Spectrum_1,'b');
hold on
plot(AVIRIS_Bands(1,69:224),Rad_Spectrum_2,'r');
title('Irradiation, Radiation and Calculated Radiation Spectrum at a Pixel')
xlabel('Wavelength(nm)')
ylabel('W/(m^2.nm.st)')
legend('Calculated Radiation At AVIRIS Height','Actual Radiation At AVIRIS Height')
hold off

%%
%%%%%%%%%%%%%% Mapping methane emission %%%%%%%%%%%%%%%
%%%%%%%%%%%%%% 1- Band Ratio Technique %%%%%%%%%%%%%%%%
%%%%%%%%%%%%%% 2- Residual Energy Technique%%%%%%%%%%%%%%%
%%%%%%%%%%%%%%%%%%%%%%%%%%%%%%%%%%%%%%%%%%%%%%%%%%%%%%%%
%%%%%%%%%%%%%% 1- Band Ratio Technique %%%%%%%%%%%%%%%%
%%%%%%%%%%%%%%%%%%%%%%%%%%%%%%%%%%%%%%%%%%%%%%%%%%%%%%%%
for Band=202
   Row_Min=Row*(Band-1)+1;
   Row_Max=Row*(Band-1)+Row;


Radiation_at_Band_202(1:Row,1:Column)=Rad_Spectrum(Row_Min:Row_Max,1:Column);

Radiation_at_Band_202_Calc(1:Row,1:Column)=Calculated_Rad(Row_Min:Row_Max,1:C
olumn);

   wavelength_202=AVIRIS_Bands(1,Band);

   temp=abs(Trans_Spectrum(:,2)-wavelength_202);
   [idx,idy]=min(temp);
   closests_Trans_Wave=Trans_Spectrum(idy,2);
   Trans_Value_202=Trans_Spectrum(idy,3);

   temp=abs(Irrad(:,1)-wavelength_202);
   [idx,idy]=min(temp);
   closests_Ref_Wave=Irrad(idy,1);
   Irrad_Value_202=Irrad(idy,2);

end

for Band=177
   Row_Min=Row*(Band-1)+1;
   Row_Max=Row*(Band-1)+Row;


Radiation_at_Band_177(1:Row,1:Column)=Rad_Spectrum(Row_Min:Row_Max,1:Column);

Radiation_at_Band_177_Calc(1:Row,1:Column)=Calculated_Rad(Row_Min:Row_Max,1:C
olumn);
```

```
   wavelength_177=AVIRIS_Bands(1,Band);

   temp=abs(Trans_Spectrum(:,2)-wavelength_177);
   [idx,idy]=min(temp);
   Trans_Value_177=Trans_Spectrum(idy,3);

   temp=abs(Irrad(:,1)-wavelength_177);
   [idx,idy]=min(temp);
   Irrad_Value_177=Irrad(idy,2);
end

Band_Ratio_202_177=zeros(Row,Column);
for i=1:Row
   for j=1:Column
       Band_Ratio_202_177(i,j)=Radiation_at_Band_202(i,j)./Radiation_at_Band_177(i,j);
   end
end

Sum_Band_Ratio=0;
Count=0;
Band_Ratio_202_177_Edited=zeros(Row,Column);
for i=1:Row
   for j=1:Column
      if Band_Ratio_202_177(i,j)~=Inf || Band_Ratio_202_177(i,j)==0
         Sum_Band_Ratio=Band_Ratio_202_177(i,j)+Sum_Band_Ratio;
         Count=Count+1;
         Band_Ratio_202_177_Edited(i,j)=Band_Ratio_202_177(i,j);
      end
   end
end

for i=1:Row
   for j=1:Column
      if Band_Ratio_202_177 ==Inf
         Band_Ratio_202_177_Edited(i,j)=max(Band_Ratio_202_177_Edited(:));
      end
      if Band_Ratio_202_177_Edited(i,j)==0
         Band_Ratio_202_177_Edited(i,j)=mean(Band_Ratio_202_177_Edited(:));
      end
   end
end

% Applying constraint
Reference_Transmittance=mean(Band_Ratio_202_177_Edited(:));

Methan_Map_BR=zeros(Row,Column);
for i=1:Row
   for j=1:Column
      if Band_Ratio_202_177_Edited(i,j)>Reference_Transmittance ||
Band_Ratio_202_177_Edited(i,j)<Reference_Transmittance*0.90
```

```
         Methan_Map_BR(i,j)=0;
      else
         Methan_Map_BR(i,j)=1;
      end
   end
end

% Mapping methane emission using band ration technique
figure
N=2;
Z=Methan_Map_BR';
temp_Z=zeros(Column,Row);
Row_count=Column;
for i=1:Column
   for j=1:Row
      temp_Z(Row_count,j)=Z(i,j);
   end
   Row_count=Row_count-1;
end
imagesc(temp_Z);
cmap = jet(N);
colormap(cmap)
hold on
markerColor = mat2cell(cmap,ones(1,N),3);
L = plot(ones(N), 'LineStyle','none','marker','s','visible','off');
set(L,{'MarkerFaceColor'},markerColor,{'MarkerEdgeColor'},markerColor);
legend('Pixels with Normal Methane Concentration','Pixels with Higher than Normal
Methane Concentration')
set(gca, 'FontName', 'Arial')
set(gca, 'FontSize', 24)
set(gca, 'FontName', 'Arial')
set(gca, 'FontSize', 24)
title('Band Ratio Method (Band 202 / Band 177), 12hr 50min, 19 June 2008,
34°23N,119°52W')
xhandle = get(gca,'xlabel');
set(xhandle,'string','Pixels Along Longtitude','fontsize',22)
yhandle = get(gca,'ylabel');
set(yhandle,'string','Pixels Along Latitude','fontsize',22)

%%
%%%%%%%%%%%%%%%%%%%%%%%%%%%%%%%%%%%%%%%%%%%%%%%%%%%%%%%%
%%%%%%%%%%%%%%%%% 2- Residual Energy Method %%%%%%%%%%%%%%%%%
%%%%%%%%%%%%%%%%%%%%%%%%%%%%%%%%%%%%%%%%%%%%%%%%%%%%%%%%

% Caluclating black body radiation
c=2.997*10.^8;% m/s speed of light in vaccum
h=6.625*10.^-34;% J.s Planck constant
k=1.3806488*10.^-23; %Boltzman Constant JK^-1
step=  1e-009;
lambda=[10^-11:step:7000*10^-9];
```

```
T=297.720923076923;
lambda_202=[2277.495*10^-9:step:2287.462*10^-9];
L_202=(2.*h.*(c.^2)./lambda_202.^5).*(1./(exp((h.*c)./(lambda_202.*k.*T))-1));
sum_L_202=sum(L_202.*step);


Radiation_Residual_202_177=zeros(Row,Column);
for i=1:Row
   for j=1:Column
      Radiation_Residual_202_177(i,j)=(Radiation_at_Band_202(i,j).*wavelength_202-
Radiation_at_Band_177(i,j).*wavelength_177);
   end
end


% Applying constraint
Methan_Map_RE=zeros(Row,Column);
for i=1:Row
   for j=1:Column
      if Radiation_Residual_202_177(i,j)<0
         Methan_Map_RE(i,j)=1;
      else
         Methan_Map_RE(i,j)=0;
      end
   end
end

% Mapping residual energy method
figure
N=2;
Z=Methan_Map_RE';
temp_Z=zeros(Column,Row);
Row_count=Column;
for i=1:Column
   for j=1:Row
      temp_Z(Row_count,j)=Z(i,j);
   end
   Row_count=Row_count-1;
end
imagesc(temp_Z);
cmap = jet(N);
colormap(cmap)
hold on
markerColor = mat2cell(cmap,ones(1,N),3);
L = plot(ones(N), 'LineStyle','none','marker','s','visible','off');
set(L,{'MarkerFaceColor'},markerColor,{'MarkerEdgeColor'},markerColor);
legend('Pixels with Normal Methane Concentration','Pixels with Higher than Normal
Methane Concentration')
set(gca, 'FontName', 'Arial')
set(gca, 'FontSize', 24)
```

```
set(gca, 'FontName', 'Arial')
set(gca, 'FontSize', 24)
title('Residual Energy Method, 12hr 50min, 19 June 2008, 34°23N,119°52W')
xhandle = get(gca,'xlabel');
set(xhandle,'string','Pixels Along Longtitude','fontsize',22)
yhandle = get(gca,'ylabel');
set(yhandle,'string','Pixels Along Latitude','fontsize',22)

%%
%%%%%%%%%%%%%%%%%%%% Evaluation of methane emission
%%%%%%%%%%%%%%%%%%%%
%% Calculating Actuall Transmittance

Actual_Transmittance_at_202=zeros(Row,Column);
Band_202_Ratio=Radiation_at_Band_202(:,:)./Radiation_at_Band_202_Calc(:,:);
for i=1:Row
   for j=1:Column
      if Methan_Map_RE(i,j)==1

Actual_Transmittance_at_202(i,j)=Trans_Value_202.*abs(Radiation_at_Band_202(i,j)./9.96
7-sum_L_202./9.967-Radiation_at_Band_202_Calc(i,j))./Radiation_at_Band_202_Calc(i,j);
      else
         Actual_Transmittance_at_202(i,j)=Trans_Value_202;
      end
   end
end
NaN_Check=isnan(Actual_Transmittance_at_202);
for i=1:Row
   for j=1:Column
      if NaN_Check(i,j)==1;
         Actual_Transmittance_at_202(i,j)=Trans_Value_202;
      end
   end
end

% Mapping actual transmittance distribution
figure
Z=(Actual_Transmittance_at_202*100)';
x = [1:Row];
y = [1:Column];
[X,Y] = meshgrid(x,y);
pcolor(X,Y,Z);
set(gca, 'FontName', 'Arial')
set(gca, 'FontSize', 24)
title('Transmittance Distribution (%), 12hr 50min, 19 June 2008, 34°23N,119°52W')
xhandle = get(gca,'xlabel');
set(xhandle,'string','Pixels Along Longtitude','fontsize',22)
yhandle = get(gca,'ylabel');
set(yhandle,'string','Pixels Along Latitude','fontsize',22)
set(colorbar,'fontsize',14)
```

```
% Apply resampling over transmittance distribution
Actual_Transmittance_Filter=zeros(Row-2,Column-2);
for i=1:Row-2
   for j=1:Column-2
      sum=0;
      for k=0:2
         for l=0:2
            sum=sum+Actual_Transmittance_at_202(i+k,j+l);
         end
      end
      Actual_Transmittance_Filter(i,j)=sum./9;
   end
end

% Mapping actual transmittance after resampling
figure
Z=(Actual_Transmittance_Filter*100)';
x = [1:Row-2];
y = [1:Column-2];
[X,Y] = meshgrid(x,y);
pcolor(X,Y,Z);
set(gca, 'FontName', 'Arial')
set(gca, 'FontSize', 24)
title('Transmittance Distribution (%), 12hr 50min, 19 June 2008, 34°23N,119°52W')
xhandle = get(gca,'xlabel');
set(xhandle,'string','Pixels Along Longtitude','fontsize',22)
yhandle = get(gca,'ylabel');
set(yhandle,'string','Pixels Along Latitude','fontsize',22)
set(colorbar,'fontsize',14)
%% Calculating Absorption
for i=1:Row-2
   for j=1:Column-2
      Methane_Absorption(i,j)=max(Actual_Transmittance_at_202(:))-
Actual_Transmittance_Filter(i,j);
   end
end

% Mapping absorption distribution
figure
Z=(Methane_Absorption*100)';
x = [1:Row-2];
y = [1:Column-2];
[X,Y] = meshgrid(x,y);
pcolor(X,Y,Z);
set(gca, 'FontName', 'Arial')
set(gca, 'FontSize', 24)
title('Methane Absorption Anomaly (%), 12hr 50min, 19 June 2008, 34°23N,119°52W')
xhandle = get(gca,'xlabel');
set(xhandle,'string','Pixels Along Longtitude','fontsize',22)
```

```
yhandle = get(gca,'ylabel');
set(yhandle,'string','Pixels Along Latitude','fontsize',22)
set(colorbar,'fontsize',14)
%% Mixing concentration Calculation
for i=1:Row-2
   for j=1:Column-2

Methan_Concentration(i,j)=reallog(Actual_Transmittance_Filter(i,j))./reallog(Trans_Value_2
02).*1670.000023508499;
   end
end

% Mapping atmospheric methane concentration
figure
Z=(Methan_Concentration)';
x = [1:Row-2];
y = [1:Column-2];
[X,Y] = meshgrid(x,y);
pcolor(X,Y,Z);
set(gca, 'FontName', 'Arial')
set(gca, 'FontSize', 24)
title('Methane Concentration (ppb), 12hr 50min, 19 June 2008, 34°23N,119°52W')
xhandle = get(gca,'xlabel');
set(xhandle,'string','Pixels Along Longtitude','fontsize',22)
yhandle = get(gca,'ylabel');
set(yhandle,'string','Pixels Along Latitude','fontsize',22)
set(colorbar,'fontsize',14)

%% Estimating methane emission flux
Pixel_Count=0;
Methane_Concentration=0;
for i=1:Row-2
   for j=1:Column-2
      if Methan_Map_RE(i,j)==1
            Dif=0;
            Dif=Methan_Concentration(i,j)-1670.000023508499;
            Methane_Concentration=Methane_Concentration+Dif;
            Pixel_Count=Pixel_Count+1;
      end
   end
end

% Calculating methane density
Methane_Density=(Methane_Concentration./Pixel_Count)./(7.5*7.5)
```

6.4.1.2 Functions

In the study two functions were supporting the main body of code in methane emission mapping and evaluation part.

6.4.1.2.1 Atmospheric Transmittance

The Transmittance_HITRAN function was responsible for reading output of HITRAN on web as ASCII file and generate atmospheric transmittance spectrum t each ROI (Fig.34).

```
function Trans=Transmittance_HITRAN
delimiterIn = ' ';
headerlinesIn = 5;
Transmittance_0=dlmread('Transmittance_Spectrum_0_Cal.txt',delimiterIn,headerlinesIn);
Transmittance_1=dlmread('Transmittance_Spectrum_1_Cal.txt',delimiterIn,headerlinesIn);
Transmittance_2=dlmread('Transmittance_Spectrum_2_Cal.txt',delimiterIn,headerlinesIn);
Transmittance_3=dlmread('Transmittance_Spectrum_3_Cal.txt',delimiterIn,headerlinesIn);
Transmittance_4=dlmread('Transmittance_Spectrum_4_Cal.txt',delimiterIn,headerlinesIn);
Transmittance_5=dlmread('Transmittance_Spectrum_5_Cal.txt',delimiterIn,headerlinesIn);
Transmittance_6=dlmread('Transmittance_Spectrum_6_Cal.txt',delimiterIn,headerlinesIn);
Transmittance_7=dlmread('Transmittance_Spectrum_7_Cal.txt',delimiterIn,headerlinesIn);
Transmittance_8=dlmread('Transmittance_Spectrum_8_Cal.txt',delimiterIn,headerlinesIn);
Transmittance_9=dlmread('Transmittance_Spectrum_9_Cal.txt',delimiterIn,headerlinesIn);
Transmittance_10=dlmread('Transmittance_Spectrum_10_Cal.txt',delimiterIn,headerlinesIn);
Transmittance_11=dlmread('Transmittance_Spectrum_11_Cal.txt',delimiterIn,headerlinesIn);


[M,N]=size(Transmittance_0);
Transmittance=zeros(M,3);
for i=1:M
   Transmittance(i,1)=Transmittance_0(i,2);

T_0_11=Transmittance_0(i,4).*Transmittance_1(i,4).*Transmittance_2(i,4).*Transmittance_
3(i,4).*Transmittance_4(i,4).*Transmittance_5(i,4).*Transmittance_6(i,4).*Transmittance_7(
i,4).*Transmittance_8(i,4).*Transmittance_9(i,4).*Transmittance_0(i,4).*Transmittance_10(i
,4).*Transmittance_11(i,4);
   Transmittance(i,3)=T_0_11;
   Transmittance(i,2)=1e7/Transmittance(i,1);
end
Trans=Transmittance;
end
```

6.4.1.2.2 At Sensor Radiation Modelling

The RadiationModelling function was responsible to model the at sensor radiation for each ROI (Diagram.13).

```
function
Calculated_Rad=RadiationModelling(Row,Column,wavelength,Class_Tide_Water,Ref,Irrad,
Steradian_Coeff,Trans_Value)

temp=abs(Irrad(:,1)-wavelength);
[idx,idy]=min(temp);
Irrad_Value=Irrad(idy,2);

for i=1:Row
```

```
    for j=1:Column
        tem_Ref=Ref.*(1-Class_Tide_Water(i,j)).*Steradian_Coeff(i,j)./0.129;
        RefWater=Ref+tem_Ref;
        Calculated_Rad(i,j)=(RefWater.*Irrad_Value.*Trans_Value)./(Steradian_Coeff(i,j));
    end
end
end
```

Department of Physical Geography and Ecosystem Science, Lund University

Lund University GEM thesis series are master theses written by students of the international master program on Geo-information Science and Earth Observation for Environmental Modelling and Management (GEM). The program is a cooperation of EU universities in Iceland, the Netherlands, Poland, Sweden and UK, as well a partner university in Australia. In this series only master thesis are included of students that performed their project at Lund University. Other theses of this program are available from the ITC, the Netherlands (www.gem-msc.org or www.itc.nl).

The student thesis reports are available at the Geo-Library, Department of Physical Geography and Ecosystem Science, University of Lund, Sölvegatan 12, S-223 62 Lund, Sweden. Report series started 2013. The complete list and electronic versions are also electronic available at the LUP student papers (https://lup.lub.lu.se/student-papers/search/) and through the Geo-library (www.geobib.lu.se).

1 Soheila Youneszadeh Jalili (2013) The effect of land use on land surface temperature in the Netherlands
2 Oskar Löfgren (2013) Using Worldview-2 satellite imagery to detect indicators of high species diversity in grasslands
3 Yang Zhou (2013) Inter-annual memory effects between Soil Moisture and NDVI in the Sahel
4 Efren Lopez Blanco (2014) Assessing the potential of embedding vegetation dynamics into a fire behaviour model: LPJ-GUESS-FARSITE
5 Anna Movsisyan (2014) Climate change impact on water and temperature conditions of forest soils: A case study related to the Swedish forestry sector
6 Liliana Carolina Castillo Villamor (2015) Technical assessment of GeoSUR and comparison with INSPIRE experience in the context of an environmental vulnerability analysis using GeoSUR data
7 Hossein Maazallahi (2015) Switching to the "Golden Age of Natural Gas" with a Focus on Shale Gas Exploitation: A Possible Bridge to Mitigate Climate Change?
8 Mohan Dev Joshi (2015) Impacts of Climate Change on *Abies spectabilis*: An approach integrating Maxent Model (MAXent) and Dynamic Vegetation Model (LPJ-GUESS)
9 Altaaf Mechiche-Alami (2015) Modelling future wheat yields in Spain with LPJ-GUESS and assessing the impacts of earlier planting dates
10 Koffi Unwana Saturday (2015) Petroleum activities, wetland utilization and livelihood changes in Southern Akwa Ibom State, Nigeria: 2003-2015